The Integration of State Space into the Dynamic Synthesis/Design and Operational/Control Optimization of a PEMFC System

Meng Wang

Dissertation submitted to the Faculty of the

Virginia Polytechnic institute and State University

in partial fulfillment of the requirements for the degree of

DOCTOR OF PHILOSOPHY

in

Mechanical Engineering

Dr. Michael von Spakovsky, Chair

Dr. Douglas Nelson

Dr. Michael Ellis

Dr. Martin Johnson

Dr. Diego Rancruel

January 11, 2008

Blacksburg, Virginia

Keywords: optimization, dynamics, control, state space, decomposition, fuel cell, PEM

The INTEGRATION of State Space into the Dynamic Synthesis/Design and Operational/Control Optimization of a PEMFC System

by Meng Wang

ABSTRACT

A typical approach to the synthesis/design optimization of energy systems is to only use steady state operation and high efficiency (or low total life cycle cost) at full load as the basis for the synthesis/design. Transient operation is a secondary task to be solved by system and control engineers once the synthesis/design is fixed. This dissertation considers the system dynamics in the process of developing the system using a set of transient thermodynamic, kinetic, and geometric as well as physical and cost models developed and implemented for the components of a 5 kW PEMFC (Proton Exchange Membrane Fuel Cell) system. The system is composed of three subsystems: a stack subsystem (SS), a fuel processing subsystem (FPS), and a work recovery and air supply subsystem (WRAS). To study the effect of control to the optimization, State Space control design is used in a looped set of optimizations. These results are compared to those resulting from a more direct optimization of the controller designs in which the gains for the controllers are part of the decision variable set for the overall optimization. Then, dynamic optimization results are obtained and compared with steady-state optimization results to illustrate the advantages of dynamic optimization. Also, a multi-

level optimization technique, dynamic iterative local-global optimization (DILGO), is utilized for the optimization of the PEMFC system by separating the system into three subsystems and the results are compared with the single level optimization results, in which the whole system is optimized together.

Acknowledgements

The author wishes to acknowledge the following:

My advisor, Dr. Michael von Spakovsky for his instructions, and encouragement during the past three and half years. From him, I obtained a lot of valuable knowledge and experience during my study and research at Virginia Tech, which will benefit me forever.

Dr. Douglas Nelson, Dr. Michael Ellis, Dr. Martin Johnson, Dr. Al Kornhauser, and Dr. Diego Rancruel for serving on my committee. Their comments and recommendations are greatly appreciated.

Mr. Kihyung Kim, my officemate, who is working on the same project with me. Working and studying with him is a great experience for me.

I also want to thank every person in our group and my friends in Blacksburg, Vikram, Richard, Charls, Vajay, Wandi, Xiaoyu, Yong, Jianqiu, Yumin, Dong, and Huan, for their support and company.

This is especially dedicated to my parents, Changsong Wang and Xiufeng Gu, for the support and love they give me through life.

This research project was performed at Virginia Tech under funding from EPA. I gratefully acknowledge both the Virginia Tech and EPA for their support.

Meng Wang

Table of Contents

List of Figures

List of Tables

Acronyms Index

APU	Auxiliary Power Unit	LTSR	Low Temperature Shift Reactor
BOPS	Balance of Plant Subsystem	MCFC	Molten Carbonate Fuel Cell
CFD	Computational Fluid Dynamics	MIMO	Multi-input/Multi-output
DILGO	Dynamic Iterative Local-Global Optimization	ORS	Optimum Response Surface
DMFC	Direct Methanol Fuel Cell	PAFC	Phosphoric Acid Fuel Cell
DMINLP	Dynamic Mixed Integer Non-linear Programming Problem	PEMFC	Polymer Electrolyte Membrane Fuel Cell
DOE	Department of Energy	PES	Power Electronics Subsystem
EFA	Engineering Functional Analysis	PrOx	Preferential Oxidation
EPA	Environmental Protection Agent	SG	Steam Generator
FPS	Fuel Processing Subsystem	SISO	Single-input/Single-output
HTSR	High Temperature Shift Reactor	SMR	Steam-Methane Reformer Steam-to-Methane Ratio
IC	Internal Combustion	SOFC	Solid Oxide Fuel Cell
ILGO	Iterative Local-Global Optimization	SS	Stack Subsystem
LGO	Local-Global Optimization	WRAS	Work Recovery and Air Supply Subsystem

Chapter 1

Introduction

Among all the technologies for energy conversion, fuel cells have become more and more important for transportation, stationary (central and distributed) and portable applications. Among the reasons are that fuel cells and their supporting technology have the potential for both high efficiencies (on and off-design) and lower emissions. Generally, fuel cells provide higher efficiency (especially in the low power range) over gas turbines, IC engines, etc. Hybrid fuel cell systems (e.g., SOFC/gas turbine (GT) cycles, hybrid fuel cell electric vehicles, etc.) provide even higher efficiencies and deliver superior environmental performance at the same time.

On the other hand, there are still several technical barriers in fuel cells which need to be overcome to make fuel cells competitive candidates among the various energy system technologies, such as cost, fuel storage, durability, etc. A variety of fuel cell technologies are in different stages of development. The common classification of fuel cells is by type of electrolyte used in the cells and includes proton exchange membrane fuel cells (PEMFCs), alkaline fuel cells (AFCs), phosphoric acid fuel cells (PAFCs), molten carbonate fuel cells (MCFCs), and solid oxide fuel cells (SOFCs). Of these, one of the primary candidates for transportation and distributed-power applications is the PEMFC system. There are several advantages over other types of fuel cells, which make the PEMFC the leading candidate in transportation applications involving personal vehicles and favorable as a candidate for distributed power and cogeneration. To meet the same power requirements, the high power densities allow smaller size of PEMFC to be utilized. And with a solid phase polymer membrane, all the components inside a PEMFC are solid, which make it much easy and safe to install, transport, etc., especially for transportation applications. The low operation temperatures (60^{o} to 80^{o}C), allow for potentially faster startup than higher temperature fuel cells.

Even with these advantages, for gains both in energy savings and pollutant emissions, it is important to synthesize/design and operation/control the fuel cell system intelligently in order to meet the varying load profiles and safety requirements which they must satisfy.

Typically, a system design procedure consists of system synthesis/design, design-point operating condition selection, and off-design operation. Here, synthesis refers to changes in system or component configuration while design refers exclusively to, for example, the nominal (full load or design point) capacity, geometry of a given component, etc. The operating condition represents the operating point, e.g., pressure, temperature, efficiency, or lowest system emissions. During off-design operation, the control architecture needs to be designed so that the system can meet its dynamic operating requirements. One of the major goals of this research is to study new energy system development procedures and methodologies can be used to design such architecture within the context of system synthesis, design, control and dynamic operation.

1.1 System Synthesis/Design and Operation/Control Problem

In recent years, with the increasing complexities of energy systems and the level of interactions between their various subsystems, e.g. a fuel cell system and its subsystems, and with the increasing requirements both for high efficiencies and low emissions, it has become more and more important to carry out the synthesis/design and operation/control of the system in a completely integrated fashion such that the demands imposed by all the subsystems can be accommodated in the best way possible. When developing new energy systems, today's engineers still rely heavily on rules-of-thumb, individual experience and a fairly non-integrated, non-interdisciplinary approach of basic calculations, i.e. trade-off analysis, due to the lack of comprehensive synthesis/design tools and the simplicities of applying these methods. Such traditional methods are limiting to say the least. In cases where optimization is considered, partially due to the fact that new and more powerful computers have become available and optimization tools more popular, it is viewed as a straightforward mathematical problem. However, for large-scale, highly non-linear optimization problems, this is not always the case and often times leads to problems too

complex to solve. Even significant increases in computational power are not sufficient to offset this ever increasing complexity of the ensuing synthesis/design and operation/control problem. Therefore, the need for methods that permit effective solutions of large-scale optimization problems is still an area of research, which generates great interest.

In formulating the entire large-scale synthesis/design and operation/control optimization problem, i.e. identifying all the interacting subsystems, choosing the possible configurations and decision variables, and defining the physical constraints, it may turn out that it is impractical to solve the entire problem as a single optimization problem (as opposed to solving a set of multiple problems). The reasons are:

- The number of decision variables involved may simply be too large for an efficient solution. In fact, given the current state of mathematical optimization, a solution may not be obtainable at all in the most complex cases.
- A single group of engineers may not possess all the expertise required for dealing with the technologies, subsystems, and components involved in the problem.
- The integration of different computer codes, which simulate different aspects of the system, may be difficult. This is even more so the case if such codes are written on entirely different platforms. In addition, these codes may not be available for use to all the members of the entire team.
- Even in cases when code integration is possible, the overhead is simply too great to make the optimization viable. This is especially the case if the simulation tools are computationally expensive to use (e.g., as is often the case with CFD codes).
- The synthesis/design and operation/control of the different subsystems may, in many cases, be done at different stages and times, crossing company lines. Furthermore, it is not uncommon to have design teams that are not located entirely at one facility, which added to cultural differences, complicates the task at hand even further.

When such a single-level approach is unable to solve the synthesis/design and operation/control optimization problem due to all the complexities involved, a multi-level approach using a decomposition technique may be used to formulate the optimization problem in such a way as to permit the use of optimization. Decomposition techniques are methods employed to break an optimization problem into a set of nearly equivalent

smaller problems in order to facilitate the solution of the large problem and overcome both the mathematical and cultural difficulties.

1.2 System Dynamic Operation/Control

For purposes of either off-design operation or dynamic optimization, the energy system needs to be controlled intelligently. In recent years, rapid and significant advances in energy system technologies together with advances in power electronics and control systems have enabled the development of high performance energy systems for different applications. In the case of fuel cell systems, in particular the static and dynamic performance and the energy efficiency of the system are critically dependent on the intelligent design of the control system and control strategies.

There are two approaches for the design of a system's control architecture: classical control design and modern control design. The use of transfer-function-based methods such as root locus and frequency response have been referred to as classical control design, whereas those using the state-space approach have been referred to as modern control design. The idea of state-space comes from the state-variable method of describing differential equations. In this method, dynamic systems are described by a set of first-order differential equations in variables called the state, and the solution may be visualized as a trajectory in space.

Advantages of state-space design are especially apparent when engineers design controllers for systems with more than one control input or more than one sensed output. In the control design of an energy system, especially a complex one, because variables are usually strongly coupled in the system, e.g., flow rate and pressure, state space control design has a big advantage over transfer-function-based classical control design with respect to the best dynamic response as well as the best system efficiencies across all possible operating conditions.

However, typical control system design is still limited in finding appropriate values for the controller parameters once the system synthesis and design (i.e., geometry) have been determined, leaving no space for exploring the effects of system dynamics on life cycle costs. Additionally, most times the typical control system design approach yields changes in system configuration (synthesis) and geometry which separates the final

system from the synthesis/design originally determined through analysis and optimization, which in turn may affect its optimal performance negatively. Thus, it becomes desirable to simultaneously optimize the control architecture along with the synthesis/design and operation system taking into account in either a dynamic or a quasi-stationary manner load and environmental variations over time. In fact, when transient regimes happen quite often, taking these into consideration during the process of developing the system becomes very important, as is the case, for example, for small power units used in transportation applications, distributed power and cogeneration, and energy system start-up. This dynamic optimization contrasts with the common practice of designing a system for a single design point (typically chosen to be close to the most demanding operating point) followed by a verification of proper operation at off-design.

1.3 Proton Exchange Membrane Fuel Cell (PEMFC) System

Generally, a fuel cell system consists of a fuel processing subsystem (FPS), fuel cell power subsystem (FCPS) and a power conditioning subsystem (PCS), as shown in Figure 1.1. The FPS converts a commercially available gas, liquid, or solid fuel to a fuel suitable for the FCPS. The PCS is an enabling technology that is necessary to convert DC electrical power generated by a fuel cell into usable AC power for stationary loads, automotive applications, and interfaces with electric utility grids. The FCPS consists of a fuel cell stack and a thermal management subsystem to control the stack temperature condition the air, and recover energy from exhaust streams. Typical cell components within a PEMFC stack are illustrated in Figure 1.2 and include

- an ion exchange membrane
- electrically conductive porous backing layers
- electrode-catalyst layers (the electrodes) at the interfaces between the backing layers and the membrane
- flow plates that deliver the fuel and oxidant to reactive sites via flow channels and electrically connect the cells.

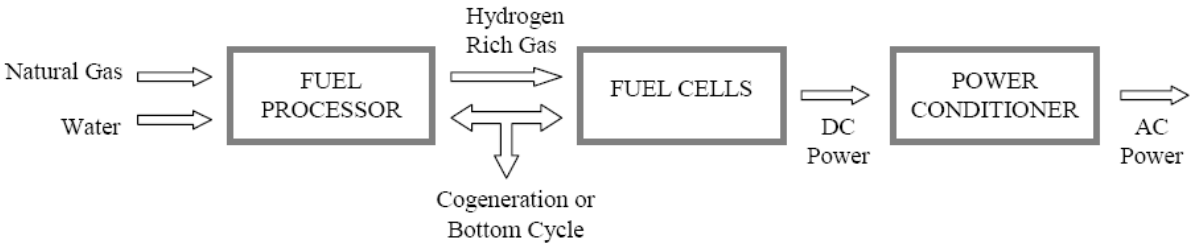

Figure 1.1 General fuel cell system schematic.

On the anode side of a cell, the hydrogen gas ionizes, releasing electrons and creating H^+ ions (protons).

$$2H_2 \rightarrow 4H^+ + 4e^- \tag{1.1}$$

The electrons are eventually captured as work via some external load. At the cathode, oxygen reacts with electrons coming from the anode and H^+ ions transported through the electrolyte to form water in an exothermic reaction, i.e.

$$O_2 + 4e^- + 4H^+ \rightarrow 2H_2O \tag{1.2}$$

For both these reactions to proceed continuously, electrons produced at the anode must pass through an electrical circuit to the neighboring cathode or via a bus and external circuit. Also, in PEMFCs, polymers called proton exchange membranes are the electrolytes utilized to move the H^+ ions from anode to cathode.

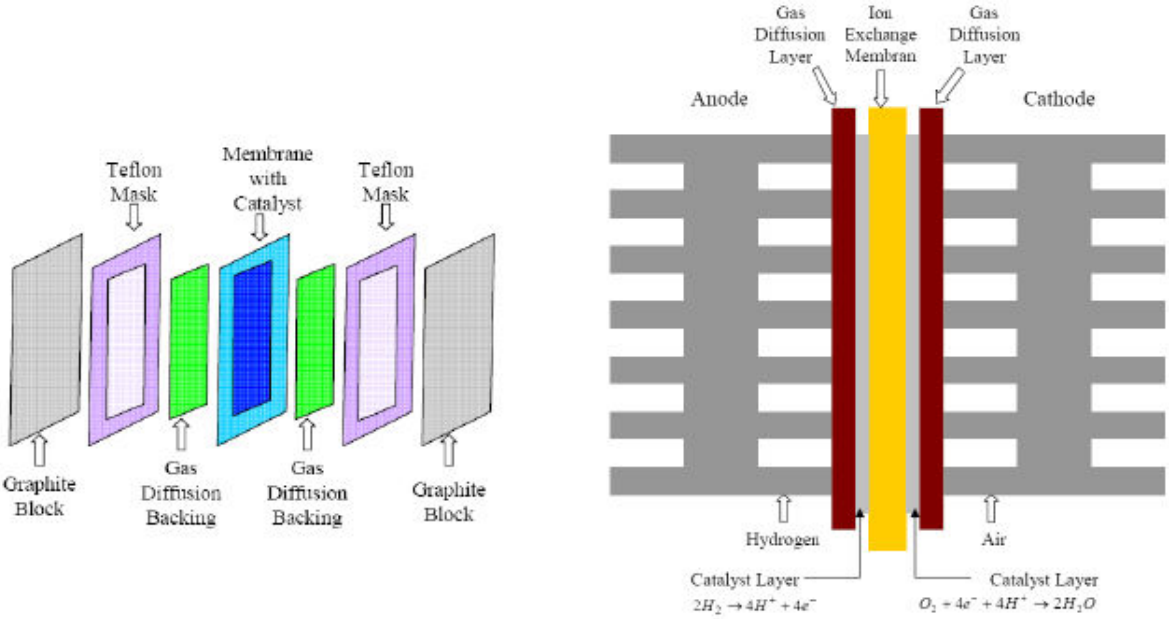

Figure 1.2 Schematic of a representative PEMFC and single cell structure.

The FPS delivers fuel to the fuel cell stack by converting a commercially available gas, e.g., natural gas, to a fuel, e.g., hydrogen, suitable for the fuel cell anode reaction. Figure 1.3 shows the general fuel processing process for a PEMFC.

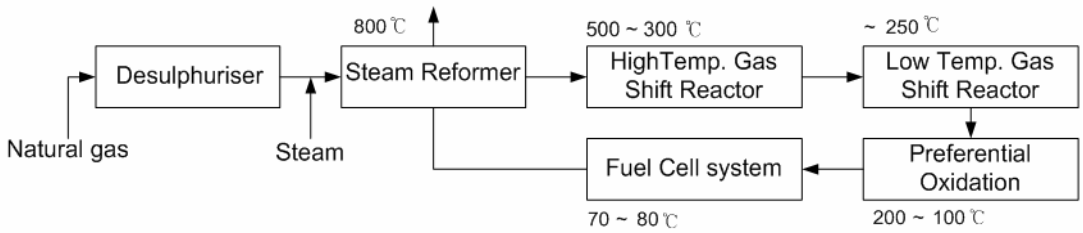

Figure 1.3 Fuel processing subsystem schematic (FPS).

The desulphuriser removes organic sulphur compounds contained in natural gas before any further fuel processing can be carried out. Ever if suphur levels in fuels are below 0.2 ppm, some deactivation of steam reforming catalysts can occur.

By adding steam to the natural gas, the methane-steam reformer converts the hydrocarbons to a hydrogen rich fuel. A typical steam-to-carbon molar ratio is 2.5:1. The reforming reaction and the associated water-gas shift reaction carried out in the reformer are

$$CH_4 + H_2O \rightarrow CO + 3H_2 \tag{1.3}$$

$$CO + H_2O \rightarrow CO_2 + H_2 \tag{1.4}$$

A steam methane reformer running on natural gas and operating at atmospheric pressure with an outlet temperature of 800 ^{o}C produces a gas comprised of around 75% hydrogen, 15% carbon monoxide, and 10% carbon dioxide on a dry basis. However, for the PEMFC, the carbon monoxide content must be drastically reduced to much lower levels. The initial reduction occurs two reactors, a high- and a low-temperature water-gas shift reactor. In order to drop the carbon monoxide levels even further low (to less then 10 ppm to prevent poisoning the catalyst in the stack), a selective oxidation reactor is used to preferentially oxidize the remaining CO down to the required levels. This is done by adding a small amount of air to the fuel stream, which then passes over a precious metal catalyst. This catalyst preferentially absorbs the carbon monoxide, rather than the hydrogen, where it reacts with the oxygen in the air.

In addition to fuel processing and delivery, both thermal and water management are crucial issues in a PEMFC system. Heat exchangers must be utilized between reactors so

that the flow temperature can meet the requirement of each reactor. Furthermore, maintaining the proper quantity of water within a PEMFC is very important for effective operation. If there is too much, the cell will flood; too little, the cell membrane will dehydrate. Either will severely degrade fuel cell performance. The proper balance is achieved by considering the water production, evaporation, and humidification levels of the reactant gases. The required humidification level is a complex function of the cell temperature, pressure, reactant feed rates, and current density. Optimum PEMFC performance is achieved with a fully saturated, yet unflooded membrane.

Finally, since the fuel cell stack provides a variable DC voltage output which is not typically directly usable for the load, an electric power conditioning subsystem converts the electric power from DC into regulated DC or AC for consumer use.

1.4 Dissertation Objectives

As discussed above, currently, the typical approach to energy system development is to only use steady state operation and high efficiency (or low total life cycle cost) at full load as the basis for the synthesis/design. Transient operation and the controllers needed to optimally control system operation are a secondary task to be solved by system and control engineers once the optimal synthesis/design is fixed. The problem with this approach for highly non-linear, complex, dynamic energy systems is that this type of approach ignores the effects which transients and a given control architecture have on the development of the system, i.e. on its synthesis/design, and vice versa. In other words, there is a tight coupling between synthesis/design and operation/control such that changes to one affect the other and changes to the other affect the former.

Thus, there exists a need for a general methodology that will permit the integrated synthesis/design and operation/control optimization of energy systems at design and off-design while considering the system dynamic requirements and subsystem transient interactions.

The overall goal of this doctoral work is to investigate the effects of the coupling on energy system development at all levels (i.e. synthesis, design, operation, and control) and to develop an approach for dealing with them. This approach will be demonstrated

by simultaneously and dynamically determining the optimal synthesis/design and operation/control of a 5 kWe PEMFC system for highly transient loads.

In order to achieve this overall goal, the following objectives are envisioned:

- Develop a comprehensive set of detailed transient system/subsystem/component thermodynamic, kinetic, geometric, and cost models for a system composed of three subsystems: a stack subsystem (SS), a fuel processing subsystem (FPS), and a work and air recovery subsystem (WRAS); this will be done in collaboration with Kihyung Kim (Kim, 2008);
- Understand and then develop an integrated approach for applying the state space control approach, which requires model linearity, to the highly non-linear system/subsystem/component models developed here;
- Integrate this state space control approach into the dynamic synthesis/design and operation/control optimization of each PEMFC subsystem (FPS, WRAS, SS) in order to optimally design a set of MIMO (multi-input and multi-output) controllers, one for each subsystem or a single MIMO controller for the overall system consistent with the optimal synthesis/design and operation of the subsystem and/or system;
- Verify that optimizing the control architecture separately from the process of optimizing the system synthesis/design does not lead to the optimal system;
- Develop a base line optimal system synthesis/design based on operating at steady state and full load and use this to verify that taking into account transient operation during the optimization process indeed makes a difference;
- Verify the difference or compatibility of the integrated state space approach developed here with that which determines the optimal control architecture using the integrated approach found in Rancruel (2005); the latter determines a set of optimal controller gains directly from a single system-wide optimization process in which the gains are part of the overall decision variable set for synthesis/design and operation/control;
- For the dynamic synthesis/design and operational/control optimization process of the overall system, use the decomposition strategy for multi-level optimization called Dynamic Iterative Local-Global Optimization (DILGO) found in Rancruel

(2005) to perform the synthesis/design and operational/control optimization of the PEMFC system and compare the results with those obtained using a single-level optimization approach;

- Compare the deterministic results obtained above with the probabilistic and multi-objective results being developed by Kim (2008) and draw appropriate conclusions.

1.5 Original Contributions and Practical Impact

The originality of what is proposed here lies both in the development implementation, and validation of a comprehensive set of detailed transient models for PEMFC simulation as well as in the development of a dynamic integrated synthesis/design and operational/control optimization approach which utilizes both state space control as an integral part of the process and dynamic decomposition in solving large-scale optimization problems. Originality include showing and quantifying difference mode in optimizing the system control architecture simultaneously with system synthesis/design, verifying the validity of using a dynamic decomposition as opposed to a single-level strategy for large-scale optimization, quantifying the transient effects on the final optimal system synthesis/design and operation/control, and comparing deterministic versus probabilistic/multi-objective results.

The work done here can have an immediate practical impact on the way energy systems, e.g., fuel cell systems, are dynamically synthesized/designed and operated/controlled in that it will

- provide a methodology to solve the optimal design problem of complex, highly-nonlinear systems with dynamic operation as part of the system lift cycle.
- allow the integration of state space control design into the synthesis/design and operation/control optimization process.
- provide a comprehensive set of detailed transient models for PEMFC system simulations.
- establish effective control strategies for PEMFC system operation using MIMO controllers.
- provide an economically and technologically viable 5kWe PEMFC system synthesis/design and set of controllers for distributed power applications.

Chapter 2

Literature Survey

2.1 Energy System Synthesis/Design

Systematic methodologies developed and used to determine the "best" and/or "optimal" synthesis/design of an energy system in general and a fuel cell system in particular can be classified broadly into either methods of analysis or optimization (see Figure 2.1).

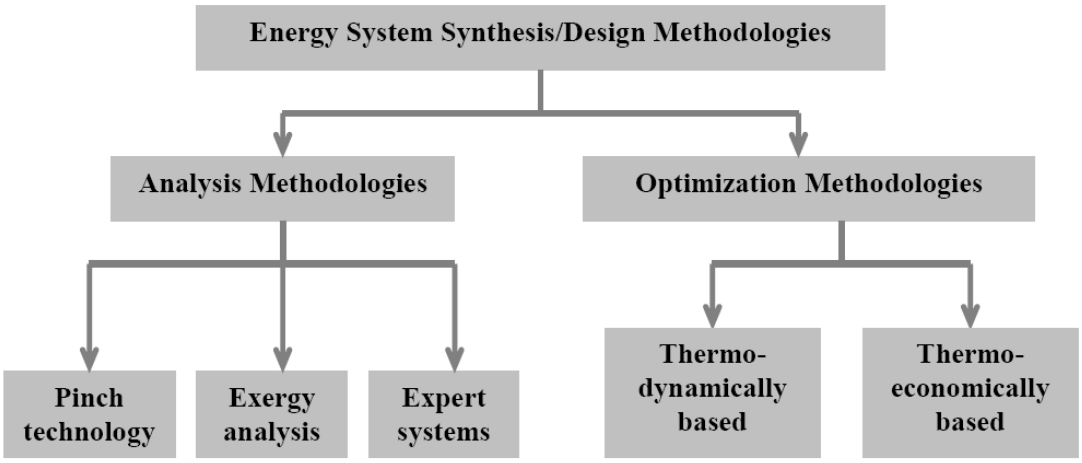

Figure 2.1 Classification of energy system synthesis/design methodologies.

Analysis methodologies and tools are typically used to gain a fundamental understanding of a process or system. The information is then used to rationally define a set of possible configurations or a mode of operation. A systematic analysis using rules of thumb and/or particular procedures of analysis is then applied to refine the synthesis/design so that a figure of merit is at least notionally maximized or minimized. Examples of such procedures or methodologies include pinch technology (e.g., Linnhoff, 1989), exergy analysis (Moran, 1982; Tsatsaronis et al. 1989), and expert systems (e.g., Melli and Sciubba 1997).

Pinch Technology, Exergy Analysis, and Expert Systems

Pinch technology is originally applied for the analysis and design of heat exchanger networks, which is a tool that can be used for process design, and also as a systematic approach without a comprehensive operational research base used primarily in process industry for reducing costs. It has led to significant energy savings in the chemical and process industries. It does this by minimizing the number of heat exchangers in a heat exchanger network, and determining the placement of heat pumps and power generation cycles with respect to this network. Although it has not by any means gained wide acceptance in this industry, it has, nevertheless, gained more of a foothold than all of the mathematically based modeling, analysis and optimization methods that have been or are being developed in the research domain. Linnhoff (1989) presented a traditional Second Law Analysis of s simple heat exchanger network, exergy analysis, pinch technology, and applying pinch technology to combined heat and power. The results showed that pinch technology is firmly based in Second Law Analysis. In contrast to conventional Second Law Analysis, however, it does not require a base case design. Rather, it performs true synthesis. Also, it is capable of a methodical distinction between "inevitable" and "avoidable" exergy losses.

Exergy analysis (Moran, 1982) is a systematic but less structured way of analyzing alternative synthesis/design options for energy systems and components. Though less structured than other 1st Law approaches, it does provide a more complete picture and a greater number of insights into the overall synthesis, design, and operational problem since it accounts both for the quantity and quality of all energy conversions present in a process. Furthermore, it is not primarily centered on heat exchange or mass exchange networks. It uses a set of common sense guidelines to detect and avoid or remove the so-called 2nd Law errors in synthesis, design, and operation in order to guarantee a more cost-effective and/or better performing system. The objective of this type of analysis is the judicious expenditure of exergy to reduce not just fuel costs but total costs. An incomplete list of "common sense guidelines", which would be used in an exergy analysis along with exergy balances of the system and each of its components and subsystems, is the following:

- Do not use excessively large or excessively small thermodynamic driving forces in process operations.
- Minimize the mixing of streams with differences in temperature, pressure, or chemical composition.
- Do not discard energy at high temperatures to the ambient or to cooling water.
- Do not heat refrigerated streams with hot streams or with cooling water.
- When choosing streams for heat exchange, try to match streams where the final temperature of one is close to the initial temperature of the other.
- When exchanging heat between two streams, the exchange is more efficient if the flow heat capacities of the streams are similar. If there is a big difference between the two, consider splitting the stream with the larger heat capacity.
- Minimize the use of intermediate heat transfer fluids when exchanging heat between two streams.
- Heating (or refrigeration) is more valuable the further its temperature is from the ambient.
- Minimize the throttling of steam or other gases.
- The larger the mass flow, the larger the opportunity to save (or to waste) energy.
- Use simplified exergy (or availability or available energy) consumption calculations as a guide to process modifications.
- Some exergy inefficiencies cannot be avoided. Others can. Concentrate on those which can.

Expert systems capable of assisting the process engineer in thermal processes design selection can improve both the quality and the variety of the solutions proposed. Melli and Sciubba (1997) showed that an expert system can be of valid help in finding answers to conceptual process selection. They described an automatic procedure of choosing the most convenient process configuration for a given set of design goals. The procedure makes use of a very powerful set of computational techniques, which are collectively known under the term artificial intelligence, whose specific task is to make possible the codification and (in some measure) the reproduction, of the thinking patterns of human mind. The expert systems (E.S.), which are a subset of these techniques, can be used to reproduce the (human) engineer's decisional path which proceeds from the design data

and constraints to the possible process configurations. It is shown that it is indeed possible to construct an E.S. which performs the following principle operations:

1. acquisition in a proper format of the inputs which represent the knowledge of the state of the domain the E.S. will have to deal with: design data, type and state of the environment, components specifications, state-of-the-are of a certain technology etc.;
2. interaction with the user about the (logically and physically) exact design goals, i.e. about some physical, logical or numerical properties the solution must possess;
3. manipulation of its knowledge base according to a predetermined set of rules contained in its inference engine;
4. ability to selectively call other numerical procedures: of interest here is the fact that an E.S. can call one of the available process calculation codes.

However, there are significant limitations as to what can be done with such analysis methodologies. Approaches for overcoming these limitations are mathematically based, which simultaneously model the thermodynamic and/or economic aspects of a system and its components. The degree of detail in the modeling varies from the simplest system models which treat each component as a black box and are, thus, viable for a single operating point only to complex system models which incorporate detailed component models that capture the behavior of each component at all operating points. Such models (geometric, thermodynamic, kinetic, cost, etc.) can be coupled to optimization algorithms whether gradient-based or heuristic which search the solution space of all possible solutions for the optimum synthesis/design and/or operation of the system and its components. Of course, the degree of success of such an approach depends on the complexity of the models used (e.g., their nonlinearities, number of degree of freedom, etc.) and on the effectiveness of the optimization algorithms employed. Even when the latter are very effective, model complexity can very quickly render a problem as impractical or ever impossible to solve. Under such circumstances, the models must either be simplified with a subsequent undesirable loss of information or additional strategies must be employed such as the decomposition strategies which will be discussed in section 2.2 below.

Over the last thirty years, the use of optimization for the synthesis/design optimization of energy systems has become more and more widespread. A large number

of researchers are involved in this field. The applications that can be found range from relatively simple non-linear programming (NLP) problems (e.g., Valero et al, 1994) to very complex mixed integer non-linear programming (MINLP) problems (e.g., Olsommer, von Spakovsky, and Favrat, 1999a, b).

The NLP problem Valero (1994) published is a conventional solution to the CGAM problem, which is an economic optimization of a simple cogeneration system involving physical, thermodynamic, and economic models. It assumes ideal gas behavior and constant heat capacities. An optimization strategy is presented as a result. The strategy is based on conventional techniques and incorporates assumptions and consequences of the exergetic cost theory (ECT) and of symbolic exergoeconomics. In addition to the results obtained by conventional techniques, this method provides valuable information about the interaction of components.

Olsommer, von Spakovsky, and Favrat presented their use of optimization for the synthesis/design optimization of a MINLP problem. In their articles, they showed that decision models developed to minimize the total costs associated with cogeneration systems only partially respond to the problems associated with the choice of configuration, component design, and the operation of the waste incineration/cogeneration unit. In face, the time factor which greatly affects certain key parameters such as the amount of wastes and the electrical and heating demands placed on the system renders the problem of synthesis, design and operation very complex. A thermoeconomic methodology and the results of an application of it to a waste incineration system with cogeneration and a gas turbin topping cycle are presented. Also, the details of the approach used to incorporate reliability and availability considerations into the methodology are presented. The methodology permits a more realistic evaluation of performance, flows and costs at both the structural (synthesis/design) and operational levels and leads, thus, to more rational decisions on system synthesis, design and operation.

In these set of problems, the most established and well-developed discipline-based optimization methodologies for synthesis/design are Entropy Generation Minimization (EGM) and Thermoeconomics. EGM (e.g., Bejan, 1995; Bejan et al, 1996) is a second law-based methodology which uses a purely thermodynamic objective. In contrast,

thermoeconomics (whether or not based on exergy) combine both cost and thermodynamic principles into a single objective to account for the natural trade-off between efficiency and capital cost and, thus, address some of the inherent drawbacks of EGM (e.g., von Spakovsky and Evans, 1984; Evans and von Spakovsky, 1993; von Spakovsky, 1994; El-Sayed, 1996).

2.2 Decomposition Strategies for Large Scale Optimization

Most practical energy system synthesis/design optimization problems are single- or multi-objective, deterministic optimization problems characterized by a mix of continuous-discrete variables, non-linearities, and discontinuous and nonconvex synthesis/design surfaces. The optimization used algorithms to solve these problems can be broadly divided into two categories: gradient-based algorithms and non-gradient-based algorithms. The gradient-based algorithms are a class of search methods for real-valued functions. These methods use the gradient of a given function as well as function values. Thus, consider the unconstrained optimization problem

$$\text{Minimize } f(\vec{x}), \text{ w.r.t. } \vec{x} \tag{2.1}$$

The resulting iterative algorithm is given by

$$\vec{x}^{k+1} = \vec{x}^{k} - \lambda^{k} \nabla f(\vec{x}^{k}) \tag{2.2}$$

where λ is a sufficiently small step-size. The choice of the step-size leads to a number of different algorithms: the steepest descent method, Newton and quasi-Newton methods (e.g., the Fletcher-Powell and the BFGS methods), conjugate direction methods (e.g., the methods of Fletcher-Reeves, Polar-Ribiere, and Hestenes-Stiefel). Some of these methods are introduced below briefly.

The Steepest Descent Method

In the steepest descent method, the choice of direction is where f decreases most quickly, which is in the direction opposite to $\nabla f(\vec{x})$. Hjorteland (1999) gave introductions about the steepest descent method in optimization. The search starts at an arbitrary point x_0 and then slide down the gradient, until we are close enough to the solution. Now, the question is, how big should the step taken in that direction be? Obviously, we want to

move to the point where the function f takes on a minimum value, which is where the directional derivative is zero. The directional derivative is given by

$$\frac{d}{d\lambda^k} f\left(\vec{x}^{k+1}\right) = \nabla f\left(\vec{x}^{k+1}\right)^T \cdot \frac{d}{d\lambda^k} \vec{x}^{k+1} = -\nabla f\left(\vec{x}^{k+1}\right)^T \cdot g\left(\vec{x}^{k}\right) \tag{2.3}$$

where $g\left(\vec{x}^{k}\right)$ is the gradient at the given point. Setting this expression to zero, we see that λ^k should be chosen so that $\nabla f\left(\vec{x}^{k+1}\right)$ and $g\left(\vec{x}^{k}\right)$ are orthogonal. The next step is then taken in the direction of the negative gradient at this new point and we get a zig-zag pattern as illustrated in Figure 2.2. The iteration continues until the extreme bas been determined within a chosen accuracy.

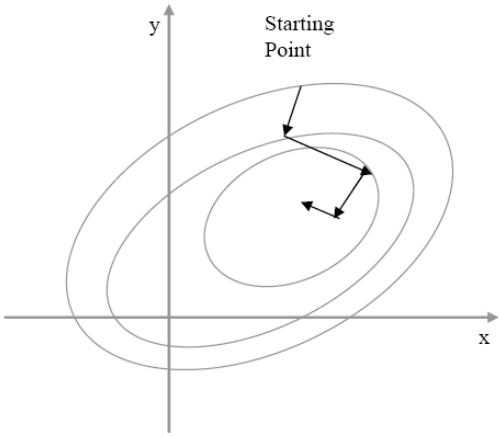

Figure 2.2 Steepest descent method approaches the minimum in a zig-zag manner.

Newton's Method

In mathematics, Newton's method is a well-known algorithm for finding solutions of equations. It can also be utilized to find local maxima/minima of functions by noticing that if a real number x* is a stationary point of a function $f(x)$, then x* is a root of the derivative $f(x)$, and therefore one can solve for x* by applying Newton's method to $f(x)$. The Taylor expansion of $f(x)$

$$f(x+\Delta x) = f(x) + f'(x)\Delta x + \frac{1}{2} f''(x)\Delta x^2 \tag{2.4}$$

is minimized when Δx solves the linear equation

$$f'(x) + f''(x)\Delta x = 0 \tag{2.5}$$

and $f''(x)$ is positive. Thus, provided that $f(x)$ is a twice-differentiable function and the initial guess x_0 is chosen close enough to x*, the sequence (x_n) defined by

$$x_{n+1} = x_n - \frac{f'(x_n)}{f''(x_n)}, \qquad n \geq 0 \tag{2.6}$$

will converge towards x*.

However, due to the nature of the optimization problems involved, gradient-based methods may not be sufficient and for nonlinear problems may have a hard time finding the global optimum among many local optima. Also, using discrete variables with a gradient-based method may be problematic.

To circumvent some of these limitations, a number of non-gradient-based algorithms based on specialized search schemes have been developed. These types of algorithms, when properly conditioned, specialize in performing a complete search of the entire synthesis/design space and as a consequence are often referred to as global search algorithms. Among these are rule-based expert systems. The latter are heuristic methods and have received considerable attention lately (Carlos A. Coello Coello, Gary B. Lamont, 2004). However, the most popular and most developed methods for global search are neural networks (Xiang-Sun Zhang, 2000), simulated annealing (Metropolis et al. 1953) and genetic algorithms (Hajela and Lee, 1996, Rao, 1996).

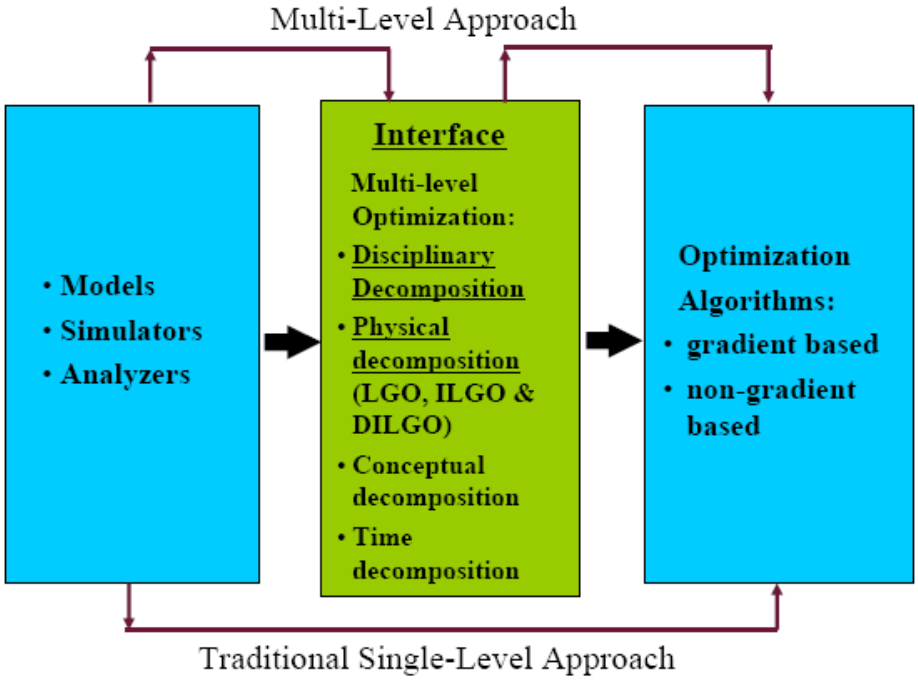

Figure 2.3 Decomposition strategies for large-scale optimization (Rancruel, 2005).

Nonetheless, even with these algorithms or even more powerful hybrid gradient/non-gradient based algorithms, cases of large-scale, highly non-linear optimization arise which these algorithms can not effectively solve and, even significant increases in computational power are not sufficient to offset the ever increasing complexity of the ensuing synthesis/design and operation/control optimization problem. In formulating this problem, it may turn out that solving it as a single problem is simply impractical. However, such complex problems can be solved as a set of smaller problems which approximate the larger one. This is done through the use of decomposition techniques or strategies as shown in Figure 2.3.

Four major forms of decomposition can be employed in energy system synthesis/design and operation/control optimization. The first is disciplinary decomposition in which, for example, thermodynamics and cost are de-coupled and each discipline is optimized independently using a multi-objective approach. Additional forms are time and conceptual decomposition which, respectively, transform a dynamic or transient optimization problem into a quasi-stationary and decouple the synthesis/design optimization from the operational optimization so that the latter follows the former. Discussions and examples of time decomposition can be found in Frangopoulos, von Spakovsky and Scuibba (2002) and in Olsommer, von Spakovsky and Favrat (1999 a, b).

A fourth type of decomposition is physical, i..e. is one which decomposes the system across unit (component or subsystem) boundaries. One of the first to devise a scheme for physical decomposition were El-Sayed and Evans (1970), a scheme which has come to be known as the Evans–El-Sayed Formalism. Without a doubt, this is the single most influential work in thermoeconomics, which applies decomposition. Many of the leading cost assignment and decomposition strategies for optimization such as Engineering Functional Analysis - EFA (von Spakovsky and Evans, 1993; Evans and von Spakovsky, 1993), Thermoeconomic Functional Analysis - TFA (Frangopoulos, 1994), Exergy Structural Theory (Valero et al., 1994) and others (e.g., Tsatsaronis and Pisa, 1994) are to a certain extent variations of the original Evans–El-Sayed method. This method was based on the Lagrange multiplier theorem of optimization and made possible, under certain very specific conditions, the decomposition of a system into units (for a brief

discussion of the essential features of the original Evans–El-Sayed method, the reader is referred to Muñoz and von Spakovsky, 2000, 2001).

Based on the thermoeconomic approaches developed by Evans, Frangopoulos, and von Spakovsky (i.e. TFA and EFA), the concept of "thermoeconomic isolation (TI)" was introduced (Evans, 1980; Frangopoulos, 1983; Frangopoulos and Evans, 1984; von Spakovsky and Evans, 1984). TI is defined as the ability to optimize independently each unit of a system and yet still arrive at the optimum for the system as a whole. TI is, in fact, a stronger condition than mere decomposition. In the latter, the complete set of decision variables for the system and its components can only partially be distributed to the units into which the system is decomposed, i.e. although each unit has its own local set of decision variables independent of those of the other units, there is still a subset of decision variables at the system level which cannot be uniquely assigned to any given unit. Thus, not all of the decision variable sets can be said to be disjoint, i.e. assignable to one and only one unit. TI, on the other hand, assumes that under certain conditions complete disjointness is possible so that simply optimizing at the unit level is sufficient for ensuring a system level optimum. The conditions required for TI in these earlier methods (e.g., von Spakovsky and Evans, 1993) included an adequate functional breakdown of the system (i.e. a breakdown into units as described by the functional diagram of EFA or TFA), system and component cost functions and constraints based on exergy and negentropy, and system and component cost functions linearized with respect to each corresponding function's (unit's) product.[1]

However, the practicality of linearazing in very complex systems as well as the negative associated with a possible loss of information makes the use of EFA and TFA in particular and the Evans / El-Sayed formalism in general questionable for achieving TI in such systems. In addition, TI has only been successfully achieved or closely approached using this formalism for very simple systems. Furthermore, none of these methods was developed for units coupled to non-energy systems as is the case in aircraft; and, thus, the

[1] Note that in ILGO which is described later, these conditions are completely eliminated and TI is closely approached by embedding system-level information (i.e. that due to the decision variables which are not disjoint and, thus, exist at the system-level) explicitly at the unit level through the use of coupling functions and their associated shadow prices (see the discussions on LGO and ILGO below). Achieving or closely approaching TI in effect requires that the system-level optimum response surface (again, see the discussions below on LGO and ILGO) is either a hyperplane or a convex hypersurface.

conditions for closely approaching TI were never studied for those cases. Finally, the Evans / El-Sayed formalism indirectly assumes that a single group of analysts has access to and the expertise to work with all of the disciplines and the different technologies (units) that compose the system. This may, in fact, not be the case and more often than not is.

To overcome the difficulties mentioned above and eliminate the conditions required by these earlier methods for achieving or closely approaching TI, a physical decomposition approach called Iterative Local-Global Optimization (ILGO) was developed and utilized for large-scale (i.e. for hundreds of optimization degrees of freedom) aircraft energy system optimization by Muñoz and von Spakovsky (2000, 2001a,b) and later by Rancruel and von Spakovsky (2003). This decomposition strategy is the first to successfully closely approach the theoretical condition of "thermoeconomic isolation" (Frangopoulos and Evans, 1984; von Spakovsky and Evans, 1993) when applied to highly complex, highly dynamic non-linear systems. In 2002, Georgopoulos applied the ILGO method to the optimal synthesis/design and operation of a fuel cell based total energy system. The ability of ILGO to handle large-scale mixed integer nonlinear programming problems for complex transportation and stationary energy system applications was, thus, demonstrated. Rancruel (2005) further developed this decomposition strategy to be fully dynamic, calling Dynamic Iterative Local-Global Optimization (DILGO). He then applied DILGO to the dynamic synthesis/design and operation/control optimization of a 5kWe SOFC auxiliary power unit. (Rancruel, 2005)

2.3 Energy System Control and Dynamic Operation

When considering the operation aspect of an energy system, control is a crucial issue due to the dynamic response, issues of safety, and the complexity of the system. A control system is an interconnection of components forming a system configuration that will provide a desired response. The basis for analysis of a system is provided by linear systems theory, which assumes a cause-effect relationship for the components of a system. The input-output relationship represents the cause-effect of a process, which in turn represents the processing of the input signal to provide an output signal variable. All

control systems consist of the same basic structure and the same basic components as shown in Figure 2.4 (e.g., Franklin, 1991).

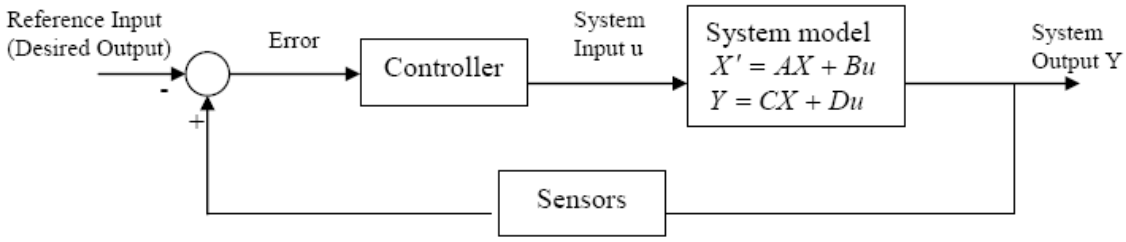

Figure 2.4 Basic structure and components of a control system.

Typically, there are two approaches for the design of control: classical control design and modern control design. Transfer-function-based methods such as root locus and frequency response are referred to as classical control design, whereas state-space approaches are called modern control design. The idea of state-space comes from the state-variable method of describing differential equations. In this method, dynamic systems are described by a set of first-order differential equations in variables called state variables, and the solution may be visualized as a trajectory in space.

Both control design approaches have been utilized in energy system operations. Advantages of state-space design are especially apparent when engineers design controllers for systems with more than one control input or more than one sensed output. Because the variables in an energy system are usually strongly coupled – e.g., pressure, flow rate, etc – a multi-input, multi-output controller may provide the best dynamic response as well as the best system operating efficiency across all possible operating conditions. A further advantage is that the system representation provides a complete description of the system, including possible internal oscillations or instabilities that might be hidden by inappropriate cancellations in the transfer-function description.

Control design is a crucial issue in fuel cell system operations. The response of a fuel cell system to a load requirement depends on the air and fuel feed, flow and pressure regulation, and heat and water management, etc. To study the fuel cell system operations, creating a control-oriented dynamic model of the overall system is an essential first step, not only for the understanding system behavior, but also for the development and design of model-based control methodologies. Some research has been done to generate models

for the purposes of studying the fuel cell system control (e.g., Pukrushpan, Stefanopoulou, and Peng, 2003).

Pukrushpan, Stefanopoulou, and Peng presented a nonlinear fuel cell system dynamic model (no fuel reforming) which is suitable for control study. The transient phenomena captured in the model include the flow characteristics and inertia dynamics of the compressor, the manifold filling dynamics, and consequently, the reactant partial pressures. An observer based feedback and feedforward controller that manages the tradeoff between reduction of parasitic losses and fast fuel cell net power response during rapid current demands in designed. The feedback controller can provide robustness through the integration of the error between the desired and the measured compressor air flow. It also provides a means for calibrating the transient fuel cell net power response and avoiding harmful compressor motor voltage command that can result in stall or surge. They also clarify the origins of the tradeoff between air flow control and system net power.

Varigonda (2003) illustrates the idea that system level dynamic models help in understanding system level interactions, implications for system performance, model-aided controller design, and alternative system architectures in an integrated design and control paradigm. In the study, control theoretic tools such as the relative gain array (RGA) and the observability gramian[2] are employed to guide the control design for a FPS combined with a PEMFC. These tools provide insight into subsystem interactions and can point to the need for system redesign. The observability analysis can help in assessing the relative cost-benefit ratio in adding extra sensors in the system.

Different control strategies and architectures have been studied to improve the dynamic responses of fuel cell systems. Pukrushpan (2003) published the results of the air flow control problem in a fuel cell system based on a control-oriented fuel cell system model. In the study, a combination of non-linear feedforward and linear feedback controllers is designed to regulate the excess oxygen ratio in the cathode during step changes in fuel cell current demand. The feedback controller provides robustness through the integration of the error between the desired and the measured compressor air flow. It

[2] The Observability Gramian is a Gramian used in optimal control theory to determine whether or not a linear system is observable.

also provides a means for calibrating the transient fuel cell net power response and avoiding harmful compressor motor voltage command that can result in stall or surge. Moreover, the study clarifies the origins of the tradeoff between air flow control and system net power. The analysis also suggests a multi-variable control architecture where the power conditioning unit of the fuel cell and the traction motor controller coordinate for better performance.

Suh (2005) presented load following fuel cell systems depending on control of reactant flow and regulation of DC bus voltage during load (current) drawn from them, using decentralized and coordinated control architectures. Model-based control techniques have been employed to tune the two separate controllers for the compressor and the converter. Suh demonstrates that the lack of communication and coordination between the two controllers entails a severe tradeoff in achieving the stack and power output objectives. A coordinated controller is then designed which manages the air and the electron flow control in an optimal way. Results show that the coordination between the compressor and the converter controllers can alleviate the tradeoff between the two performance for the compressor and that for the converter.

The various control design strategies shown above are all for the purpose of system dynamic operation. As discussed in Chapter 1, the typical approach to energy system synthesis/design optimization is based on steady state operation and only verifies transient operation and develops controller architectures once the optimal steady state synthesis/design is established(e.g. Braun, 2002). Braun studied optimal system design and operation strategies for stationary solid oxide fuel cell systems applied to single-family detached dwellings. Optimal cell design voltage, fuel utilization, and operating temperature parameters have been found using minimization of the life cycle costs. His system design evaluations reveal that hydrogen-fueled SOFC systems demonstrate lower system efficiencies than methane-fueled systems. The annual simulations reveal that efficiencies of 45% electric (LHV basis), 85% cogenerative, and simple economic paybacks of 5-8 years are feasible for 1-2 kW SOFC systems in residential-scale applications.

The problem with this approach for highly non-linear, complex, dynamic energy systems is that it ignores the effects which transients and a given control architecture

have on the development of the system, i.e. on its synthesis/design and vice versa. In other words, there is a tight coupling between synthesis/design and operation/control such that changes to one affect the other and changes to the other affect the former. Thus, development of control architecture necessitates taking this coupling into account during the dynamic optimization of a system's synthesis/design and operation. A schematic illustrating such an integrated approach is seen in Figure 2.5.

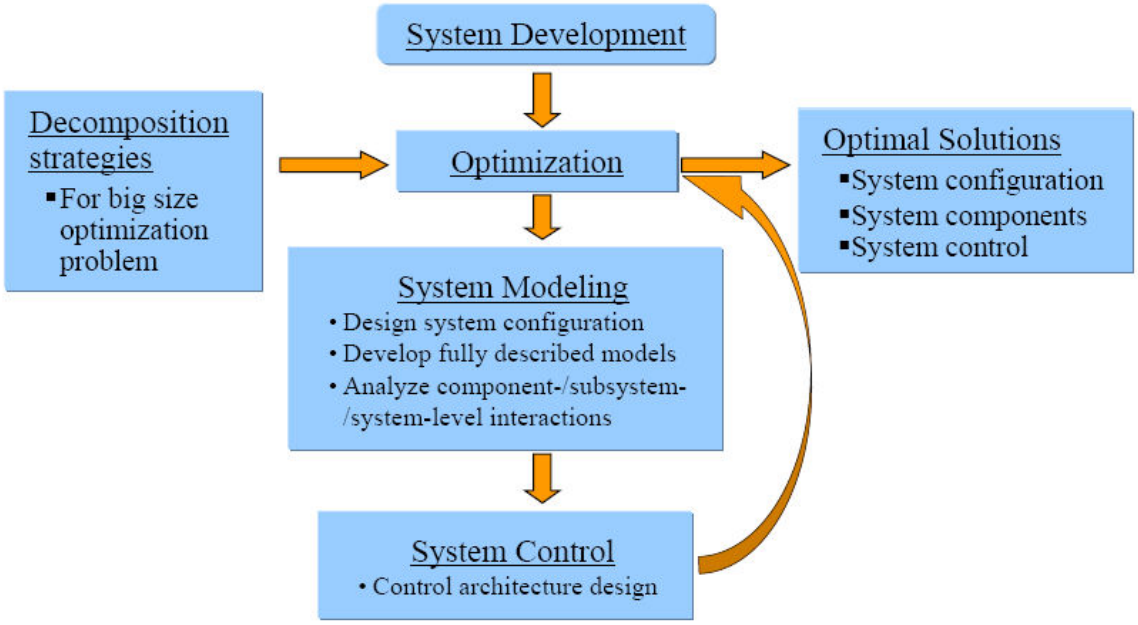

Figure 2.5 Schematic of an integrated approach to energy system development.

2.4 PEM Fuel Cell System Modeling

Different mathematical models of PEM fuel cells and stacks have been developed and are presented in the literature (e.g., Ceraolo, Miulli, and Pozio, 2003, Carlson et al, 2005). The types of fuel cell models which can be used in the kinds of large-scale system optimizations which are of interest here are so-called 0-D (or lumped parameter) and 1-D analytical or semi-empirical models since models of higher dimensionality are computationally to intensive. Of the PEMFC models in the literature, a number of them are able to simulate only steady state cell behavior while others able to simulate the dynamics of the cell are characterized by high complexities (e.g., they are 2-D or 3-D models) which make using them impractical. Ceraolo, Miulli, and Pozio (2003), on the other hand, have developed a dynamic PEMFC model with some simplified semi-empirical equations, based on physical-chemical knowledge of the phenomena occurring

inside the cell and experimental data. The behavior of the proposed model, used with values of the numerical parameters found with the proposed identification procedure, has shown a good agreement with experimental results both in static and dynamic conditions. The model is also structured so that it can be easily extended to a whole stack of fuel cells.

A fuel cell system also requires the integration of many other components beyond the fuel cell stack itself. A FPS is necessary in order to convert conventional fuels, e.g., natural gas, into the hydrogen required by the fuel cell stack. Over several decades, a lot of research has been done with regard to hydrogen production. Steam reforming is the most popular method of converting light hydrocarbons to hydrogen. Xu and Froment (1989) present intrinsic rate equations for the steam reforming of methane accompanied by the water-gas shift reaction on a $Ni/MgAl_2O_4$ catalyst. They derived the intrinsic rate equations for steam reforming of methane as well as the accompanied water-gas shift reaction. A modified collocation method was used in their research to obtain the partial pressure profiles of the reacting components in the catalyst pellet.

Ettouney (1995) have published results for a theoretical analysis about the catalytic reaction of carbon monoxide in both high and low temperature shift reactors. Removing carbon monoxide in a hydrogen rich stream is a critical issue when hydrocarbons are used as the hydrogen source for PEMFCs. Their analysis results show that increase in the steam/gas ratio increases the overall conversion in both HTSR and LTSR. At temperatures higher than the optimum equilibrium favors the reverse of the conversion reaction. Also, increasing the operating pressure has a very limited effect on the overall conversion, especially at high feed temperature. Choi (2004) presents the kinetics of CO preferential oxidation to evaluate various rate expressions and to simulate the performance of the CO oxidation step for fuel cell applications. A three reaction model consisting of CO oxidation, H_2 oxidation, and the water gas shift reaction is considered inside a simple tubular reactor model. They showed that the trend of decreasing CO conversion and selectivity at higher temperatures is accurately predicted to be caused by the reverse water gas shift reaction rather than a difference in the activation energies for CO oxidation and H_2 oxidation. Also, it is shown that adding water should increase the performance of PrOx reactors.

In addition to the FPS, a work recovery and air supple subsystem (WRAS) supplies conditioned air to the PEMFC stack. Typically, air is provided at the appropriate pressure and flow rate for the fuel cell stack and, if present, the fuel processor. The WRAS also recovers energy from the fuel cell exhaust in order to reduce parasitic power required for the WRAS. For example, in 1981, a bootstrap turbocompressor system was built up for phosphoric acid fuel cell power plant by TEPCO, which was applied for 5MW phosphoric acid fuel cell power plant (Hydrogen and Fuel Cells Merit Review, 2003). Several companies in United States have also had various projects on fuel cell WRAS via contracts funded by the U.S. DOE. These projects are presented in the 2002 annual progress report of the Hydrogen, Fuel Cell and Infrastructure Technologies Program, by U.S. Department of Energy, Energy Efficiency and Renewable Energy. For example, one project taken by Mechanology LLC is funded by DOE, which is Development and Testing of High Efficiency Integrated Compressor/Expander Based on Toroidal Intersecting Van Machine (TIVM) Geometry. Their design and analysis of the first generation TIVM compressor/expander has shown that this concept has the potential to meet the DOE requirements for automotive fuel cell applications with better performance than many other options.

Chapter 3

System Configuration and Component Modeling

This chapter describes the PEMFC system configuration and outlines detail of the components modeling done in this doctoral work. Since the system and component models used here are those used in Kim (2008), what is presented and explained in detail in this chapter are the models actually developed by me whereas those developed by Kim are only outlined more briefly. For these, the reader is referred to Kim (2008) for more details.

3.1 Fuel Cell System Configurations

The proposed PEMFC system (Figure 3.1) modeling includes three subsystems: a fuel processing subsystem (FPS), a stack subsystem (SS), and a work recovery and air supply subsystem (WRAS). The SS generates electrical energy from chemical energy, using hydrogen as fuel and air as oxidant. The FPS supplies hydrogen to the SS anode. It consists of a series of chemical reactors, heat exchangers, etc., using methane and water as reactants. The WRAS supplies air to the SS cathode and can also recover energy from the exhaust gases of the SS. The system model is developed taking into account all the equipment and recovery loops necessary to maximize total system efficiency. The power conditioning subsystem is not considered in this research. The details of the models of these three subsystems (which are been marked in Figure 3.1) are given in the following sections. We begin, however, with a description of the overall system configuration. For the overall system, there are two input flows, i.e. methane to the FPS and air to the WRAS; the outputs are electrical power, heat, and exhausting gases (high percentage of CO_2, N_2, and low percentage of H_2O, O_2 without CO, NO_x, or SO_x as an environmental friendly system).

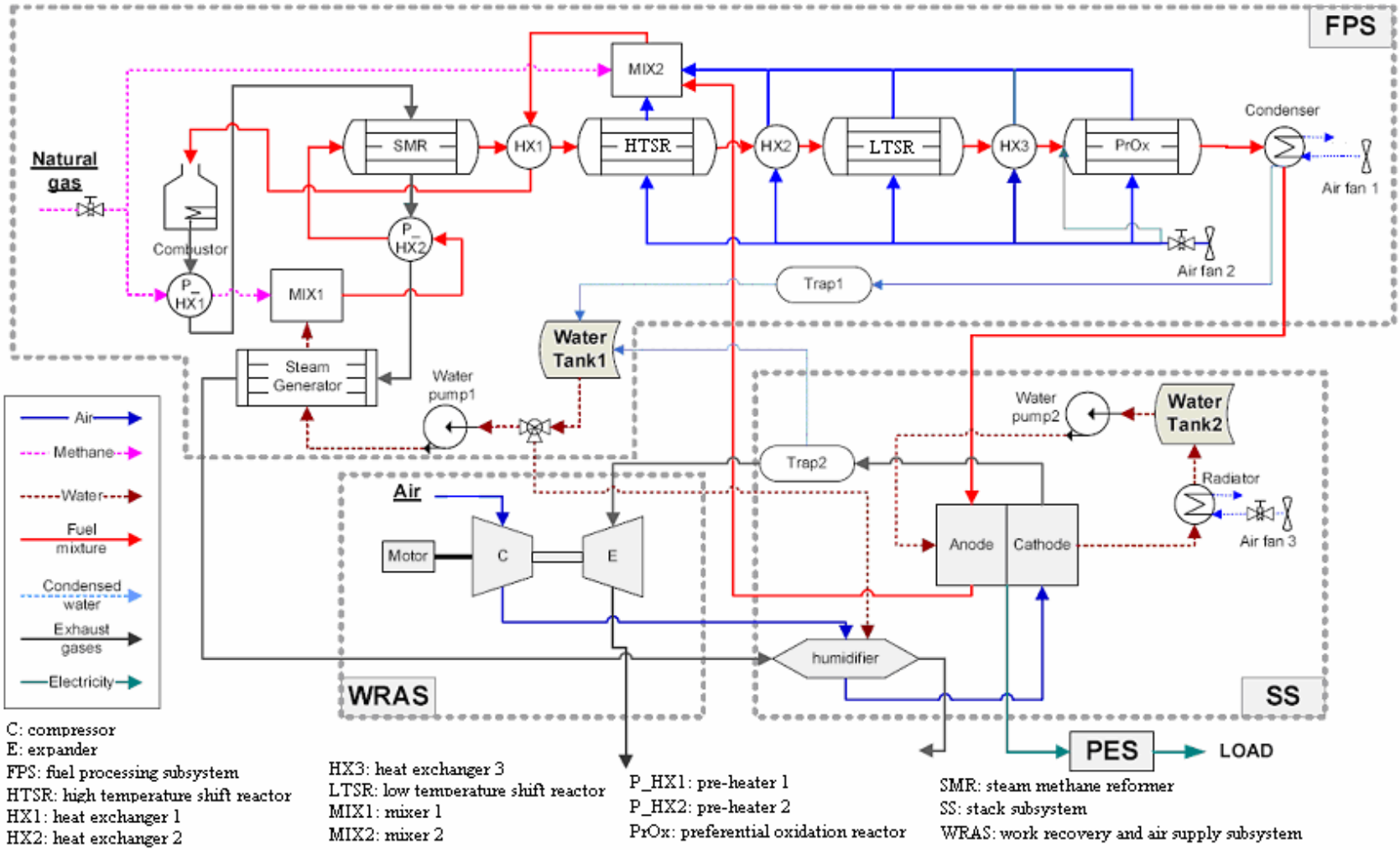

Figure 3.1 PEMFC system configuration (Kim, 2008).

3.2 Modeling of the Stack Subsystem (SS)

The PEMFC stack subsystem, as shown in Figure 3.2, consists of a fuel cell stack and a cooling cycle that incorporates a deionized water supply (developed in the present work). Hydrogen rich fuel flows through the anode side of each cell and the air through the cathode side of each cell. The cooling loop keeps the stack temperature within 60^{o}C to 80^{o}C and prevents a big temperature variation inside the fuel cell stack. The radiator in the cooling loop controls the cooling water temperature.

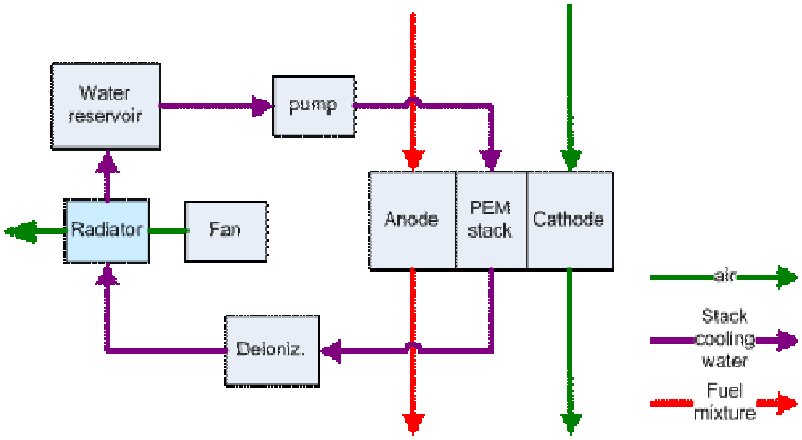

Figure 3.2 Stack subsystem configuration.

3.2.1 Stack Cooling Loop Model

The power consumed by the pump and the fan in the cooling loop of the PEMFC stack is simulated as a function of the stack output power (Boettner and Moran, 2004). In case of considering the change of cooling water temperature through the flow channel, the major reason is to study the temperature variation of the fuel cell stack. As shown in the next section, the proposed fuel cell stack model in this research is a 1-D model (only considering the direction orthogonal to the anode/cathode surface) with constant temperature. Therefore, it is not important to study the water temperature change with this fixed fuel cell stack temperature, as long as the power consumption of the cooling cycle can be calculated.

3.2.2 PEMFC Stack Model

The stack model used in this research is a semi-empirical model which has the capability of simulating both the steady state and transient behavior of a PEMFC. The

cell model is based on that developed by Ceraolo, Miulli, and Pozio (2003) while its extension to a stack model is based on the work of Martin–DuPan. It is a dynamical model which uses knowledge of the chemical-physical phenomena occurring inside the cell and some empirical equations and data.

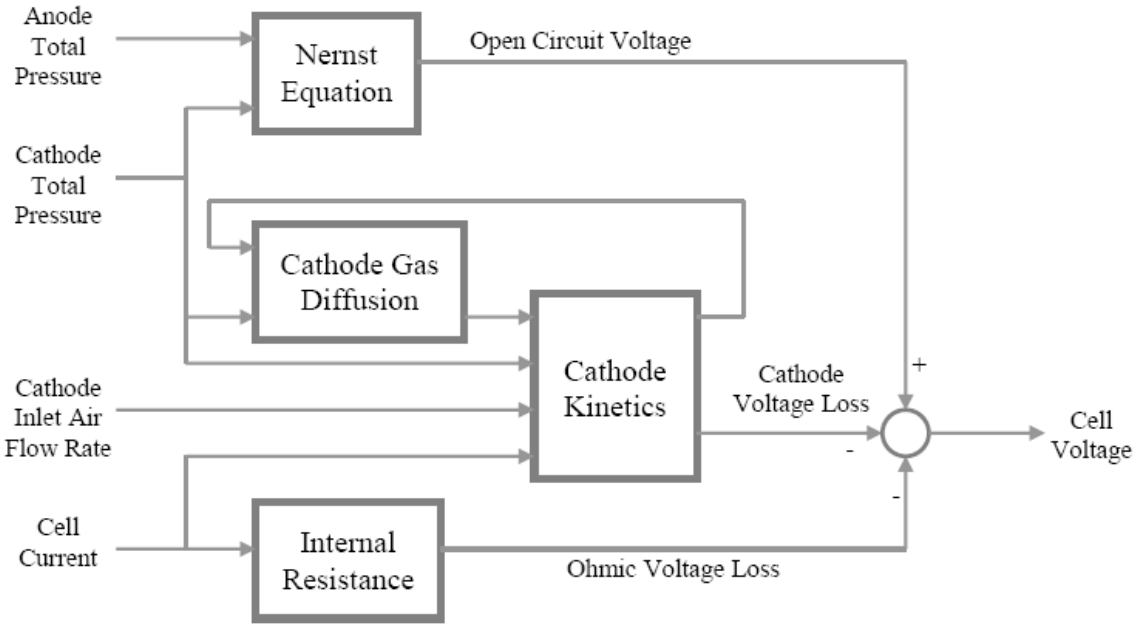

Figure 3.3 The proposed fuel cell model structure.

The main assumptions of this model are as follow:

1. The electrode (diffusion and catalyst) layers have known and constant porosities and tortuosities. This implies that the possibility of cathode flooding is not considered, since it would change the size of the macropores and therefore the layer effective porosity.
2. The model is one-dimensional, i.e. all quantities vary only in the direction orthogonal to the anode and cathode surfaces.
3. The temperature is assumed to be uniform in the cell.
4. The total air pressure is assumed to be uniform, while the special variation with of the partial pressures of its components is taken into account. As a consequence, the movement of the gases within the electrodes only results from concentration and not pressure gradients.
5. The water vapour contained in the reactants in the diffusion (backing) layer macropores is in equilibrium with the surrounding liquid phase; consequently the partial water pressure is uniform.

6. The membrane is considered to be completely saturated with water; therefore, its conductivity is only a function of temperature.
7. The anodic overpotential is disregarded with respect to that of the cathode; consequently, the voltage across the anode is assumed to be constant.

Table 3.1 Gas diffusion model of PEMFC.

Cathode gas diffusion		
p_1	Oxygen partial pressure	From 1. Continuity equations: $\frac{\varepsilon_g}{RT}\frac{\partial p_i}{\partial t}+\frac{\partial N_i}{\partial y}=0$ 2. Stefan-Maxwell equations of diffusion: $\frac{\varepsilon_g}{\tau^2}\frac{\partial p_i}{\partial y}=\sum_{k=1}^{3}\frac{RT}{p_c d_{ik}}\left(p_i N_k - p_k N_i\right)$ where $i,\quad k\in(1,\quad 3),\ p_c = p_1 + p_2 + p_3,$ $p_c d_{ik} = D_{ik}(T)$ to obtain the equation of oxygen partial pressure: $\frac{\partial p_1}{\partial t}=\omega\frac{\partial^2 p_1}{\partial \xi^2}-\psi\frac{j_r}{4F}\frac{\partial p_1}{\partial \xi}$, where $\omega=\frac{1}{\tau^2 L_d^2\left(\left(p_{sat}/D_{12}\right)+\left(p_c-p_{sat}\right)/D_{13}\right)},$ $\psi=\frac{RT}{\varepsilon_g L_d\left(p_c-p_{sat}\right)}$
$p_2 = p_{sat}(T)$	Water vapor partial pressure	
p_3	Nitrogen partial pressure	
p_c	Cathode pressure	
$D_{ik}(T)$	Diffusivity	
ε_g	Diffusion layer porosity	
τ	Tortuosity	
L_d	Thickness of the diffusion layer	
$\xi = y/L_d$	Dimensionless distance in the diffusion layer	

Figure 3.3 illustrates the fundamentals of the purposed model. With cell current and other inlet conditions such as flow rates, temperature, and pressure, this model can be used to calculate voltage losses, cell voltage, and fuel consumption. As shown in the figure, the cell open circuit voltage can be calculated based on anode and cathode pressure. The oxygen partial pressure at the cathode catalyst layer is calculated based on diffusion through the cathode. The cathode overpotential can then be obtained with other information such as air flow rate, cell current, etc. The ohmic loss can also be calculated based on some empirical equations and, subsequently, the cell voltage as well. The hydrogen consumption is determined from the inlet hydrogen flow rate and the cell current.

Details of the model equations for a single cell are shown in Tables 3.1 and 3.2. As to the overall stack model, the same single cell model is added together, i.e. stack voltage is the number of cell times the single cell voltage and the stack current is the single cell current.

Table 3.2 Kinetic, resistance, and voltage models of the PEMFC.

Cathode kinetics, internal resistance and open circuit voltage		
j_r	Reaction current density	$j_r = j_0 A_r \left\{ \frac{p_1}{p_{10}} \frac{[H^+]}{[H^+]_0} \exp\left(\frac{\eta}{b}\right) - 1 \right\}$, where $j_0 A_r = j_{01} A_{r0} \left\{ 1 + \left[\exp\left(\frac{\eta_b}{b_1} - \frac{\eta_b}{b_h}\right) - 1 \right] \cdot u(\eta - \eta_b) \right\}$ $\times \exp\left(-a_1 j - a_2 j^5\right)$ $j_{01} A_{r0} = j_{ref} \exp\left(-\frac{k_0}{T} + \frac{k_0}{T_{ref}} \right) P_{O_2}^{\alpha_0}$ and $\eta = E_{oC} - \Delta\phi_{ce} = E_o - V_{cell} - R_{ohm} j$, $j = j_r + C_{dl} \frac{\partial \eta}{\partial t}$, $\eta_b = E_0 - 0.8$. The behavior over time of the proton concentration is: $u\left(-\frac{\partial c_{H^+}}{\partial t} \right) \cdot \frac{\partial c_{H^+}}{\partial t} + \frac{c_{H^+}}{\tau_{H^+}} = \frac{1 + \alpha_{H^+} \cdot j^3}{\tau_{H^+}}$. The relationship between internal ohmic resistance and temperature is: $R_{ohm} = R_{ref} + \alpha_T (T - T_{ref})$. The open circuit voltage is: $E_o = E_{ref} + \frac{dE}{dT}(T - T_{ref}) + k \frac{RT}{2F} \ln\left(p_{H_2} p_{O_2}^{1/2}\right)$.
p_{10}	Zero-current oxygen partial pressure	
$[H^+]$	Proton concentration	
η	Cathode overpotential	
b	Tafel slope	
j	Cell current density	
E_{oC}	Cathode potential	
C_{dl}	Double layer capacitance	
E_o	Open-circuit voltage	
V_{cell}	Cell voltage	
c_{H^+}	Dimensionless proton concentration	
R_{ohm}	Internal ohmic resistance	
E_{ref}	Reference voltage	

As a 1-D model, the hydrogen and oxygen concentration changes along the flow channels are ignored. Nonetheless, this model still predicts the voltage-current relation very well by utilizing some semi-empirical equations to compromise the reactant concentration reductions based on the inlet flow concentrations. The verification is shown in Chapter 6. However, this generates a problem which is that the fuel utilization does not affect the fuel cell performance in this particular case (it is only based on the inlet condition). Therefore, in the optimization, the fuel utilization is fixed (at 85%) to avoid approaching 100%.

3.3 Modeling of the Fuel Processing Subsystem (FPS)

The fuel processing subsystem (FPS) converts natural gas (methane) mixed with water vapor to a hydrogen rich fuel for the PEMFC stack. The mathematical model of the FPS consists of a set of equations that describe the mass and associated energy flows in each of the lines of the subsystem, based on the chemical reactions inside each reactor and on the laws of conservation of mass and energy for each component in the subsystem. The detailed schematic of the FPS configuration is shown in Figure 3.4.

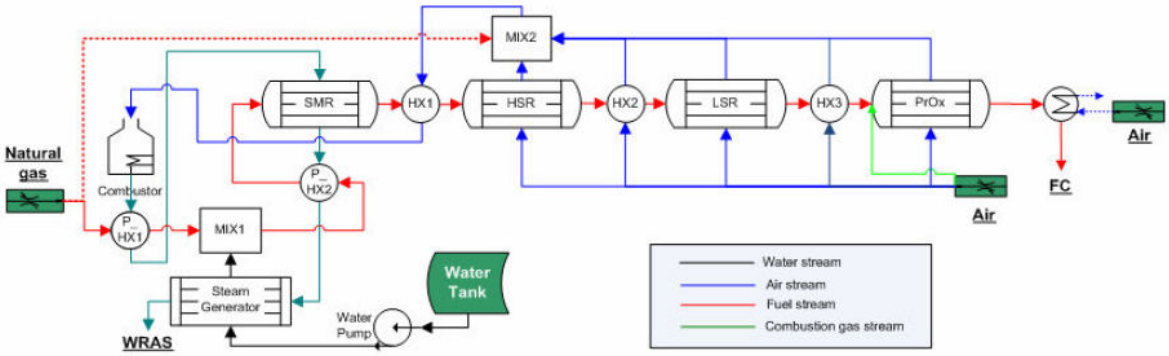

Figure 3.4 Schematic of the fuel processing subsystem configuration.

In this figure, the red line represents the fuel-water mixture stream and the blue line the cooling air flow. In the FPS, the steam generator generates water vapor from liquid water. The water vapor is then mixed with the methane to generate hydrogen rich fuel in steam-methane reformer. After the steam-methane reformer, both high- and low-temperature shift reactors are used to reduce the CO concentration in the fuel mixture and generate more hydrogen at the same time. Finally, extra air is injected into the PrOx to selectively combust the CO and lower its concentration to less than 10 PPM. At the same time, some hydrogen is consumed in the PrOx due to the effect of this combustion. Air is used as the cooling flow to keep each reactor at its proper operating temperature after which it is input to the combustor. The exhausting hydrogen from the SS and extra methane are feed into the combustor to provide energy to the steam generator and the steam methane reformer. A detailed model of each of the components is given in the following sections. However, before proceeding to these sections, a general description of the mathematical models is given.

The mathematical model of each component in the FPS consists of a set of equations that describe the mass and associated energy flows as well as the chemical reactions. For

all of the components and for the case where the subsystem is undergoing a transient process, the conservation of molar mass and energy can be written as follow:

$$\sum_{in} \dot{n}_{mix} - \sum_{out} \dot{n}_{mix} = \frac{dn_{cv}}{dt} \tag{3.1}$$

$$\sum_{q} \dot{Q}_q - \dot{W} + \sum_{in} \dot{n}_{mix} h_{mix} - \sum_{out} \dot{n}_{mix} h_{mix} = \frac{dE_{cv}}{dt} \tag{3.2}$$

where the indices in and out refer to the inlet and outlet flow streams, respectively, and q to the number of heat interactions $\dot{Q}_q$ of the component with other components or subsystems. Moreover, $\dot{W}$ represents the rate of work done by the component, $\dot{n}_{mix}$ the inlet or outlet mixture molar flow rate, and h_{mix} the corresponding mixture specific enthalpy. The terms n_{cv} and E_{cv} refer to the control volume moles and energy.

The mixture's molar flow rate, $\dot{n}_{mix}$, is defined as the sum of the molar flow rates of its constituents, while the corresponding mixture specific enthalpy, h_{mix}, is given by the following relation:

$$h_{mix}(T, \mathbf{y}) = \sum_{p=1}^{7} y_p h_p(T) \tag{3.3}$$

which is valid for a Gibbs-Dalton (ideal gas) mixture. In the above equation, y_p represents the mole fraction of the pth constituent and h_p its corresponding partial enthalpy. Since there are chemical reaction mechanisms that are active within the system, the constituent's partial enthalpy is expressed as

$$h_p(T) = \left(\Delta h_f^o\right)_p + h_p'(T) - h_p'(T_o) \tag{3.4}$$

where $\left(\Delta h_f^o\right)_p$ is the enthalpy of formation of constituent p at standard temperature, T_o, and pressure, P_o. The value of the enthalpy h_p' of the pth constituent is determined by the approximate expression

$$h_p'(T) = a_p T + \frac{4}{5} b_p T^{5/4} + \frac{2}{3} c_p T^{3/2} + \frac{4}{7} d_p T^{7/4} \tag{3.5}$$

which is based on a regression of data from the JANAF Thermochemical Tables (1971). The values of the coefficients a_p, b_p, c_p, and d_p in the above equation are tabulated in

Gyftopoulos and Beretta (1991, 2004). The range of application for this correlation is for temperatures ranging from 300 ^{o}K to 4000 ^{o}K

Chemical equilibrium calculations are necessary in the modeling of the FPS reactor in order to determine in conjunction with the chemical kinetics of each reactor described in the following sections the compositions of their inlet and outlet streams. The equilibrium constant of the reaction, $K(T)$, is defined as

$$K(T) = \exp\left[-\frac{\Delta g^{o}(T)}{RT}\right] \tag{3.6}$$

where $\Delta g^{o}(T)$ is the Gibbs free energy of reaction at temperature T given by

$$\Delta g^{o}(T) = \Delta h^{o}(T) - T\Delta s^{o}(T) \tag{3.7}$$

Here $\Delta h^{o}(T)$ is the enthalpy of reaction at temperature T and pressure P_o, and $\Delta s^{o}(T)$ the entropy of reaction at the same conditions. The values of these functions can be determined by using the following two relations:

$$\Delta h^{o}(T) = \Delta h^{o} + \sum_{p=1}^{7} \nu_p \left[h_p^{'}(T, P_o) - h_p^{'}(T_o, P_o) \right] \tag{3.8}$$

$$\Delta s^{o}(T) = \Delta s^{o} + \sum_{p=1}^{7} \nu_p \left[s_p(T, P_o) - s_p(T_o, P_o) \right] \tag{3.9}$$

where $s_p(T,P) = a_p \ln T + 4b_p T^{1/4} + 2c_p T^{1/2} + \frac{4}{3} d_p T^{3/4} - R \ln P$ (3.10)

(JANAF Thermochemical Table, 1971; Gyftapoulos and Beretta, 1991, 2004) and ν_p is the stoichiometric coefficient of the pth constituent in the reaction. The term Δh^{o}, appearing in equation (3.8), is called the enthalpy of reaction at standard conditions, i.e. $T_o = 25\,^{\circ}$C and $P_o = 1$ atm, and is expressed as

$$\Delta h^{o} = \sum_{p=1}^{7} \nu_p \left(\Delta h_f^{o} \right)_p \tag{3.11}$$

The term Δs^{o}, appearing in equation (3.9), is called the entropy of reaction at standard conditions and is given by

$$\Delta s^{o} = \sum_{p=1}^{7} \nu_p \left(\Delta s_f^{o} \right)_p \tag{3.12}$$

where $\left(\Delta s_f^o\right)_p$ is the entropy of formation of constituent p at standard temperature T_o and pressure P_o.

3.3.1 Modeling of Steam Generator

The steam generator (SG) generates water vapor from liquid water (developed by Kim, 2008). The water phases change from a liquid to a liquid-vapor mixture and finally to a high temperature vapor. The steam generator model considered in this research and shown schematically in Figure 3.5 consists of three sections based on those different phases, i.e. an economizer, an evaporator, and a superheater. The component has been modeled as a cross-flow, shell-and-tube heat exchanger with a single-pass shell and one tube pass. The necessary equations are obtained from Kakaç and Liu (2002) and are the appropriate ones for this particular shell-and-tube configuration. The geometric model of the steam generator is presented in Table 3.3.

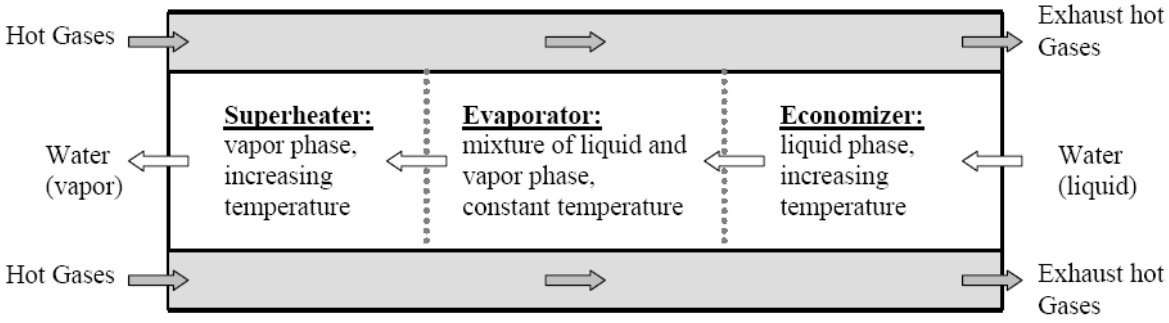

Figure 3.5 Schematic of the steam generator.

The economizer, evaporator, and superheater dynamic models are formulated similarly. In general, the steam generator is discretized spatially into n sections. For each section (index i), a dynamic energy balance for the tube is formulated as follows:

$$\left(mc_p\right)_w \frac{\partial T_{wi}}{\partial t} = \dot{Q}_{gas-wall\,i} - \dot{Q}_{wall-steam\,i} \tag{3.13}$$

where the heat flows are calculate by

$$\dot{Q}_{gas-wall\,i} = \frac{1}{n} U_{gas_i} A\left(T_{gas_i} - T_{wall\,i}\right) \tag{3.14}$$

$$\dot{Q}_{wall-steam\,i} = \frac{1}{n} U_{steam\,i} A\left(T_{wall\,i} - T_{steam\,i}\right) \tag{3.15}$$

The temperatures of the gas and steam for each section of the counter flow heat exchanger are calculated as follow:

$$\dot{Q}_{gas-wall\,i} = \left(\dot{m}c_p\right)_{gas}\left(T_{gas\,i-1} - T_{gas\,i}\right) \tag{3.16}$$

$$\dot{Q}_{wall-steam\,i} = \left(\dot{m}c_p\right)_{steam}\left(T_{steam\,i} - T_{steam\,i+1}\right) \tag{3.17}$$

For the evaporator, the last equation is replaced by

$$\dot{Q}_{wall-steam\,i} = \left(\dot{m}\right)_{steam}\left(h_{steam\,i} - h_{steam\,i+1}\right) \tag{3.18}$$

Table 3.3 Geometric model of the steam generator.

Fixed Parameter Description		**Value**	**Fixed Parameter Description**		**Value**
t_w	Tube wall thickness (mm)	1.5	CTP	Tube count calculation constant	0.93
n_{passes}^{SG}	Number of passes	1	CL	Tube layout constant	1
Variable Description			**Model Equation**		
d_i^{SG}	Tube inner diameter		Assigned value		
n_{tubes}^{SG}	Number of tubes		Assigned value		
L_{SG}	Length		Assigned value		
d_o^{SG}	Tube outer diameter		$d_o^{SG} = d_i^{SG} + 2t_w$		
P_T^{SG}	Pitch		$P_T^{SG} = 1.25 d_o^{SG}$		
D_s^{SG}	Shell diameter		$D_s^{SG} = 0.637\sqrt{\frac{CL}{CTP}}\sqrt{\pi n_{tubes}^{SG}\left(P_T^{SG}\right)^2}$		
B	Baffle spacing		$B = 0.6 D_s^{SG}$		

As far as the heat transfer analysis of the steam generator is concerned, three different heat transfer models are developed and presented on the following pages due to the fact that different convection heat transfer coefficients as well as methods are considered in the design/analysis of its three different parts.

Two different expressions for the tube-side heat transfer coefficient are given depending on whether the water flow inside the tubes is fully developed laminar or turbulent. The correlation used for the shell-side heat transfer coefficient is the one

suggested by Kern (1950). The details of the economizer's heat transfer model are given in Table 3.4.

Table 3.4 Heat transfer model of the economizer.

Variable	Description	Model Equation
Re_{eco}	Tube-side Reynolds number	$\mathrm{Re}_{eco} = \left(\frac{4\dot{n}_{H_2O}}{\pi d_i \mu_{H_2O} n_{tubes}} \right)_{eco}$, $\mathrm{Pr}_{eco} = \left(\frac{\mu_{H_2O} c_{P_{H_2O}}}{k_{H_2O}} \right)_{eco}$
Pr_{eco}	Tube-side Prandtl number	
$h_{H_2O}^{eco}$	Tube-side heat transfer coefficient	If $\mathrm{Re}_{eco} \le 2300$, $h_{H_2O}^{eco} = 4.36 \left(\frac{k_{H_2O}}{d_i} \right)_{eco}$ otherwise, $h_{H_2O}^{eco} = 0.023 \left(\frac{k_{H_2O}}{d_i} \right)_{eco} (\mathrm{Re}_{eco})^{0.8} (\mathrm{Pr}_{eco})^{0.4}$
D_{eq}^{eco}	Shell-side equivalent diameter	$D_{eq}^{eco} = \frac{4\left(P_T^{eco}\right)^2 - \pi\left(d_o^{eco}\right)^2}{\pi d_o^{eco}}$
A_s^{eco}	Bundle cross-flow area	$A_s^{eco} = \frac{D_s^{eco}\left(P_T^{eco} - d_o^{eco}\right)B_{eco}}{P_T^{eco}}$, $G_s^{eco} = \frac{\dot{n}_{gas}}{A_s^{eco}}$
G_s^{eco}	Shell-side mass velocity	
h_{gas}^{eco}	Shell-side heat transfer coefficient (Kerm, 1950)	$h_{gas}^{eco} = 0.36 \left(\frac{k_{gas}}{D_{eq}^{eco}} \right)_{eco} \left(\frac{D_{eq}^{eco} G_s^{eco}}{\mu_{gas}} \right)_{eco}^{0.55} \left(\frac{c_{pgas}\mu_{gas}}{k_{gas}} \right)_{eco}^{1/3} \left(\frac{\mu_{gas}}{\mu_{wall}} \right)_{eco}^{0.14}$
U_{eco}	Overall heat transfer coefficient	$U_{eco} = \frac{1}{\frac{1}{h_{H_2O}^{eco}} + \frac{1}{h_{gas}^{eco}}}$, $A_{eco} = \left(\pi d_o L n_{tubes} n_{passes}\right)_{eco}$
A_{eco}	Heat transfer area	
ΔT_{lm}^{eco}	Log mean temperature difference	$\Delta T_{lm}^{eco} = \frac{\left(T_{gas,i} - T_{H_2O,o}\right)_{eco} - \left(T_{gas,o} - T_{H_2O,i}\right)_{eco}}{\ln\left[\frac{\left(T_{gas,i} - T_{H_2O,o}\right)_{eco}}{\left(T_{gas,o} - T_{H_2O,i}\right)_{eco}}\right]}$
$\dot{Q}_{eco}$	Heat transfer rate	$\dot{Q}_{eco} = \dot{n}_{gas} c_{P_{gas}}^{eco} \left(T_{gas,i}^{eco} - T_{gas,o}^{eco}\right) = U_{eco} A_{eco} \Delta T_{lm}^{eco}$

For saturated convective boiling prior to dry-out, relations to predict the heat transfer coefficient have typically been formulated so as to impose a gradual suppression of nucleate boiling and a gradual increase in liquid film evaporation heat transfer as the

quality increases. A number of correlations based on this approach have been developed. The one recently developed by Kandlikar (1998), which has been fit to a broad spectrum of data for both horizontal and vertical tubes, is used to calculate the tube-side heat transfer coefficient for the evaporator.

Table 3.5 Heat transfer model of the evaporator.

Variable	Description	Model Equation
A_{cr}^{evap}	Cross-sectional area	$A_{cr}^{evap} = \frac{\pi\left(d_i^{evap}\right)^2}{4}$, $G_{tube}^{evap} = \frac{\dot{n}_{H_2O}}{n_{tubes}^{evap} A_{cr}^{evap}}$
G_{tube}^{evap}	Tube-side mass velocity	
Co	Convection number	$Co = \left(\frac{1-\chi}{\chi}\right)^{0.8}\left(\frac{\rho_{H_2O}^{vap}}{\rho_{H_2O}^{liq}}\right)^{0.5}$, $Fr_{le} = \frac{\left(G_{tube}^{evap}\right)^2}{\left(\rho_{H_2O}^{liq}\right)^2 g d_i^{evap}}$
Fr_{le}	Froude number	
Bo	Boiling number	$Bo = \frac{q''_{evap}}{G_{tube}^{evap} h_{fg}}$, $D_{eq}^{evap} = \frac{4\left(P_T^{evap}\right)^2 - \pi\left(d_o^{evap}\right)^2}{\pi d_o^{evap}}$
D_{eq}^{evap}	Shell-side equivalent diameter	
h_{liq}	Heat transfer coefficient for the liquid phase	$h_{liq} = 0.023 \frac{k_{H_2O}^{liq}}{d_i^{evap}}\left(\frac{G_{tube}^{evap}(1-\chi) d_i^{evap}}{\mu_{H_2O}^{liq}}\right)^{0.8}\left(\frac{\mu_{H_2O} c_{pH_2O}}{k_{H_2O}}\right)_{liq}^{0.4}$
$h_{H_2O}^{evap}$	Tube-side heat transfer coefficient	$h_{H_2O}^{evap} = h_{liq}\left[C_1 Co^{C_2}\left(25 Fr_{le}\right)^{C_5} + C_3 Bo^{C_4}\right]$
A_s^{evap}	Bundle cross-flow area	$A_s^{evap} = \frac{D_s^{evap}\left(P_T^{evap} - d_o^{evap}\right) B_{evap}}{P_T^{evap}}$, $G_s^{evap} = \frac{\dot{n}_{gas}}{A_s^{evap}}$
G_s^{evap}	Shell-side mass velocity	
h_{gas}^{evap}	Shell-side heat transfer coefficient	$h_{gas}^{evap} = 0.36\left(\frac{k_{gas}}{D_{eq}^{evap}}\right)_{evap}\left(\frac{D_{eq}^{evap} G_s^{evap}}{\mu_{gas}}\right)_{evap}^{0.55}\left(\frac{c_{pgas}\mu_{gas}}{k_{gas}}\right)_{evap}^{1/3}\left(\frac{\mu_{gas}}{\mu_{wall}}\right)_{evap}^{0.14}$
U_{evap}	Overall heat transfer coefficient	$U_{evap} = \frac{1}{\frac{1}{h_{H_2O}^{evap}} + \frac{1}{h_{gas}^{evap}}}$, $A_{evap} = \left(\pi d_o Ln_{tubes} n_{passes}\right)_{evap}$
A_{evap}	Heat transfer area	
ΔT_{lm}^{evap}	Log mean temperature difference	$\Delta T_{lm}^{evap} = \frac{\left(T_{gas,i} - T_{gas,o}\right)_{evap}}{\ln\left[\frac{\left(T_{gas,i} - T_{H_2O}\right)_{evap}}{\left(T_{gas,o} - T_{H_2O}\right)_{evap}}\right]}$
q''_{evap}	Surface heat flux (single tube)	$q''_{evap} = \frac{\dot{n}_{gas} c_{pgas}^{evap}\left(T_{gas,i}^{evap} - T_{gas.o}^{evap}\right)}{n_{tubes}^{evap} A_{evap}} = \frac{U_{evap}\Delta T_{lm}^{evap}}{n_{tubes}^{evap}}$

The equations for the evaporator's heat transfer model are presented in detail in Table 3.5. As to the heat transfer model of the superheater, this is presented in Table 3.6. The correlations used to calculate the tube-side and shell-side heat transfer coefficients are the same as those appearing in the model for the economizer. It is important to notice that the state of the water along the pipes is tracked by considering its pressure and temperature. This allows one to know the phase change location in order to use the proper heat transfer coefficient in the energy equation.

Table 3.6 Heat transfer model for the superheater**.**

Variable Description		**Model Equation**
$\mathrm{Re}_{\sup er}$	Tube-side Reynolds number	$\mathrm{Re}_{\sup er} = \left(\frac{4\dot{n}_{H_2O}}{\pi d_i \mu_{H_2O} n_{tubes}} \right)_{\sup er}$, $\mathrm{Pr}_{\sup er} = \left(\frac{\mu_{H_2O} c_{P_{H_2O}}}{k_{H_2O}} \right)_{\sup er}$
$\mathrm{Pr}_{\sup er}$	Tube-side Prandtl number	
$h_{H_2O}^{\sup er}$	Tube-side heat transfer coefficient	$h_{H_2O}^{\sup er} = 0.023 \left(\frac{k_{H_2O}}{d_i} \right)_{\sup er} \left(\mathrm{Re}_{\sup er} \right)^{0.8} \left(\mathrm{Pr}_{\sup er} \right)^{0.4}$
$D_{eq}^{\sup er}$	Shell-side equivalent diameter	$D_{eq}^{\sup er} = \frac{4\left(P_T^{\sup er}\right)^2 - \pi\left(d_o^{\sup er}\right)^2}{\pi d_o^{\sup er}}$
$A_s^{\sup er}$	Bundle cross-flow area	$A_s^{\sup er} = \frac{D_s^{\sup er}\left(P_T^{\sup er} - d_o^{\sup er}\right)B_{\sup er}}{P_T^{\sup er}}$, $G_s^{\sup er} = \frac{\dot{n}_{gas}}{A_s^{\sup er}}$
$G_s^{\sup er}$	Shell-side mass velocity	
$h_{gas}^{\sup er}$	Shell-side heat transfer coefficient (Kerm, 1950)	$h_{gas}^{\sup er} = 0.36 \left(\frac{k_{gas}}{D_{eq}^{\sup er}} \right)_{\sup er} \left(\frac{D_{eq}^{\sup er} G_s^{\sup er}}{\mu_{gas}} \right)_{\sup er}^{0.55} \left(\frac{c_{pgas}\mu_{gas}}{k_{gas}} \right)_{\sup er}^{1/3} \left(\frac{\mu_{gas}}{\mu_{wall}} \right)_{\sup er}^{0.14}$
$U_{\sup er}$	Overall heat transfer coefficient	$U_{\sup er} = \frac{1}{\frac{1}{h_{H_2O}^{\sup er}} + \frac{1}{h_{gas}^{\sup er}}}$, $A_{\sup er} = \left(\pi d_o L n_{tubes} n_{passes}\right)_{\sup er}$
$A_{\sup er}$	Heat transfer area	

As introduced above, different equations are utilized in calculating the heat transfer in the three sections of the steam generator (economizer, evaporator, and superheater). However, during dynamic operation, the boundary locations (between the economizer and the evaporator as well as between the evaporator and the superheater) change. This generates computational difficulties during the domain discretization. Therefore, in this

work, the steam generator model applied in the PEMFC system is not transient in terms of the energy balance (the transient terms in the previous equations are set to be zero). Nonetheless, the steam generator guarantees the steam supply (guarantees the existence of the superheater region) during all operating conditions. With this model, there is error in terms of the outlet vapor temperature, but due to the existence of the superheater region, the vapor mass flow rate is still simulated with very good accuracy.

Adiabatic Assumption:

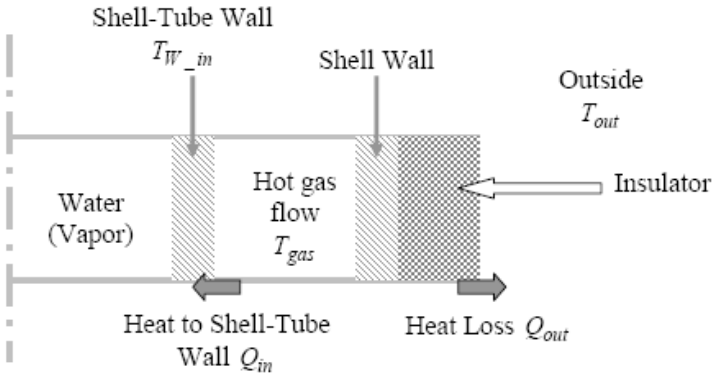

Figure 3.6 Estimation of heat exchanger heat losses.

One assumption of the heat exchanger and reactor models utilized in this research is adiabatic. A brief calculation is then necessary to show the accuracy of this assumption. As shown in Figure 3.6, with the steam generator as an example, the hot gas transfers energy in a heat interaction to both the shell-tube wall side and the shell wall side which causes heat losses to the environment. In a typical condition (full load, steady state), the shell-tube wall average temperature T_{W_in} is about 600 K (considering the water temperature changes from 300 K to around 1000 K), the hot gas flow average temperature T_{gas} 1000 K, and the outside temperature T_{out} 300 K. The convection heat transfer coefficient between the hot gas flow and the wall h_w is about 90 W/m^{2}K, and the natural convection heat transfer coefficient h_{out} 5 W/m^{2}K. Therefore, the heat transfer rate from the hot gas flow to the shell-tube wall is estimated by

$$\dot{Q}_{in} / A = h_w \left(T_{gas} - T_{W_{in}} \right) = 36 kw / m^2 \tag{3.19}$$

and the heat transfer rate from the hot gas flow to the environment is estimated as

$$\frac{\dot{Q}_{out}}{A} = \frac{1}{\frac{1}{h_w} + \frac{L_{shell}}{k_{wall}} + \frac{L_{ins}}{k_{ins}} + \frac{1}{h_{out}}} \left(T_{gas} - T_{W_{in}}\right) = 1.5kw/m^2 \tag{3.20}$$

where the L_{shell}/k_{wall} is ignored compared with the other terms, the thickness of the insulator L_{ins} is 0.01 m, and the insulator thermal conductivity k_{ins} is 0.04 W/mK. Therefore, the adiabatic assumption is reasonable with approximately 4.2% heat loss with the insulator on the shell wall.

3.3.2 Modeling of the Steam-Methane Reformer

Steam-methane reforming (developed by Kim, 2008) is the primary process for the production of hydrogen rich fuel. A schematic of steam-methane reformer model is given in Figure 3.7. This model utilizes a shell-tube heat exchanger structure. The steam-methane mixture flow through the tube side packed with catalyst inside. The hot air, which is on the shell side, supplies heat to the reforming reactions. Both mass and energy balances in the reactor are applied. For the other reactors, i.e. the HTSR, LTSR, and PrOx, the mass and energy balance equations are similar to those in the steam-methane reformer.

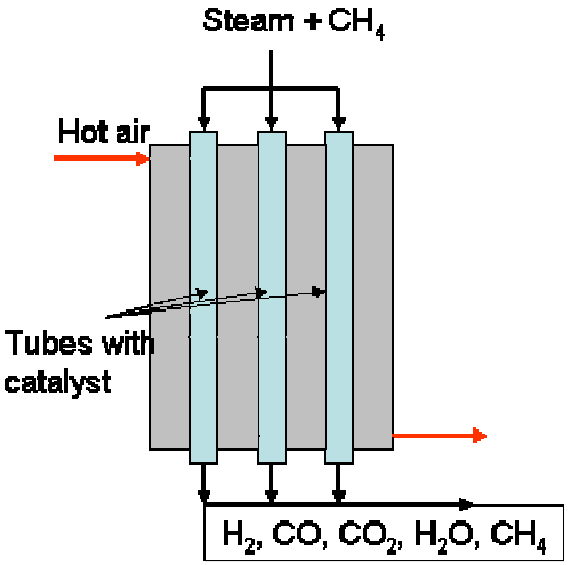

Figure 3.7 Steam-methane reformer model schematic.

There are three dominant reactions which occur in the steam-methane reformer that are considered for:

$$CH_4 + H_20 \Leftrightarrow CO + 3H_2 \tag{3.21}$$

$$CO + H_2 0 \Leftrightarrow CO_2 + H_2 \tag{3.22}$$

$$CH_4 + 2H_2 0 \Leftrightarrow CO_2 + 4H_2 . \tag{3.23}$$

Among the different kinetic rate equations found in the literature for these three chemical reactions, the one developed by Xu and Froment (1989) is used here for the reaction rate of the SMR's kinetic model. They are as follows:

$$r_1 = \frac{\frac{k_1}{P_{H2}^{2.5}}\left[P_{CH4}P_{H2O} - \frac{P_{H2}^3 P_{CO}}{K_{eq_1}}\right]}{DEN^2} \tag{3.24}$$

$$r_2 = \frac{\frac{k_2}{P_{H2}}\left[P_{CO}P_{H2O} - \frac{P_{H2}P_{CO2}}{K_{eq_2}}\right]}{DEN^2} \tag{3.25}$$

$$r_3 = \frac{\frac{k_3}{P_{H2}^{3.5}}\left[P_{CH4}P_{H2O}^2 - \frac{P_{H2}^4 P_{CO2}}{K_{eq_3}}\right]}{DEN^2} \tag{3.26}$$

where $k_i = A_i \exp\left(\frac{-E_i}{RT}\right)$ (3.27)

$$DEN = 1 + K_{CO}P_{CO} + K_{H2}P_{H2} + K_{CH4} + P_{CH4} + K_{H2O}\frac{P_{H2O}}{P_{H2}} \tag{3.28}$$

$$K_j = B_j \exp\left(\frac{-\Delta H_j}{RT}\right). \tag{3.29}$$

The P_i (i=CH_4, H_2O, CO_2, CO, H_2) are the partial pressure of the constituents in the reacting mixture and the K_{eqi} the equilibrium constant associated with each reaction mechanism i. The values of the constants are presented in Table 3.7 and Table 3.8.

Table 3.7 Kinetic parameters.

Reaction No.	$A_i \quad \left[mol \cdot MPa^{0.5} \cdot (g_{cat})^{-1} \cdot h^{-1}\right]$	$E_i \quad \left[kJ \cdot mol^{-1}\right]$
1	$1.336 \cdot 10^{12}$	**240.1**
2	$1.955 \cdot 10^{4}$	**67.13**
3	$3.226 \cdot 10^{11}$	**243.9**

Table 3.8 Absorption constants.

Species	$B_j \quad \left[MPa^{-1}\right]$	$\Delta H_j \quad \left[kJ \cdot mol^{-1}\right]$
CO	$8.23 \cdot 10^{-4}$	**-70.65**
H_2	$6.12 \cdot 10^{-8}$	**-82.90**
H_2O	$1.77 \cdot 10^{5}$	**88.69**
CH_4	$6.65 \cdot 10^{-3}$	**-38.28**

A number of simplifying assumptions are introduced to facilitate the modeling of the SMR. These are outlined below:

- Reforming and combustion gases behave ideally in all sections of the reactor.
- The gas flow pattern through the channels is assumed to be plug flow.
- A uniform temperature exists throughout each catalyst particle.
- No carbon deposition occurs in the SMR reactor.
- Axial dispersion and radial gradients are negligible due to flow rate is much dominant phenomenal than the dispersion and axial gradients is much dominant than the radial gardients.
- The outside shell wall is adiabatic.

The set of mass and energy balances used to model the SMR are given next beginning with the former.

Tube-side mass balance

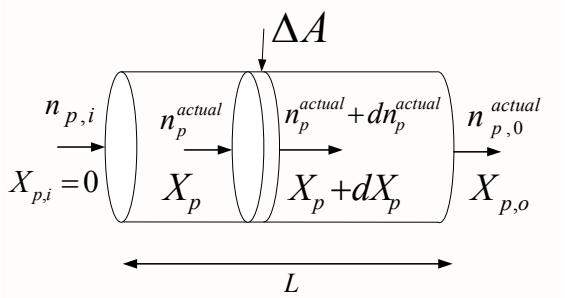

Figure 3.8 SMR control volume and differential discretization.

Figure 3.8 shows the differential control volume over which the mass and energy balances are applied. For plug flow conditions, axial dispersion is assumed to be negligible. Thus, the material balance, which includes transport, reaction, and accumulation of the reforming gas, can be written as

$$\frac{\partial c}{\partial t} = \frac{\partial(-vc)}{\partial x} - R_a \rho_c \tag{3.30}$$

where c is the methane molar concentration (g-mole/m3), v is the superficial velocity (m/hr), R_a is the methane reaction rate per unit mass of catalyst (equals to $r_1 + r_3$, which is the total methane consumption rate from all reactions), ρ_C is the catalyst bed density (kg catalyst / m^3 reactor), x is the axial direction (m), t is time (hr). Let y be the mole fraction of methane and ρ the molar density of the bulk flow. Then, $c = \rho y$ and the concentration balance is replaced by

$$\frac{\partial \dot{n} M y}{\partial x} - R_a \rho_C \frac{\pi d^2}{4} = \frac{\pi d^2}{4}\left(\rho \frac{\partial y}{\partial t} + y \frac{\partial \rho}{\partial t}\right) \tag{3.31}$$

where $\dot{n}$ is the molar flow rate inside the reactor (g-mole/hr) and d is the inside diameter of a give tube (m). Now the mole flow, density, methane mole fraction, and methane conversion along the reactor length are given, respectively, by

$$\dot{n} = \dot{n}_0 + 2X_1\dot{n}_1 \tag{3.32}$$

$$\rho = \frac{P}{RT}\left(\frac{\dot{n}}{\dot{n}_0}\right) \tag{3.33}$$

$$Y = \frac{\dot{n}_1(1 - X_1)}{\dot{n}_0 + 2X_1\dot{n}_1} \tag{3.34}$$

$$X_1 = \frac{\dot{n}_1 - \dot{n}_0 Y}{\dot{n}_1 + 2Y\dot{n}_1} \tag{3.35}$$

where X_1 is the methane conversion, $\dot{n}_0$ is the initial total molar flow outside of the reactor, and $\dot{n}_1$ is the initial methane flow rate.

Tube-side pressure drop

The pressure drop along the catalyst bed (along the tube) is given by (Scott, 1999)

$$\frac{\partial P_i}{\partial x} = \frac{-G_x}{\rho_x g D_p}\frac{1-\phi}{\phi^3}\left[\frac{150(1-\phi)\mu}{D_p} + 1.75G_x\right] \tag{3.36}$$

where $G_x = \rho_x v$ (3.37)

and ρ is the gas density, D_p is the catalyst particle equivalent average diameter, g is the acceleration of gravity, μ is the gas viscosity, and ϕ is the void factor (1-ϕ is the ratio of

catalyst total volume over tube total volume). The pressure drop on the shell-side is ignored in this model due to relatively small pressure drop without catalyst packed in.

SMR Energy balances

Energy balances for the tube-side of the reformer, for the tube-wall, for the combustion gases (shell–side), and for the catalyst are given next.

Tube-side energy balance:

The reformer tube-side energy balance includes the reformate gas sensible enthalpy change, reaction enthalpies, heat transfer from the hotter tube-wall, heat transfer from the catalyst particles, and the accumulation or storage term. The energy equation is as follows:

$$-\frac{\partial\left(\dot{n}c_pT\right)}{\partial x}=h_iA_i\left(T_w-T\right)+h_cA_cA_i\left(T_c-T\right)-A_ic_p\frac{\partial\left(\rho T\right)}{\partial t}-\frac{\partial\left(\dot{n}h_{mix}\right)}{\partial x} \tag{3.38}$$

where c_p is the specific heat of the tube-side flow (J/g-mole-K), A_c is the external surface area of particles per volume of catalyst bed (m^3/m^2), T_c is the catalyst temperature (K), h_i is the inside heat transfer coefficient (J/hr-m-K), h_c is the catalyst-fluid heat transfer coefficient (J/hr-m-K), ΔH_1 the demethanation reaction enthalpy (J/g-mole CH_4), and ΔH_2 the water-gas shift reaction enthalpy (J/g-mole CO). The reaction enthalpies are evaluated at the reactor average temperature. Negative values indicate an exothermic reaction. The heat transfer coefficients (h) are a function of the characteristics of the fluid and the geometry of the reactor.

Shell-side energy balance:

The energy balance equation for the shell-side gas includes sensible enthalpy change, heat transfer with the tube wall, and accumulation of internal energy. It can be written as

$$\rho_0A_0c_{p0}\frac{\partial T_0}{\partial t}=-\rho_0V_0A_0c_{p0}\frac{\partial T_0}{\partial x}-h_0A_0\left(T_0-T_w\right) \tag{3.39}$$

where A_0 is the heat transfer area, ρ_0 is the gas density, T_0 is the gas temperature, T_w is the tube wall temperature, h_0 is the heat transfer coefficient.

Tube wall energy balance:

The energy balance for the tube wall includes convective heat transfer with the reformate gas and shell-side gas (combustion gases) and accumulation of internal energy. This balance is written as

$$\rho_w\left(d_0^2 - d_i^2\right)c_{p_w}\frac{\partial T_w}{\partial t} = 4h_0 d_0\left(T_0 - T_w\right) - 4h_i d_i\left(T_w - T_i\right) \tag{3.40}$$

where d_0 and d_i are the external and internal diameters of the tube, respectively, ρ_w is the metal density, T_0 is the reformate gas temperature, T_w is the tube wall temperature, T_i is the combustion gases temperature, h_0 is the reformate gas-side heat transfer coefficient, h_i is the combustions gas side heat transfer coefficient, and c_{p_w} is the wall specific heat.

Catalyst energy balance:

The energy balance equation for the catalyst is given by

$$c_{p_C}\rho_C\frac{\partial T_C}{\partial t} = h_C A_C\left(T - T_C\right) \tag{3.41}$$

where ρ_C is the catalyst density, T is the reformate gas temperature, A_C is the external surface area of the particles per volume of the catalyst bed (m^3/m^2), T_C is the catalyst temperature (K), h_C is the catalyst-fluid heat transfer coefficient (J/hr-m-K), and c_{p_C} is the catalyst specific heat.

3.3.3 Modeling of the High- and Low-Temperature Shift Reactors

Carbon monoxide is generated simultaneously with hydrogen during the process of methane-steam reforming. Both high- and low-temperature shift reactors (developed in the present work and Kim, 2008) are used to remove CO from the hydrogen rich stream and to generate more hydrogen. The structures of these two reactors like the SMR are also shell-tube heat exchangers.

The chemical kinetics inside high- and low-temperature shift reactors is that given by Ettouney (1991). The dominant reaction occurring inside both shift reactors are the same, i.e.

$$CO + H_2O \rightarrow CO_2 + H_2 . \tag{3.42}$$

The reaction rate of the water-gas shift reaction inside the high-temperature shift reactor (HTSR) is

$$-r_{CO} = K_{Hs} \exp\left(\frac{E_H}{R}\left(\frac{1}{T_{Hs}} - \frac{1}{T}\right)\right) P^{0.5} x_{CO}\left(1 - \frac{K}{K_{eq}}\right), \tag{3.43}$$

where K_{Hs} is the standard catalyst activity. For P<10 atm, K_{Hs}=42.669 gmole CO_2/s $atm^{1/2}m^3$; and for P>10 atm, K_{Hs}=37.870 gmole CO_2/s $atm^{1/2}m^3$. In this equation, T_{Hs} is named the standard temperature and is equal to 706.15 K, E_H is the activation energy and is equal to 11,500 cal/gmole, x_{CO} is the mole fraction of the CO in the reformate stream, and K is defined by

$$K = \frac{x_{H_2} x_{CO_2}}{x_{CO} x_{H_2O}}. \tag{3.44}$$

The reaction rate of the water-gas shift reaction inside the low temperature shift reactor is

$$-r_{CO} = \frac{513.15}{T} \frac{K_L x_{CO} x_{H_2O}^{1/2}\left(1 - K/K_{eq}\right)}{\left(1/P + K_A x_{CO} + K_B x_{CO_2}\right)} \tag{3.45}$$

where r_{CO} is in gmol/m^3cat.s, and the rate constants, K_L, K_A, and K_B, are defined as

$$K_L = K_{LS} \exp\left(\frac{E_L}{R}\left(\frac{1}{T_{LS}} - \frac{1}{T}\right)\right) \tag{3.45a}$$

$$K_A = K_{AS} \exp\left(\frac{E_A}{R}\left(\frac{1}{T_{AS}} - \frac{1}{T}\right)\right) \tag{3.45b}$$

$$K_B = K_{BS} \exp\left(\frac{E_B}{R}\left(\frac{1}{T_{BS}} - \frac{1}{T}\right)\right). \tag{3.45c}$$

In the above equations, E_L/R, E_A/R and E_B/R are equal to -3620 K, -4580 K and -1500 K, K_{LS}, K_{AS}, and K_{BS} have values of 68.4 gmole CO/m^3s atm, 4.31 atm^{-1} and 1.35 atm^{-1}, and T_{LS}, T_{AS}, and T_{BS} are equal to 513.5 K.

3.3.4 Modeling of the CO Preferential Oxidation Reactor (PrOx)

It is critical to remove sufficient amount of CO in the hydrogen rich reformate stream exiting the LTSR since even small amounts of CO (greater than 10 ppm) will poison the electrodes catalysts of the PEMFC stack. Among the various methods for removing CO selectively, catalytic oxidation is considered as one of the most plausible and economical options. This is accomplished via a CO preferential oxidation (PrOx) reactor (developed in the present work and Kim, 2008). The chemical kinetics inside the PrOx model used here is that found in Choi (2003). The following three reactions occur inside the reactor:

$$CO + \frac{1}{2}O_2 \rightarrow CO_2 \qquad \Delta H^0_{298} = -283 \text{ kJ/mol} \tag{3.46}$$

$$H_2 + \frac{1}{2}O_2 \rightarrow H_2O \qquad \Delta H^0_{298} = -242 \text{ kJ/mol} \tag{3.47}$$

and $$CO + H_2O \rightarrow CO_2 + H_2 \qquad \Delta H^0_{298} = -41.1 \text{ kJ/mol.} \tag{3.48}$$

Table 3.9 A sample calculations of the mole fractions of the constituents entering/exiting each reactor.

	SR		HSR	LSR	PrOx
Operating condition	~ 800 ℃ & 3 bar (S/C = 3.6)		~ 500 ℃ & 3 bar	~ 250 ℃ & 3 bar	~ 110 ℃ & 3 bar
Mole Fraction	**Inlet**	**Outlet**	**Outlet**	**Outlet**	**Outlet**
CH_4	0.33	0.0019	0.00190	0.0190	0.00181
H_2O	0.67	0.3355	0.31518	0.31518	0.29047
CO	0.00	0.0885	0.04343	0.00767	8 ppm
CO_2	0.00	0.0617	0.09591	0.13193	0.13376
H_2	0.00	0.5124	0.54358	0.57935	0.54990
O_2	5% of O_2 **fed before PrOx**				0.02510
SO_x	Under 200 ppbv exiting the desulphuriser				
NO_x	Essentially free from NO_x generation (NO_x = parts/ 10^{-15} at equilibrium)				

The semi-empirical kinetic rate expressions for these three reactions are

$$-r_1 = 3.528\times10^2 \exp\left(\frac{-33092}{RT}\right) P_{O_2}^{0.5} P_{CO}^{-0.1} \tag{3.49}$$

$$-r_2 = 2.053\times10 \exp\left(\frac{-18742}{RT}\right) P_{O_2}^{0.5} \tag{3.50}$$

$$-r_3 = 4.402\times10^3 \exp\left(\frac{-33104}{RT}\right) \times \left(P_{CO}P_{H_2O} - \frac{P_{CO_2}P_{H_2}}{K_P}\right). \tag{3.51}$$

with $K_p = \exp\left(\frac{4577.8}{T} - 4.33\right)$ (3.51a)

where the P_i (i=CO, H_2O, CO_2, H_2) are the partial pressure of the constituents "i" in the reformate stream. Table 3.9 shows an example case result of modeling steam-methane mixture running through reactors to generate hydrogen, in which SR, HTSR, LTSR and PrOx represent steam-methane reactor, high temperature shift reactor, low temperature shift reactor and preferential oxidation reactor respectively.

3.3.5 Modeling of the Heat Exchangers, Mixers, and Combustor

The heat exchangers (developed in Kim, 2008) used in the FPS are corrugated type compact heat exchangers (Kim, 2005). Figure 3.9 shows the spatial discretization of the compact heat exchanger model applied in this research, which considers 2-D flow (i.e. x direction for hot gas and y direction for cold gas), and i and k represent the number of discrete segments. Governing equations from (3.52) to (3.52) for describing the compact heat exchanger are considered independently at each segment, and outlet temperatures of each segment are calculated based on the two inlet temperatures. The two outlet temperatures of a segment become inlet temperatures of neighbor segments. Therefore, outlet temperatures along the cold gas and hot gas sides can be calculated.

The following energy balance equations are applied to the cold gas side, hot gas side, and heat exchanger plates for the compact heat exchanger, and cross-flow configuration is used here.

For the hot gas side, the balance is

$$\left(\frac{\dot{n}c_p}{V}\right)_h \frac{\partial T_h}{\partial t} = \left(\dot{n}c_p\right)_h \frac{\partial T_h}{\partial x} + \left(hL_y\right)_h \left(T_h - T_w\right) \tag{3.52}$$

where $\dot{n}$ is the molar flow rate, V the flow velocity, T_h the bulk temperature, T_w the wall temperature, L_y the plate width on the cold gas side, and h_h the convective heat transfer coefficient (see equation (3.56) below).

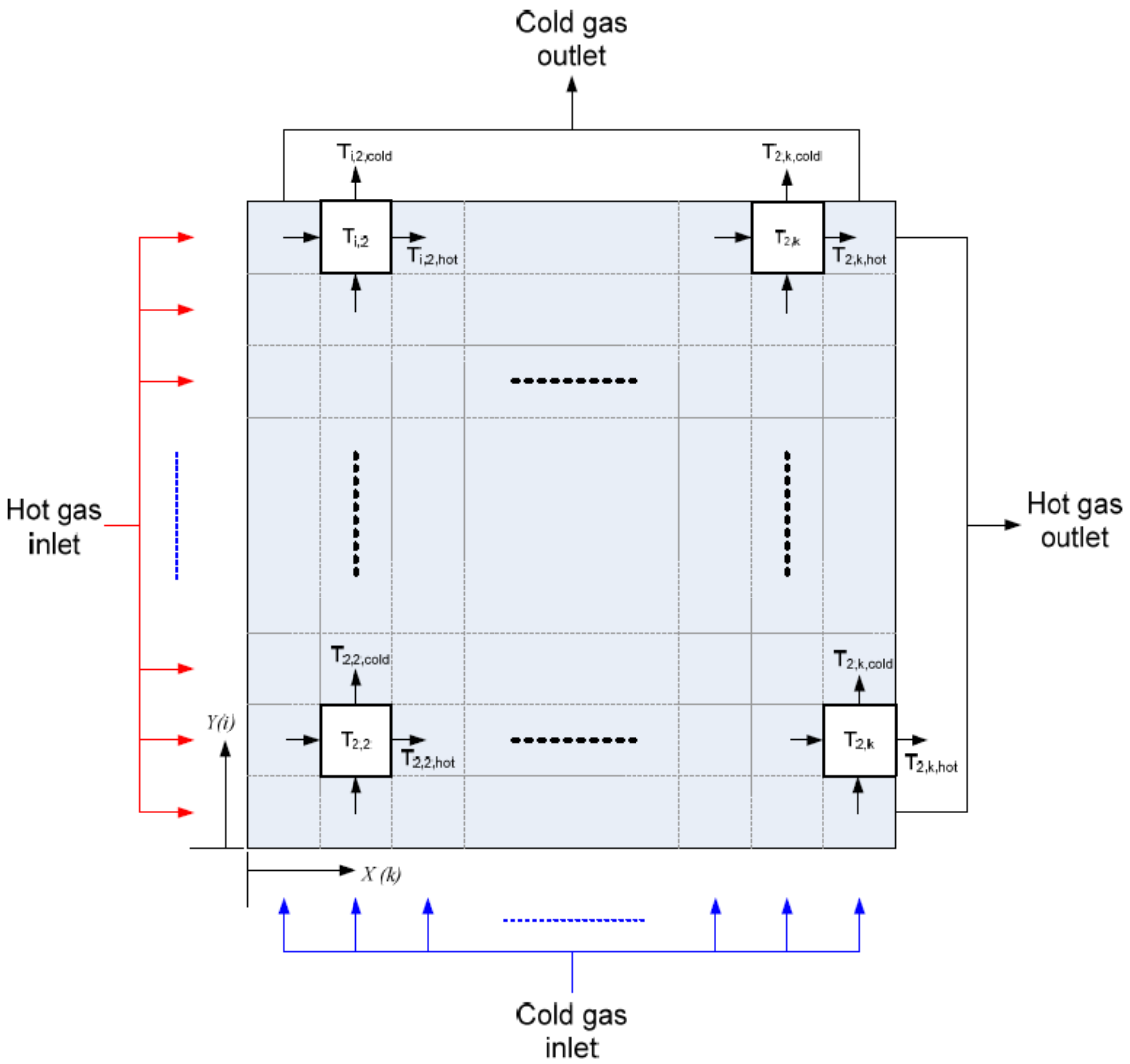

Figure 3.9 Compact heat exchanger spatial discretization (Kim, 2008).

On the cold gas side, the energy balance can be expressed similar to that of hot gas side energy balance as

$$\left(\frac{\dot{n}c_p}{V}\right)_c \frac{\partial T_c}{\partial t} + \left(\dot{n}c_p\right)_c \frac{\partial T_c}{\partial y} + \left(hL_x\right)_c \left(T_c - T_w\right) \tag{3.53}$$

where T_c is the bulk temperature, L_x the plate width on the hot gas side, and h_c the convective heat transfer coefficient (see equation (3.54) below).

The energy balance on the plate and is

$$\left(mc_p\right)_w \frac{\partial T_w}{\partial t} = \left(hA\right)_c \left(T_c - T_w\right) + \left(hA\right)_h \left(T_h - T_w\right) \tag{3.54}$$

where m is the mass of the plate and A is the plate surface area.

Finally, the modeling of the pressure losses in the dimpled-type compact heat exchanger uses the following friction factor f correlation:

$$f = 3.867\,\mathrm{Re}^{-0.196} \tag{3.55}$$

and the heat transfer coefficients are determined from:

$$Nu = 0.122\,\mathrm{Re}^{0.724}\,\mathrm{Pr}^{1/3} \tag{3.56}$$

The mass and energy balance equations for the mixer (see Figure 3.10) are given by equation 3.55, and 3.56 (developed in Kim, 2008). The outlet mass flow rate and temperature are calculated based on the inlet flow conditions, with assumptions of no time delay, and no energy losses through the mixer walls.

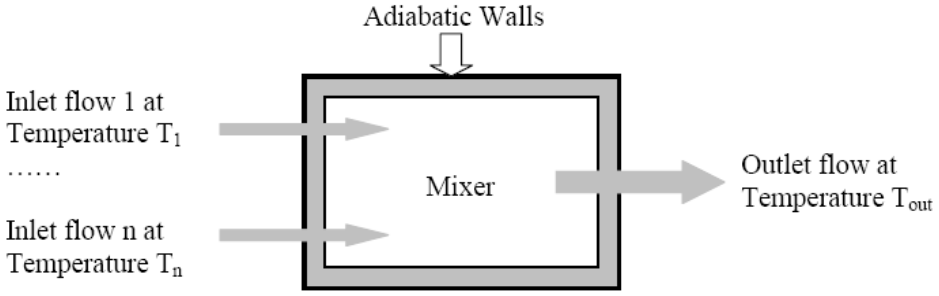

Figure 3.10 Mixer schematic.

$$\dot{m}_{i\_in} = \dot{m}_{i\_out} \tag{3.57}$$

$$\sum_{in} \dot{m}_{i\_in} h_{i\_in}\left(T_{i\_in}\right) = \sum_{out} \dot{m}_{i\_out} h_{i\_out}\left(T_{out}\right) \tag{3.58}$$

The i represents different components mixed the mixer (e.g., CH_4, H_2, O_2, N_2, etc). In equation 3.57, the $\dot{m}_i$ is mass flow rate of component i, which is constant through the mixer. In equation 3.56, the h_i represents enthalpy as a function of temperature (different inlet flow has different temperature; the outlet flow is at the same temperature, T_{out}).

The combustor (see Figure 3.11) model's mass and energy balances between the reactants and the productions are expressed as equation 3.59 and 3.60 (developed in Kim, 2008). The combustion time is ignored and the assumption of no heat loss through the combustor walls.

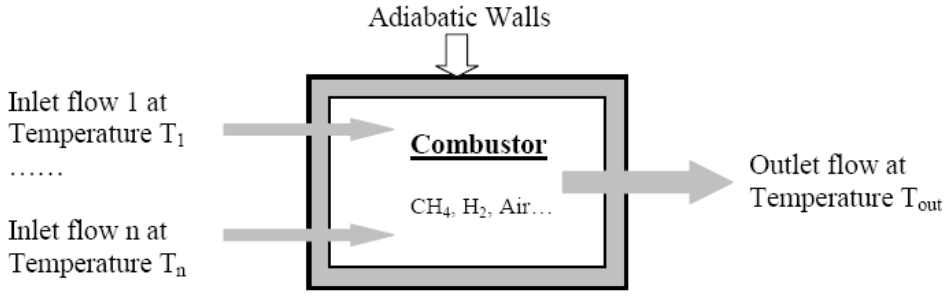

Figure 3.11 Combustor schematic.

$$\dot{m}_{non\_comb\_in} = \dot{m}_{non\_comb\_out} \tag{3.59a}$$

$$\dot{m}_{react\_in} = \dot{m}_{prod\_out} \tag{3.59b}$$

$$\sum_{in} \dot{m}_{i\_in} h_{i\_in}\left(T_{i\_in}\right) = \sum_{out} \dot{m}_{i\_out} h_{i\_out}\left(T_{out}\right) \tag{3.60}$$

For non-combust component (e.g., N2), the outlet flow rate equals to the inlet flow rate, as equation 3.59a. For combust component (e.g., CH_4 and O_2), the production outlet flow rate equals to the reactant inlet flow rate, as equation 3.59b. In equation 3.60, the h_i represents enthalpy as a function of temperature (different inlet flow has different temperature; the outlet flow is at the same temperature, T_{out}).

3.4 Modeling of the Work Recovery and Air-Supply Subsystem (WRAS)

3.4.1 Description of the WRAS

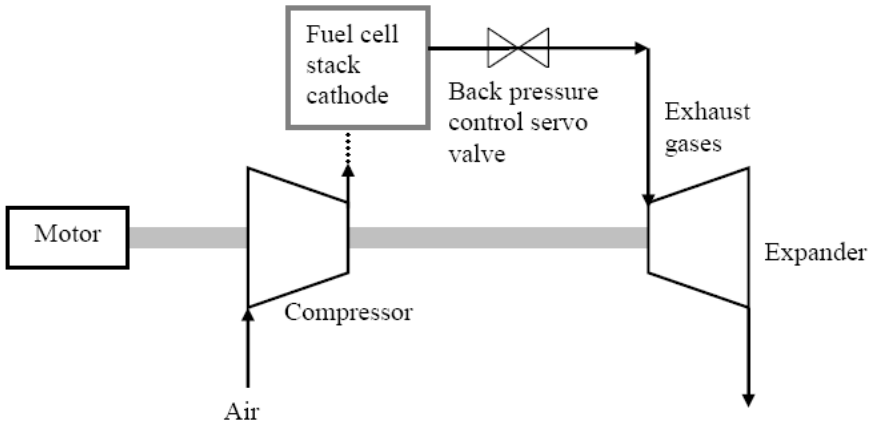

Figure 3.12 WRAS schematic.

The WRAS supplies air to the fuel cell system and recoveries energy from the exhaust gases exiting the fuel cell system (developed in the present work and Kim, 2008). Figure 3.12 shows the WRAS which consists of a compressor (C), an electric motor and an

expander (E). The compressor provides air to the fuel cell cathode. It is driven by the electric motor and the expander. The electric motor is used to supply power to the compressor and control the shaft speed of the compressor. The expander is fed with exhaust gases from the stack to recover some of the energy from this exhaust in order to offset some of the work required by the compressor to which the expander is coupled. Details of the WRAS model are given below.

3.4.2 Modeling of the Positive Displacement Machines

Screw compressor is chosen in this PEMFC system to supply air. Although screw compressors are expensive to manufacture, they provide the oil-free output required by a fuel cell system and provide an extended range of pressure ratios. In addition, they operate at a high efficiency over a wide range of flow rates. The screw compressor performance map used in the model simulation is based on Larmine and Dicks (2003). Figure 3.13 below shows the performance map for the screw compressor based on four dimension less groups, namely, the pressure ratio, the mass flow factor equal to $\dot{m}\sqrt{T_1}/P_1$, the rotor speed factor equal to $N/\sqrt{T_1}$, and the compressor efficiency

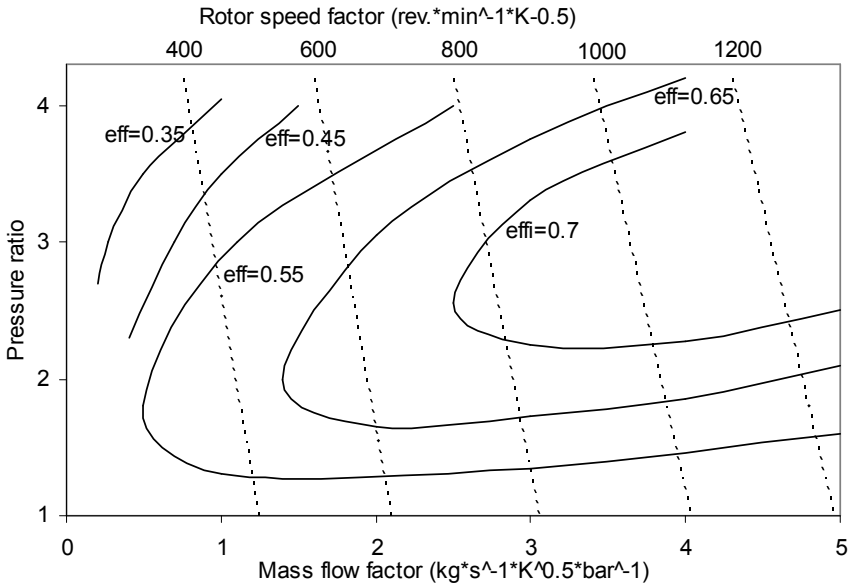

Figure 3.13 Screw compressor performance map.

Since it was not possible to find such a map in the literature for the expander coupled to the compressor, the compressor map with modifications was used for the screw expander model. These modifications entailed the change of slope of the rotational speed

factor lines from negative for the compressor to positive for the expander, as shown in Figure 3.14.

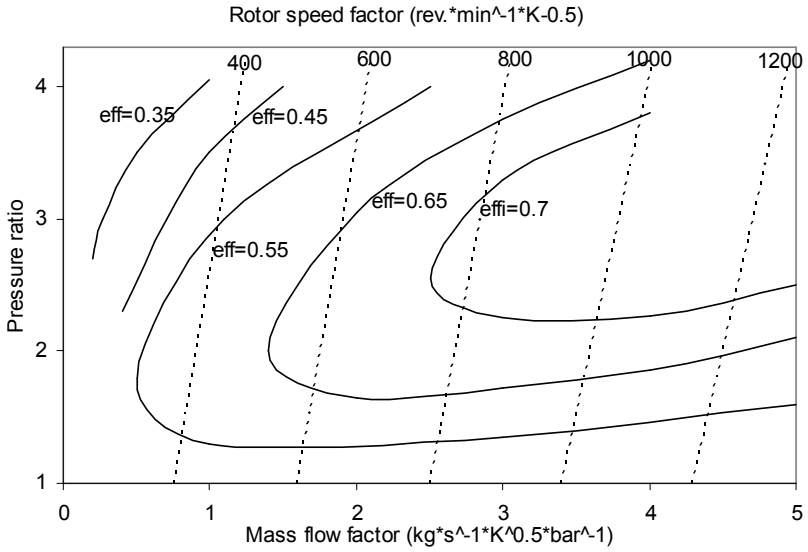

Figure 3.14 Expander performance map.

3.4.3 Modeling of the Electric Motor

Direct current (dc) motors are used where a source of dc voltage is available and variable-speed motor operation is required. Motor speed can be varied by controlling the applied armature voltage, applied field voltage, or both.

The basic equations for modeling the motor are taken from the Handbook of Electric Motors (2004). The expressions relating motor torque, current, and voltage on the electrical side of the motor are given by

$$T = Ki_a \tag{3.61}$$

$$E_a = K\omega \tag{3.62}$$

and $$v_a = R_a i_a + L_a \frac{di_a}{dt} + E_a \tag{3.63}$$

where T is the torque which is related linearly to the armature current, i_a the armature current, E_a the voltage generated by a dc motor armature winding which is the back electromotive-force voltage proportional to the motor speed, ω the angular speed of the armature, v_a the armature voltage, R the armature circuit resistance, L_a the armature circuit inductance, and K the machine constant. Equation 3.63 is the relation between the

input voltage (v_a) and the armature current (i_a), which shows the total input voltage is been used to overcome the pure electrical resistance (i.e. $R_a i_a + L_a \frac{di_a}{dt}$) and the resistance generated by the rotation (i.e. E_a).

The basic mechanical equation is

$$J\frac{d\omega}{dt} = T - D\omega - T_L \tag{3.64}$$

where J is the inertia of the armature (motor shaft inertia and the load inertia). There are internal frictional effects in the motor and the load, resulting in a torque (given by $D\omega$) that is directly proportional to the angular speed. Because most of these effects are small compared to the torques required by the load (T_L), usually, the proportionality coefficient D is set to be a small constant.

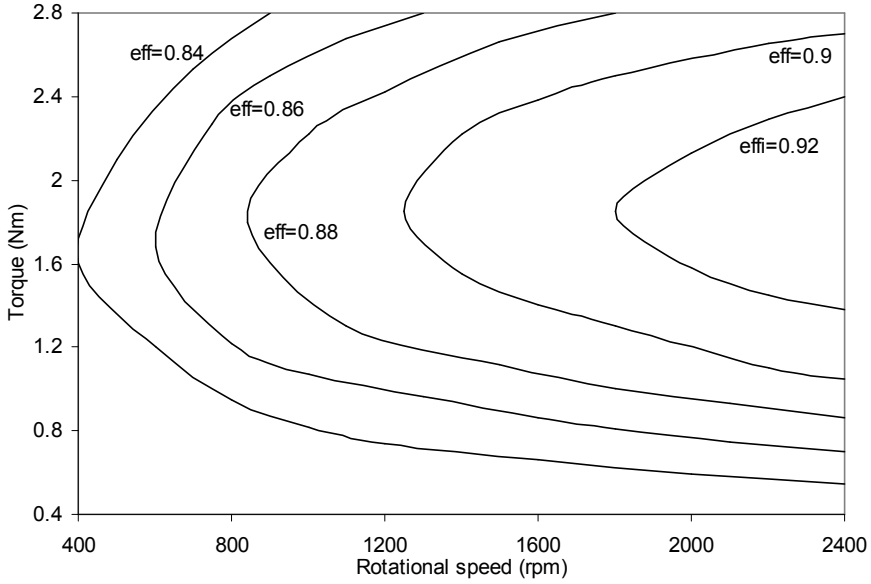

Figure 3.15 Performance map of the brushless DC motor.

In the model, the compressor and the expander are directly coupled to the same shaft, but they are not directly coupled to the motor. The gear ratio between the motor and compressor-expander is, thus, expressed as

$$N = N_m / N_{ce} \tag{3.65}$$

where N_m is the number of teeth on the gear on the motor shaft while N_{ce} is the number of teeth on the load shaft (i.e. compressor-expander shaft). The load inertia will affect the

total inertia J in equation 3.62 by J_L / N^2, where N is the gear ratio and J_L the load (i.e. compressor-expander) inertia. And if the load presents a torque T_L^*, it will affect the load torque in equation 3.62 by $T_L = T_L^* / N$. The performance map for the DC motor is shown in Figure 3.15.

3.4.4 Modeling of the Pressure Control Servovalve

The pressure control servovalve (e.g., for compressor back pressure control) model is taken from Technical Bulletin 103 of MOOG INC (1965) published by their Controls Division. They presented simplified, equivalent transfer function of electrohydraulic servovalevs for the purpose of servoanalysis and system synthesis based on experimental results. The pressure control servovalve provides a differential pressure output in response to the electrical input current. The transfer function of the servovalve is

$$\frac{P}{i}(s) = K_1 \left[1 + \left(\frac{2\zeta}{\omega_n} \right) s + \left(\frac{s}{\omega_n} \right)^2 \right]^{-1} \tag{3.66}$$

where s represents the frequency domain (this is the transfer function of the servovalve), P is the output pressure, and i the input current to the servovalve. K_1, ω_n, and ζ are constant and represent the characteristics of a servovalve. In equation 3.58, K_1 is the gain of the servovavle (125 psi/ma), ω_n the natural frequency (250 rad/sec), and ζ the damping ratio (0.4).

3.5 Cost Models of the SS, FPS and WRAS

In this section, cost models of the fuel cell system purchase, installation, maintenance, and operation are introduced (developed in Kim, 2008).

The FPS purchase cost is given in Table 3.10. The cost functions of the SMR, HTSR, and LTSR are obtained from Georgopoulos (2002), with modifications of the catalyst costs to reflect current market prices (provided by Johnson Matthey Catalysts). The purchase cost of the PrOx is obtained from Kamarudin el al. (2006). The steam generator cost model from Rancruel (2005) has been modified based on the current cost information provided by Baratto et al. (2005). Cost model from Haslego and Polley

(2002) is applied for the compact heat exchanger cost function with correction of the market price (from Des Champs Technologies).

Table 3.10 Baseline purchase cost of the FPS (Kim 2008).

Variable Description		Model Equation
C_1^{FPS}	Bare reactor purchase cost for the SMR, HTSR, and LTSR	$C_1^{FPS} = 4990\left(V_{SMR} + V_{HSR} + V_{LSR}\right)^{0.4}$
V_i	Volume of a reactor i	
C_2^{FPS}	Catalyst purchase cost for the SMR, HTSR, and LTSR	$C_2^{FPS} = 33548.9V_{C,SMR} + 15467.8V_{C,HSR} + 24296.5V_{C,LSR}$
$V_{C,i}$	Volume of catalyst in a reactor i	
C_3^{FPS}	PrOx reactor purchase cost	$C_3^{FPS} = 1.6 \times 10^5 V_{\mathrm{Pr}Ox}$
C_4^{FPS}	Total heat exchangers purchase cost	$C_4^{FPS} = \sum_{j=1}^{n}\left(125.5 A_{HX,j}{}^{0.4887}\right)$
$A_{HX,j}$	Plate surface area of a heat exchanger j	
n	The number of heat exchanger	
C_5^{FPS}	Steam generator purchase cost	$C_5^{FPS} = 96.2 A_{SG}{}^{0.7}$
A_{SG}	Steam generator heat transfer area	
C_6^{FPS}	Purchase cost of major parts	$C_6^{FPS} = \sum_{k=1}^{5} C_k^{FPS}$
C_7^{FPS}	Auxiliary parts cost (pipe, controller, pumps, valves, mixing chambers, etc)	$C_7^{FPS} = 0.2 C_6^{FPS}$
C_8^{FPS}	Baseline purchase cost of the FPS	$C_8^{FPS} = C_6^{FPS} + C_7^{FPS}$

For the cost of the auxiliary components in the FPS (e.g., pipe line, controller, valves, mixing chambers, combustor, water pumps, etc.), prices are much cheaper than the reactors. They affect only a little to the system synthesis/design and operation/control optimization. Their costs are considered as 20% of purchase cost of the major components (Baratto et al., 2005).

Based on the baseline purchase cost of the FPS, a single unit purchase cost of the FPS has been calculated and the life cycle cost of the FPS has been addressed in terms of the single unit purchase cost as shown in Table 3.11. And, the installation cost of the FPS is assumed to be 20% of the FPS purchase cost, and 10.1% of the FPS purchase cost is considered as the indirect cost (Baratto el at., 2005). The life cycle cost of the FPS can be expressed as sum of the purchase cost, installation cost, maintenance cost, amortization

cost, and indirect cost as seen in Table 3.11.

The FPS operating cost associating with fuel consumption is given by

$$C_{operation}^{FPS} = C_{NG} \cdot \int_{t=0}^{oneyear} \dot{n}_{NG} dt \tag{3.67}$$

where C_{NG} is the natural gas price and $\dot{n}_{NG}$ is the consumption rate of natural gas during operating. Natural gas price is obtained from Energy Information Administration, and average price for residential in 2006, 13.75 \$/kft^3, has been used for calculating the operating cost.

Table 3.11 Capital cost estimation of the FPS (annual based).

Variable Description		Model Equation
f_{cap}	Capitalization factor	$f_{cap} = \frac{I_{amor}\left(1+I_{amor}\right)^{N_{year}}}{\left(1+I_{amor}\right)^{N_{year}}-1}$
$C_{purchase}^{FPS}$	Purchase cost of the FPS	$C_{purchase}^{FPS} = C_8^{FPS}\left(\frac{N_{units}}{500000}\right)^{-0.362}$
$C_{install}^{FPS}$	Installation cost of the FPS	$C_{install}^{FPS} = 0.2C_{purchase}^{FPS}$
$C_{indirect}^{FPS}$	Indirect cost of the FPS	$C_{indirect}^{FPS} = 0.101C_{purchase}^{FPS}$
C_{main}^{FPS}	Maintenance cost of the FPS	$C_{main}^{FPS} = f_{main}\left(C_{indirect}^{FPS} + C_{purchase}^{FPS}\right)$
C_{amor}^{FPS}	Amortization cost of the FPS	$C_{amor}^{FPS} = f_{cap}\left(C_{indirect}^{FPS} + C_{install}^{FPS} + C_{purchase}^{FPS}\right)$
$C_{Capital}^{FPS}$	Annual capital cost of the FPS	$C_{Capital}^{FPS} = C_{main}^{FPS} + C_{amor}^{FPS}$

Table 3.12 Baseline purchase cost of the WRAS (Kim, 2008).

Variable Description		Model Equation
C_1^{WRAS}	Compressor purchase cost	$C_1^{WRAS} = 256\dot{W}_1^{WRAS}$
$\dot{W}_1^{WRAS}$	Compressor work at design	
C_2^{WRAS}	Expander purchase cost	$C_2^{WRAS} = 256\dot{W}_2^{WRAS}$
$\dot{W}_2^{WRAS}$	Expander work at design	
C_3^{WRAS}	DC motor purchase cost	$C_{motor}^{WRAS} = 0.2C_{comp}^{WRAS}$
C_4^{WRAS}	Baseline purchase cost of the WRAS	$C_4^{WRAS} = \sum_{i=1}^{3} C_i^{WRAS}$

In the same manner as the cost model development for the FPS, purchase cost models for the WRAS were established and the life cycle cost of the WRAS has been evaluated. Compressor and expander purchase cost models are adopted from Baratto et al. (2005), and DC motor purchase cost is assumed at 20 % of the compressor purchase cost based on Carlson et al.'s (2005) report. Table 3.12 and Table 3.13 shows baseline purchase cost and life cycle cost estimation of the WRAS, respectively.

Table 3.13 Capital cost estimation of the WRAS (annual based).

Variable Description		Model Equation
$C_{purchase}^{WRAS}$	Purchase cost of the WRAS	$C_{purchase}^{WRAS} = C_4^{WRAS}\left(\frac{N_{units}}{500000}\right)^{-0.362}$
$C_{install}^{WRAS}$	Installation cost of the WRAS	$C_{install}^{WRAS} = 0.2C_{purchase}^{WRAS}$
$C_{indirect}^{WRAS}$	Indirect cost of the WRAS	$C_{indirect}^{WRAS} = 0.101C_{purchase}^{WRAS}$
C_{main}^{WRAS}	Maintenance cost of the WRAS	$C_{main}^{WRAS} = f_{main}\left(C_{indirect}^{WRAS} + C_{purchase}^{WRAS}\right)$
C_{amor}^{WRAS}	Amortization cost of the WRAS	$C_{amor}^{WRAS} = f_{cap}\left(C_{indirect}^{WRAS} + C_{install}^{WRAS} + C_{purchase}^{WRAS}\right)$
$C_{Capital}^{WRAS}$	Annual capital cost of the WRAS	$C_{Capital}^{WRAS} = C_{main}^{WRAS} + C_{amor}^{WRAS}$

Table 3.14 Baseline purchase cost of the SS (Kim, 2008).

Variable Description		Model Equation
C_1^{SS}	Membrane cost	$C_1^{SS} = (0.00229256A_{act} + 0.0182)N_{cell}$
C_2^{SS}	Bipolar plate cost	$C_2^{SS} = (0.00111671A_{act} + 0.2485)N_{cell}$
C_3^{SS}	Electrode cost	$C_3^{SS} = 0.029742A_{act}N_{cell}$
C_4^{SS}	Assembly cost	$C_4^{SS} = 24.98 + 0.28105N_{cell}$
C_5^{SS}	Stack purchase cost	$C_5^{SS} = \sum_{i=1}^{4} C_i^{SS}$
C_6^{SS}	Auxiliary parts cost (cooling cycle, humidifier, value, controller, etc)	$C_6^{SS} = 13/6\, C_5^{SS}$
C_7^{SS}	Baseline purchase cost of the SS	$C_7^{SS} = C_5^{SS} + C_6^{SS}$

The stack purchase cost is broken down into components purchase cost of the stack (i.e. purchases of the membrane, bipolar plates, and electrodes) and assembly cost based

on Oei at el. (1997). Their cost models have been modified to reflect current price by comparing to Carlson el al.'s (2005). As shown in Table 3.14, the stack price is composed of stack purchase cost and auxiliary parts purchase cost including a cooling cycle, a humidifier, valves, and controllers. Life cycle cost of the SS are summarized in Table 3.15 as same as that of the FPS and WRAS.

Table 3.15 Capital cost estimation of the SS (annual based).

Variable Description		Model Equation
$C_{purchase}^{SS}$	Purchase cost of the SS	$C_{purchase}^{SS} = C_7^{SS}\left(\frac{N_{units}}{500000}\right)^{-0.362}$
$C_{install}^{SS}$	Installation cost of the SS	$C_{install}^{SS} = 0.2C_{purchase}^{SS}$
$C_{indirect}^{SS}$	Indirect cost of the SS	$C_{indirect}^{SS} = 0.101C_{purchase}^{SS}$
C_{main}^{SS}	Maintenance cost of the SS	$C_{main}^{SS} = f_{main}\left(C_{indirect}^{SS} + C_{purchase}^{SS}\right)$
C_{amor}^{SS}	Amortization cost of the SS	$C_{amor}^{SS} = f_{cap}\left(C_{indirect}^{SS} + C_{install}^{SS} + C_{purchase}^{SS}\right)$
$C_{Capital}^{SS}$	Annual capital cost of the SS	$C_{Capital}^{SS} = C_{main}^{SS} + C_{amor}^{SS}$

Table 3.16 Economic assumptions for the life cycle cost analysis (Kim, 2008).

Parameter Description		Value
N_{units}	Production volume	500,000
h	Operating hour per year (hours)	7,920
N_{year}	Life time (years)	10
f_{main}	Maintenance factor per year	0.1 (10 %)
I_{amor}	Interest rate	0.05 (5 %)

For calculation of the life cycle cost of the FPS, SS, and WRAS, several economic assumptions are made as shown in Table 3.16. The cost information introduced in this model is based on 500,000 production volume per year (Arthur D. Little, 2001; Carlson at el., 2005; Baratto et al., 2005). And, generally, high production volume will produce low single unit cost. The effect of changing the production volume on a single unit cost is taken into account by applying an appropriate scale factor to the purchase cost. For the purpose of describing the effect, the single unit cost has been expressed given by

$$C_{unit} = C_{N_{base}} \left(\frac{N_{unit}}{N_{base}} \right)^{\alpha} \tag{3.68}$$

in which C_{unit} it the single unit cost based on the production volume N_{unit}, $C_{N_{base}}$ the baseline purchase cost based on the production volume N_{base} (e.g., 500,000). α is the scale factor, and it explains reduction rate of manufacturing cost for the production volume N_{unit}. Alonso (2001) suggested -0.362 on the basis of the 500,000 production volume. And this value is used for the scale factor in this analysis. Finally, the PEMFC system life cycle cost can be written as

$$C_{life} = \frac{1}{f_{cap}} \sum \left(C_{capital}^{FPS} + C_{capital}^{WRAS} + C_{capital}^{SS} + C_{operation}^{FPS} \right). \tag{3.69}$$

3.6 Dynamic Load Profile

In order to do the synthesis/design and operational/control optimization of the proposed fuel cell system, a dynamic load profile must be established, i.e. the energy requirements for a representative residential building (one house of a typical family). The types of residential loads considered are the following:

- Electrical load.
- Space heating load.
- Space cooling load.

The electrical load, in particular, includes the electricity needed to power the lights and appliances of the residence as well as the fans of the HVAC equipment. The profiles of these three different loads depend greatly on the geographical location of the residence and the corresponding weather conditions. The residential energy demands given in Figures 3.16 are representative of Southern California area during the summer and winter (Southern California Edison, 2006). For the purposes of this doctoral work, these demand curves have been simplified by Kim (2008) into a two-day load profile, i.e. a typical summer day plus a typical winter day. It is assumed that this sufficiently models the load changes for the synthesis/design process. The resulting 48-hour load profile shown in Figures 3.16 is multiply by 180 days in order to account for a whole year, i.e. the system

is synthesized/designed based on a load profile somewhat more constrained than what the actual yearly profile looks like.

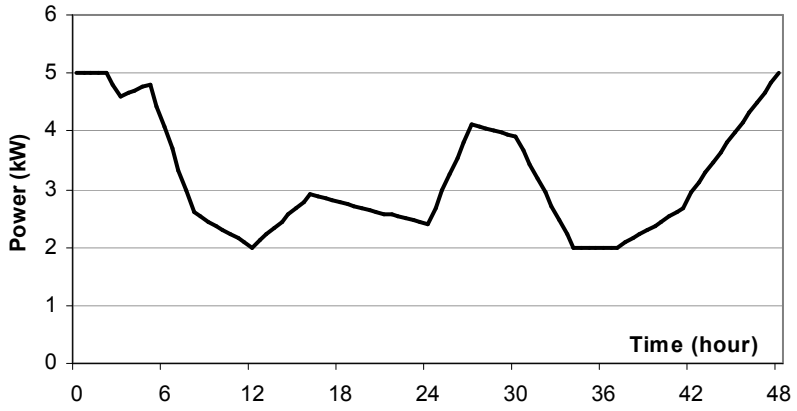

Figure 3.16 48-hour dynamic load profile used for the synthesis/design and operation/control optimization of the FCS (Kim, 2008).

Chapter 4

Control Architecture Design

To gain both in terms of energy savings and pollutant emissions from a fuel cell system, it is important that the fuel cell system not only be well synthesized and designed but also appropriately controlled to meet the varying loads and safety requirements for a given applications. In fuel cell systems, not only must the power be controlled intelligently but also the thermal and water management of the system. Therefore, proper design of the control architecture for the fuel cell system is crucial to the system performance and directly affects system synthesis/design. This chapter describes the basics of control theory and the control architecture considered during the PEMFC fuel cell system synthesis/design and operation/control optimization.

4.1 Feedback Control

A control system is a set of devices that allows the controlled system to generate desired responses. Feedback control is very common and important in both nature and engineering design.

Suppose that there is a process H which we wish to control. Call the input to the process u and the output from the process y, as shown in Figure 4.1.

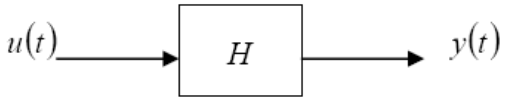

Figure 4.1 Open-loop control schematic.

Furthermore, assume that a complete description of the process is available so that it is known what the output y will be for any input. Thus, there is one particular input, u_1, which corresponds to a specified desired output, y_1. One way of controlling the process so

that it produces the desired output y_1 is to supply it with the input u_1. This is "open-loop control".

In contrast, the elements of a feedback control system are shown in Figure 4.2. Instead of controlling the output of the process by picking the control signal u which produces the desired y, the control signal u is generated as a function of the "system error" defined as the difference between the desired output r and the actual output y. This error is then amplified by the "amplifier" to generate the input u to the process.

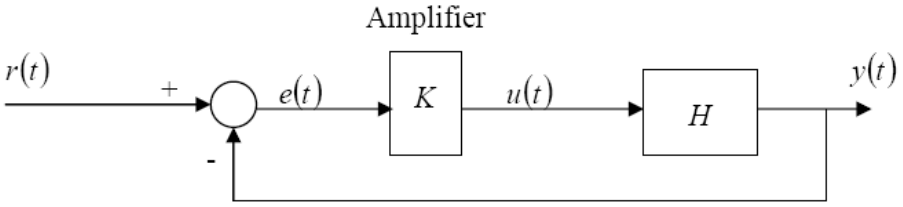

Figure 4.2 Feedback control schematic.

Suppose now that the operation of the process under control can be represented by a simple algebraic relation such as

$$y = Hu \tag{4.1}$$

and that the amplifier can similarly be described as

$$u = Ke \tag{4.2}$$

where e is the error equal to the difference between r and y. Combining these two equations result in,

$$y = \frac{HK}{1 + HK} r \tag{4.3}$$

Although the output y is not exactly equal to the desired output r, if the amplifier "gain" K is large enough, thus the actual output y can be made approach the desired output as closely as desired simply be making the gain K large enough. Moreover, this result holds, for any desired output. In fact, the r does not have to be known which contrast with the open-loop control in which u must be known in advance. This result holds independent of the process, i.e. it does not matter what H is, which means that the system will still generate the desired output even if the system (or process H) has changes to it.

$$y \cong r \tag{4.4}$$

This simple example shows some advantages of feedback control. The problem, however, is that usually *y* can not be represented by an algebraic equation as simple as equation 4.1. Because of the process dynamics, the relationship between the output and the input is much more complex, and the control architecture design is much more complex as well.

4.2 Classical Control Architecture Design

The use of transfer-function-based methods such as root locus and frequency response to design the control architecture is referred to as classical control design. The fundamental concept of classical control design analysis is the "transfer function" which expresses the relationship between the Laplace transform *Y(s)* of the system output *y(t)* and the Laplace transform *U(s)* of the input *u(t)*

$$Y(s) = H(s)U(s), \tag{4.5}$$

where *H(s)* is the transfer function of the system, *s* the Laplace operator, and *t* the time. The Laplace transform for a function of time, *f(t)*, is

$$F(s) = \int_0^\infty f(t) \cdot e^{-st} dt = L\{f(t)\} \tag{4.6}$$

To illustrate the usefulness of the Laplace transform and the steps involved in the system analysis, consider a typical second order system/process (because second order system can approximate higher order systems in system control) defined in time domain by

$$M\frac{d^2y(t)}{dt^2} + a\frac{dy(t)}{dt} + by(t) = u(t). \tag{4.7}$$

which physically can be considered as a spring-mass-damper system (with mass *M*, $M\frac{d^2y}{dt^2}$ represents the acceleration force, $a\frac{dy}{dt}$ the friction/damper force, by the spring force, and $u(t)$ the input force). In the equation, *M*, *a*, and *b* are constants and *y(t)* and *u(t)* the output and input, respectively, of the process. It is desired to obtain the response, *y*, of the process as a function of time, which is usually difficult for higher order system (equal or higher than second order). With Laplace transform, a nonlinear (high order)

system can be represented by linear equation in the frequency domain, which will give very important insight for system design and dynamic control.

The Laplace of a k^{th} order derivative term $f^{(k)}(t)=\frac{d^k f(t)}{dt^k}$ is

$$s^k F(s)-s^{k-1}f(0^-)-s^{k-2}f'(0^-)-\ldots-f^{(k-1)}(0^-). \tag{4.8}$$

Based on equation 4.8, the Laplace transform for the second order system (equation 4.7) is

$$M\left(s^2Y(s)-sy(0^-)-\frac{dy(0^-)}{dt}\right)+a\left(sY(s)-y(0^-)\right)+bY(s)=U(s) \tag{4.9}$$

where $Y(s)$ is the Laplace transform of $y(t)$, $y(0^-)$ the initial condition of $y(t)$, and $U(s)$ the Laplace transform of $u(t)$. We want to get the response, y, as a function of time. Once the initial conditions are know, such as

$$u(t)=0 \qquad y(0^-)=y_0 \qquad \left.\frac{dy}{dt}\right|_{t=0^-}=0 \tag{4.10}$$

which mean that the initial condition on $y(t)$ and its derivative and the input are zeros, equation 4.9 is solved for $Y(s)$ such that

$$Y(s)=\frac{(Ms+a)y_0}{Ms^2+as+b}=\frac{p(s)}{q(s)}. \tag{4.11}$$

which can be transferred to the solution in time domain, $y(t)$, with inverse Laplace transform. The polynomial *q(s)* in the denominator set equal to zero is called the characteristic equation. The roots of this characteristic equation are called the poles of the system. The roots of the polynomial *p(s)* in the numerator set equal to zero are called the zeros of the system. The complex frequency s-plane plot of the poles and zeros graphically can portray the character of the natural transient response of the system without solving for $y(t)$ explicitly.

For the case with nonzero input, $u(t)$, and when the initial condition on $y(t)$ and its derivative are zeros

$$y(0^-)=y_0 \qquad \left.\frac{dy}{dt}\right|_{t=0^-}=0 \tag{4.12}$$

the transfer function (Laplace transform) of the second order system above (4.9) is found from

$$Ms^2Y(s)+asY(s)+bY(s)=U(s) \tag{4.13}$$

And it is,

$$G(s)=\frac{Y(s)}{U(s)}=\frac{1}{Ms^2+as+b}. \tag{4.14}$$

which here represents the ratio between the output and input in the frequency domain. A block diagram of this second order system is shown in Figure 4.3 and can be related directly back to open-loop control system of Figure 4.1 but in this case is the frequency domain representation.

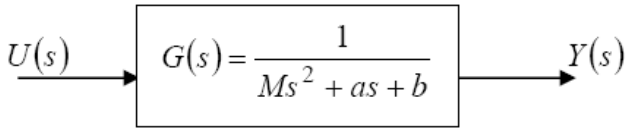

Figure 4.3 Block diagram of the second order system in the frequency domain representation.

Proportional feedback

When the open-loop system of Figure 4.3 is transformed into a closed-loop feedback control system (see Figure 4.4) with M=1, the feedback control signal can be made to be linearly proportional to the error in the measured output. This type of feedback is called proportional. The general form of proportional control is given by

$$u(t)=Ke(t) \tag{4.15a}$$

or in the frequency domain by

$$U(s)=KE(s). \tag{4.15b}$$

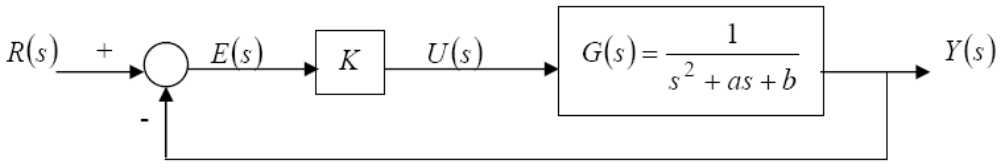

Figure 4.4 Block diagram of the closed-loop feedback control system (corresponding to Figure 4.3).

For the second-order linear process of Figure 4.4, i.e. for

$$G(s)=\frac{1}{s^2+as+b} \tag{4.16}$$

a new transfer function $G'(s)$ is found using equation 4.3 which relates the actual output to the desired output, i.e.

$$G'(s) = \frac{KG(s)}{1 + KG(s)} \tag{4.17}$$

Dividing the numerator and denominator by $G(s)$ results in

$$G'(s) = \frac{K}{1/G(s) + K} = \frac{K}{s^2 + as + b + K} \tag{4.18}$$

Thus, for the proportional feedback, the closed-loop characteristic equation is

$$s^2 + as + b + K = 0 \tag{4.19}$$

By analyzing the root locus (the locations of the roots of the characteristic equation in the complex frequency s-plane) for different values of K, a number of conclusions can be drawn with regards to proportional control: i) for higher-order systems (i.e. for higher order polynomial characteristic equations), very large values of the proportional feedback gain can often lead to instability (the poles of the closed-loop system will be on the far left of the s-plane which may not be able to dominant the system dynamics), ii) proportional feedback increases the speed of driving the error to zero, and iii) in some cases proportional feedback is essential for eliminating the error.

Integral feedback

Integral feedback takes the form

$$u(t) = \frac{K}{T_I} \int_{t_0}^{t} e dt \tag{4.20}$$

where $\frac{K}{T_I}$ is the integral gain (this is a convenience way for writing together with the proportional feedback, i.e. $u(t) = K\left(e(t) + \frac{1}{T_I} \int_{t_0}^{t} e(t) dt \right)$). The transformation of equation 4.20 into the frequency domain results in

$$U(s) = \frac{K}{T_I s} E(s) \tag{4.21}$$

The primary reason for integral control is to reduce or eliminate steady-state errors, but this benefit typically comes at the cost of reduced stability. In general, any system will be made less stable or less damped by the addition of integral control.

Derivative feedback

Derivative feedback takes the form

$$u(t) = KT_D\dot{e} \tag{4.22}$$

where KT_D is the derivative gain and $\dot{e}$ represents the time derivative of e. The transformation of equation 4.22 into the frequency-domain yields

$$U(s) = KT_D sE(s) \tag{4.23}$$

This type of feedback is typically used in conjunction with proportional and/or integral feedback to increase the damping which generally improves the stability of the controlled system. Unless the system has a natural proportional term or equivalent feature, derivative feedback by itself will not drive the error to zero. The derivative feedback affects the rate at which initial time derivative values of y decay to zero.

PID controllers

Feedback which has the three types of feedback described above, i.e. proportional, integral, and derivative, is referred to as PID control. The controller transfer function is given by

$$U(s) = K\left(1 + \frac{1}{T_I s} + T_D s\right)E(s). \tag{4.24}$$

The PID combination is sometimes able to provide an acceptable degree of error reduction simultaneously with acceptable levels of stability and damping. In general, increasing K and $1/T_I$ tend to reduce system errors but may not be capable of also producing adequate stability. Increasing T_D tends to improve stability.

4.3 State Space Control Design

The goal of classical control design is to find a compensation (which is the alteration or adjustment of a control system in order to provide a suitable performance) that best satisfy the design specifications. The goal of the state space design technique is exactly the same. Because the method of describing the plant and the compensation is so different between these two methods, it may seem that an entirely different problem is

being solved. In the state space method, dynamic systems are described by a set of first-order linear ordinary differential equations in variables called the state.

4.3.1 State Variable Representation of System

This section introduces how to represent a dynamic system with state space. Assume that there is a system which can be represented by the two second-order linear ordinary differential equations

$$\alpha \cdot \ddot{\omega}(t) + \beta \cdot \ddot{\theta}(t) - u(t) = 0 \tag{4.25}$$

$$\nu \cdot \ddot{\omega}(t) + \delta \cdot \ddot{\theta}(t) - \xi \cdot \theta(t) = 0 \tag{4.26}$$

where *u(t)* is the input to the system, $\omega(t)$ and $\theta(t)$ the two unknowns (can be solved based on these two system equations), and α, β, ν, δ, ξ constants. For the purpose of studying state space control design using this system, one of the unknowns, $\theta(t)$, is selected to be the output of the system (we want the $\theta(t)$ to be able to tracking the desire value), with $\omega(t)$ will not be controlled.

The state variables for these two second-order linear ordinary differential questions are chosen as $(x_1, x_2, x_3, x_4) = (\omega, \dot{\omega}, \theta, \dot{\theta})$. Equations (4.25) and (4.26) can then be written in terms of the state variables as

$$\alpha \cdot \dot{x}_2 + \beta \cdot \dot{x}_4 - u(t) = 0 \tag{4.27}$$

and $$\nu \cdot \dot{x}_2 + \delta \cdot \dot{x}_4 - \xi \cdot x_3 = 0 \tag{4.28}$$

To obtain the necessary first-order differential equations (there should be only one derivative term in each equation), these two equations are solved for $\dot{x}_2$ and $\dot{x}_4$ resulting in four first-order linear ordinary differential equations, i.e.

$$\dot{x}_1 = x_2 \tag{4.29}$$

$$\dot{x}_2 = \frac{\beta\xi}{\beta\nu - \alpha\delta} x_3 + \frac{\delta}{\alpha\delta - \beta\nu} u(t) \tag{4.30}$$

$$\dot{x}_3 = x_4 \tag{4.31}$$

$$\dot{x}_4 = \frac{\alpha\xi}{\alpha\delta - \beta\nu} x_3 + \frac{\nu}{\beta\nu - \alpha\delta} u(t) \tag{4.32}$$

In matrix form, these equations (with $\vec{x} = (x_1, x_2, x_3, x_4)^T$) are written as

$$\dot{\vec{x}} = A\vec{x} + Bu(t) \tag{4.33}$$

where $\vec{x}$ is a vector, $u(t)$ the input (scalar), with

$$A = \begin{bmatrix} 0 & 1 & 0 & 0 \\ 0 & 0 & \dfrac{\beta\xi}{\beta\nu - \alpha\delta} & 0 \\ 0 & 0 & 0 & 1 \\ 0 & 0 & \dfrac{\alpha\xi}{\alpha\delta - \beta\nu} & 0 \end{bmatrix} \tag{4.34}$$

$$B = \begin{bmatrix} 0 \\ \dfrac{\delta}{\alpha\delta - \beta\nu} \\ 0 \\ \dfrac{\nu}{\beta\nu - \alpha\delta} \end{bmatrix} \tag{4.35}$$

Usually, $y(t)$ is used to represent a system output (thus, in this case, $y(t) = \theta(t)$), and

$$y = C \cdot \vec{x} \tag{4.36}$$

$$\text{where } C = \begin{bmatrix} 0 & 0 & 1 & 0 \end{bmatrix} \tag{4.37}$$

Equations (4.33) to (4.37) are the state space representation of this dynamic system.

4.3.2 Design of Full-State Feedback Control Law and Observer

By transferring Equation (4.33) into frequency-domain (as shown in Equation (4.8) and (4.9)), it becomes

$$s\vec{X}(s) = A\vec{X}(s) + BU(s) \tag{4.38}$$

Thus, the relation between $\vec{X}(s)$ and $U(s)$ is

$$(sI - A)\vec{X}(s) = BU(s) \tag{4.39}$$

will I is a identity matrix. Substitute (4.39) into the Laplace transform of Equation (4.36) ($Y(s) = C\vec{X}(s)$), it shows

$$Y(s) = C(sI - A)^{-1} BU(s) \tag{4.40}$$

and the transfer function is

$$\frac{Y(s)}{U(s)} = C(sI - A)^{-1} B \tag{4.41}$$

By setting the characteristic equation (denominator of the transfer function) equal to zero, $\det(sI - A) = 0$, the pole locations of the open-loop system shown in Figure 4.5 can be determined by solving for s.

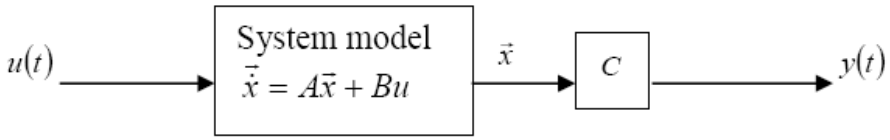

Figure 4.5 open loop system.

For the closed-loop control system, shown in Figure 4.6, with negative feedback gains $-\vec{K}$ (in this case, the size of $\vec{K}$ is 2×1 and $\vec{x}$ 1×2), the relation between $\vec{X}(s)$ and $U(s)$ in the frequency domain is

$$\left(sI - \left(A - B\vec{K}\right)\right)\vec{X}(s) = BU(s) \tag{4.42}$$

with $-\vec{K}\vec{X}(s)$ to be an input to the system and be multiplied by matrix B. Following the same procedure as Equation (4.40) and (4.41), the characteristic equation for this closed-loop system is

$$\det\left(sI - \left(A - B\vec{K}\right)\right) = 0 \tag{4.43}$$

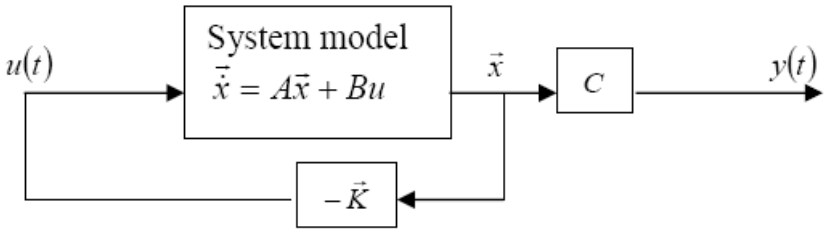

Figure 4.6 closed loop system.

With the characteristic equation of the closed-loop shown in Equation (4.43) and the locations of the desired poles (which should be the solution of the characteristic equation), the feedback control gains $\vec{K}$ can be calculated. Suppose the desired pole locations are at $-\phi \pm i\psi$ (i represents the imaginary part of the value) for the closed-loop system. Thus, we have

$$\left(s - \left(-\phi + i\psi\right)\right)\left(s - \left(-\phi - i\psi\right)\right) = \det\left(\lambda I - \left(A - B\vec{K}\right)\right) \tag{4.44}$$

from which the feedback gain matrix can be calculated by comparing the coefficients of the same order term from both sides of the equation. The procedure introduced above allows us to calculate the feedback control gains based on our desired pole locations.

The control law developed above assumes that all the state variables are available for feedback. In most systems, the state variables cannot all be measured for a number of reasons such as temperature too high, devices too expensive, etc. In such instances, observers/estimators are utilized in the system. The observer needs to provide an estimate of the states that cannot be directly observed. The goal is to achieve an accurate estimate as fast as possible without resulting in too large a gain matrix $\vec{L}$. The architecture with both observer and control law is shown in Figure 4.7.

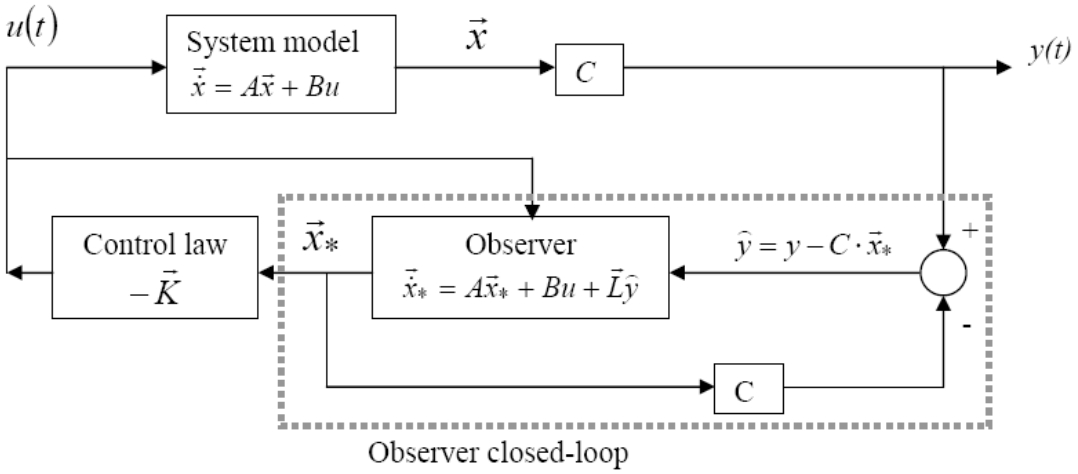

Figure 4.7 Estimator and controller mechanization.

In Figure 4.7, $\vec{x}_*$ represents the estimated states of $\vec{x}$. The matrix *A*, *B* and *C* in the observer are the same as in the system model. A good observer, which can support excellent estimation results of $\vec{x}$, can be obtained by intelligently design of the matrix *L*.

For a closed-loop system (Figure 4.6), the characteristic equation is shown in Equation 4.43. Therefore, for the closed-loop of the observer (shown as dash line in Figure 4.7), the characteristic equation for the observer is

$$\det\left(sI - \left(A - \vec{L}C\right)\right) = 0 \tag{4.45}$$

Suppose the desired observer pole locations are at $-3\phi \pm i\psi$ for this closed-loop observer (*i* represents the imaginary part of the value, and usually, for design purposes, an attempt is made to insure a separation of the desired closed-loop system poles, $-\phi \pm i\psi$, and the observer poles on the order of 2 to 10), where the constants ϕ and ψ can be appropriately chosen based on the settling time and the overshoot of the

observer. Next, the observer gain that achieves the desired observer pole locations can be found by solving

$$\left(s-\left(-3\phi+i\psi\right)\right)\left(s-\left(-3\phi-i\psi\right)\right)=\det\left(sI-\left(A-\vec{L}C\right)\right) \tag{4.46}$$

4.3.3 State Space Control Design on Dynamic Tracking

Last section discussed the basic of how to design full-state feedback control law and observer. Furthermore, if there is an extra integrator in the control system, as shown in Figure 4.8, it can remove the steady-state error to an input (Franklin, 1991), that is, command tracking (the output *y(t)* will track the input *r(t)* at any instance of time), which is the major goal of the control design used in this doctoral work. We can model the integrator by adding an extra state, which is the integral of the error, into the state space representation of the system.

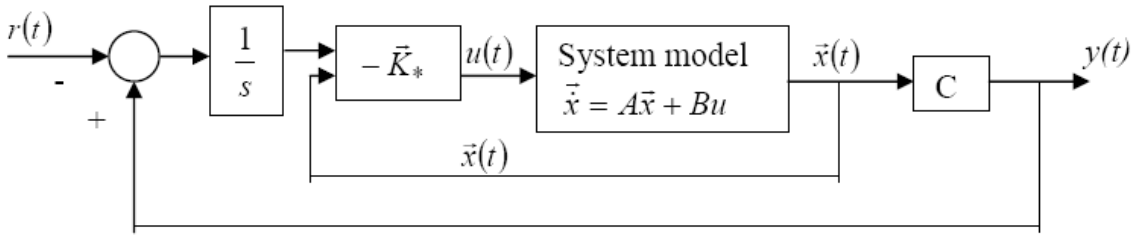

Figure 4.8 Control structure with an integrator.

Figure 4.8 presents a feedback control system without an observer (to simplify the problem, just assume all the state variables can be obtained without estimate). The new control matrix is $\vec{K}_*$. (Typically, in drawing of control block, $1/s$ is used to represent integration process even the whole block is presented in time domain, and $1/s$ in frequency-domain is the same as integration in time-domain). Therefore, the input of the system now is

$$u(t)=\vec{K}_*\begin{pmatrix}\int_{t_0}^{t}\left(y(t)-r(t)\right)dt\\ \vec{x}(t)\end{pmatrix} \tag{4.47}$$

As introduced in section 4.3.2, as long as the state space representation of a system is obtained, the controller gains can be calculated from the characteristic equation based on

the desired pole locations. Therefore, the problem now lays in what is the state space representation of the system with extra integrals in this dynamic tracking problem.

The same example will be used to illustrate the details of dynamic tracking control design. For the example from Section 4.3.1, the set of dynamic equations in state space given by Equations (4.33) to (4.37) is written as:

$$\frac{d}{dt}\begin{pmatrix} x_1 \\ x_2 \\ x_3 \\ x_4 \end{pmatrix} = \begin{bmatrix} 0 & 1 & 0 & 0 \\ 0 & 0 & \dfrac{\beta\xi}{\beta\nu - \alpha\delta} & 0 \\ 0 & 0 & 0 & 1 \\ 0 & 0 & \dfrac{\alpha\xi}{\alpha\delta - \beta\nu} & 0 \end{bmatrix} \begin{pmatrix} x_1 \\ x_2 \\ x_3 \\ x_4 \end{pmatrix} + \begin{bmatrix} 0 \\ \dfrac{\delta}{\alpha\delta - \beta\nu} \\ 0 \\ \dfrac{\nu}{\beta\nu - \alpha\delta} \end{bmatrix} u(t) \tag{4.48}$$

$$y = \begin{pmatrix} 0 & 0 & 1 & 0 \end{pmatrix} \begin{pmatrix} x_1 \\ x_2 \\ x_3 \\ x_4 \end{pmatrix} \tag{4.49}$$

where $y = x_3 = \theta$ is the output of the system and $u(t)$ the input which can be controlled. As noted above, an extra integrator in series with the plant can remove steady state error to an input, which states that the derivative of the integral of the output equals to the output. This equation will be placed at the top of the matrix. To accommodate this integrator and the closed-loop controller of Figure 4.8, the matrix equation for this controller is written as

$$\frac{d}{dt}\begin{pmatrix} \int x_3 \\ x_1 \\ x_2 \\ x_3 \\ x_4 \end{pmatrix} = \begin{bmatrix} 0 & 0 & 0 & 1 & 0 \\ 0 & 0 & 1 & 0 & 0 \\ 0 & 0 & 0 & \dfrac{\beta\xi}{\beta\nu - \alpha\delta} & 0 \\ 0 & 0 & 0 & 0 & 1 \\ 0 & 0 & 0 & \dfrac{\alpha\xi}{\alpha\delta - \beta\nu} & 0 \end{bmatrix} \begin{pmatrix} \int x_3 \\ x_1 \\ x_2 \\ x_3 \\ x_4 \end{pmatrix} + \begin{pmatrix} 0 \\ 0 \\ \dfrac{\delta}{\alpha\delta - \beta\nu} \\ 0 \\ \dfrac{\nu}{\beta\nu - \alpha\delta} \end{pmatrix} u(t) + \begin{bmatrix} -1 \\ 0 \\ 0 \\ 0 \\ 0 \end{bmatrix} r(t) \tag{4.50}$$

$$y = \begin{pmatrix} 0 & 0 & 0 & 1 & 0 \end{pmatrix} \begin{pmatrix} \int x_3 \\ x_1 \\ x_2 \\ x_3 \\ x_4 \end{pmatrix}. \tag{4.51}$$

where the inputs of the system now are $r(t)$ (desired value of $y(t)$) which is in the first row of the matrix, and $u(t)$ in the last four rows. The matrices in Equation (4.50) and (4.51) are referred to as A_a, B_{au}, B_a, and C_a. The state vector of the augment system is represented as $\vec{x}_a$

$$A_a = \begin{bmatrix} 0 & 0 & 0 & 1 & 0 \\ 0 & 0 & 1 & 0 & 0 \\ 0 & 0 & 0 & \dfrac{\beta\xi}{\beta\nu - \alpha\delta} & 0 \\ 0 & 0 & 0 & 0 & 1 \\ 0 & 0 & 0 & \dfrac{\alpha\xi}{\alpha\delta - \beta\nu} & 0 \end{bmatrix} \tag{4.52}$$

$$B_{au} = \begin{bmatrix} 0 & 0 & \dfrac{\delta}{\alpha\delta - \beta\nu} & 0 & \dfrac{\nu}{\beta\nu - \alpha\delta} \end{bmatrix}^T \tag{4.53}$$

$$B_a = \begin{bmatrix} -1 & 0 & 0 & 0 & 0 \end{bmatrix}^T \tag{4.54}$$

$$C_a = \begin{bmatrix} 0 & 0 & 0 & 1 & 0 \end{bmatrix} \tag{4.55}$$

$$\vec{x}_a = \begin{bmatrix} \int x_3 & x_1 & x_2 & x_3 & x_4 \end{bmatrix}^T \tag{4.56}$$

where A_a, B_{au}, and C_a are simply generated from A, B and C from Equation 4.33 to 4.37 with changes on the first row or column considering the extra state $\int x_3$, and B_a allows the reference input to affect the result. Note that the reference (desired output), $r(t)$, does not affect the states (except the integrator state) or the output of the plant because there is no path from the reference to the plant input, $u(t)$, without implementing the feedback matrix, $\vec{K}_*$.

After define the extra state variable and the new set of matrix to represent the system, the integral of the output will be fed back, and will be used by the controller to remove steady state error to a disturbance. With the values of these matrixes, 'place' function can be used to calculate the value of $\vec{K}_*$ for required locations of poles using Matlab.

4.4 Fuel Cell System Control

Overall fuel cell system performance and efficiency are critically dependent on the intelligent and optimal design of the control architecture. Control of the fuel cell system

includes that for heat and water management and that of the mass flow rates and pressures of both the fuel and air supply. This section describes the variety of control challenges encountered and the control strategies used for successful development of the PEMFC system's control architecture.

4.4.1 Stack Subsystem Control

In the dynamic fuel cell stack model, the three fundamental variables are voltage (V), current (I), and time. The voltage of the system can be measured or controlled as can the current, and both are a function of time. Furthermore, since current and voltage are intimately related via the fuel cell characteristics, they can not both be independently varied at the same time. If the voltage is controlled, then the fuel cell characteristics set the current. If instead the current is controlled, then these same characteristics set the voltage.

To get the fuel cell to operate at the desired power (or load) requirements, the power requirements must first be translated into current requirements based on the fuel cell characteristics shown in Figure 4.9. Even though there may be two different combinations of cell voltage and current density at one power density value, the fuel cell is always operated at the lower current density in the "operating region" shown in Figure 4.9. Of course, with different operating conditions (temperature, pressure, flow rate, etc.), the voltage - current density and power density - current density relations change. Nonetheless, these relations can be found from the model of the fuel cell stack. The fuel cell voltage is then controlled to allow the current to meet the dynamic current requirements. If a fuel cell stack (at its highest power density) can not satisfy the power requirements, the simulation is stopped and a bigger fuel cell stack is utilized in the model. Another desired output from the fuel cell stack is the fuel utilization (FU). With the cell current density value, the inlet hydrogen flow rate is controlled in order to ensure that the fuel cell stack meets the FU requirement.

The SS control architecture chosen here is shown in Figure 4.10. It is a feedback control with integrator for the purpose of dynamic tracking (as discussed in Figure 4.8). There are multi inputs (fuel cell stack voltage (V), inlet hydrogen flow rate ($\dot{m}_{H_2}$)) and outputs (fuel cell power, fuel utilization (FU)) in the system.

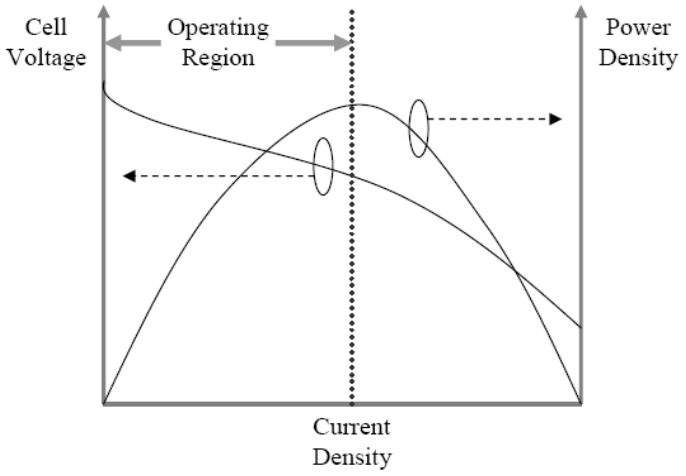

Figure 4.9 Relation between fuel cell current and power.

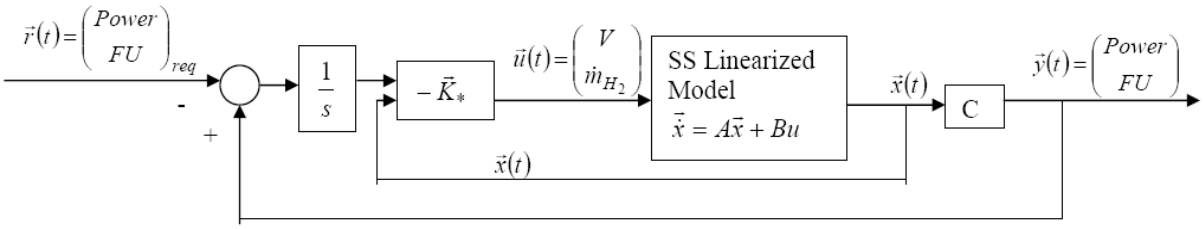

Figure 4.10 Stack subsystem control architecture.

For the control architecture design shown in Figure 4.10, the first step is to get the linearized SS model from this original non-linear SS. The non-linear SS model is programmed in gPROMS^{TM}, which has the capability of generating a linear representation (state space representation) of a non-linear model at a giving operating condition based on selected input and output variables. With the linearized model, the state space control design strategies introduced in previous sections can be applied to design the controller using Matlab. After the proper controller gains are determined, this control architecture will be programmed into the non-linear SS in gPROMS^{TM} to control the non-linear SS.

In this SS control design, cell voltage is controlled. Another variable which must be controlled is the fuel utilization of the stack, which is the percentage of the rate of hydrogen consumption in the stack over the inlet hydrogen flow rate. In this subsystem model, it is assumed that there is always a sufficient amount of hydrogen, which is supplied by the FPS, to be used by the stack. Thus, in addition to the flow rate controller needed to control the supply of fuel to the stack based on consumption, the controller must assure that the hydrogen supplied meets specific fuel utilization consistent with best

system performance and lowest cost. In Figure 4.10, the $\vec{R}$ vector represents the command inputs (i.e. desired outputs), which in this case are the power required and the fuel utilization desired. The $\vec{u}$ vector represents the inputs to the SS, which are the voltage and hydrogen flow rate. The $\vec{y}$ vector represents the actual output of SS, the power and fuel utilization while the $\vec{x}$ vector represents the state variables in the linearized SS model.

4.4.2 Work recovery and air-supply subsystem control

The WRAS provides air to the fuel cell system with required flow rate and pressure. Its control architecture is shown in Figure 4.11, which is similar to the SS control architecture in the Figure 4.10. The control design with Matlab is based on the linearized WRAS model. After that, the control architecture is programmed into the model in gPROMS™ for the non-linear WRAS control.

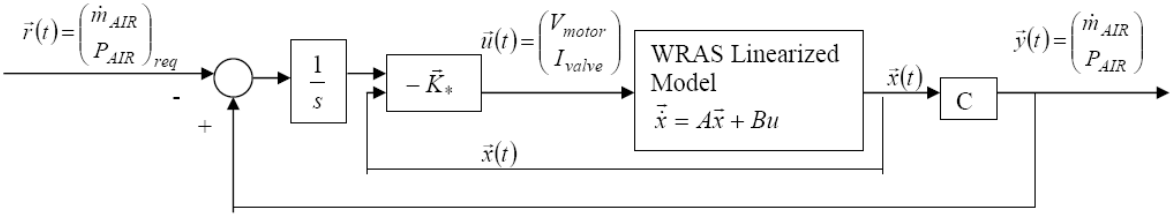

Figure 4.11 WRAS control architecture.

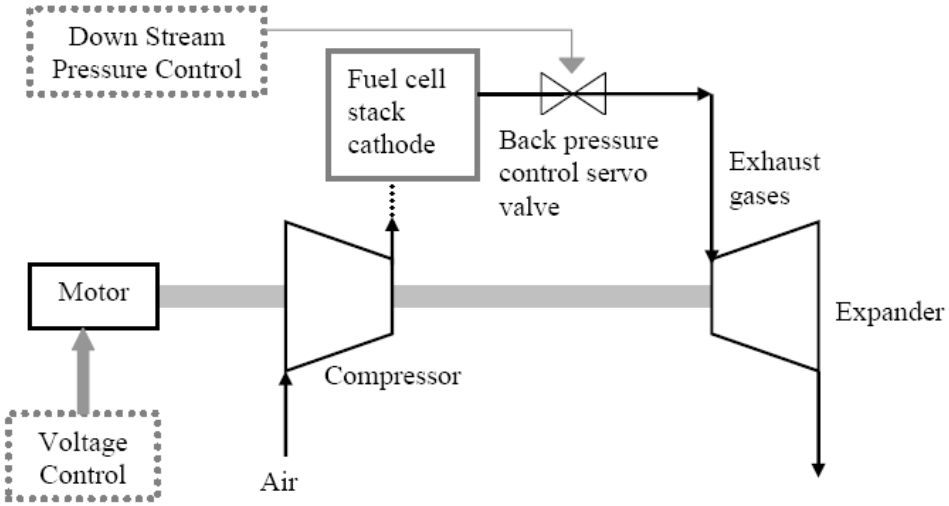

Figure 4.12 WRAS control schematic.

Figure 4.12 shows the WRAS control schematic. From the aspect of control design, there are two inputs to the WRAS: the voltage input to the motor (V_{motor}) and the current input to the down stream pressure controller (I_{valve}). There are also two outputs from the

WRAS, the air flow rate ($\dot{m}_{AIR}$) and the air pressure (P_{AIR}), which satisfy the fuel cell stack requirements. In the control structure, the voltage controls the motor shaft speed and, thus, the compressor shaft speed. The down stream pressure controller controls the air pressure in the fuel cell stack, which is related to the output air pressure from the compressor. Therefore, with the input and output pressure of the compressor determined, and with the shaft speed controlled, the air flow rate of the compressor is controlled.

4.4.3 Fuel processing subsystem control

There are several key inputs to the FPS, such as water flow rate, methane flow rate, cooling air flow rate, and exhausting fuel flow rate from the stack, etc. The control architecture of the FPS is shown in Figure 4.13.

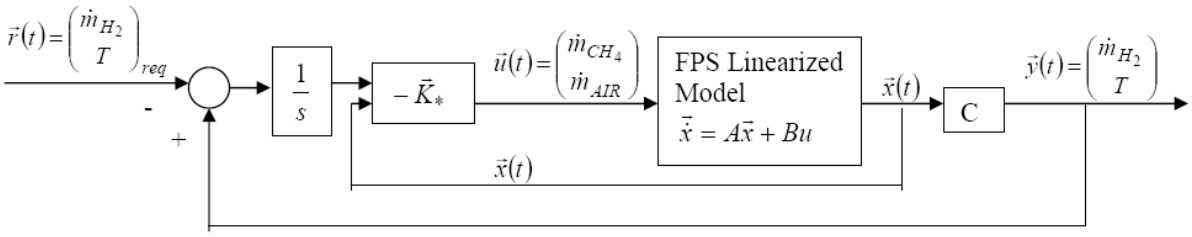

Figure 4.13 FPS control architecture.

Two variables are chosen to be controlled in this subsystem. To satisfy the hydrogen requirement from the stack, the methane flow rate is controlled since it affects the hydrogen generation rate. The ratio between the water flow rate and the methane flow rate is fixed in terms of model simulation even though it is a decision variable during the optimization. The water-methane ratio will affect the chemical kinetics in the reactors of FPS and thus, affect the hydrogen generation. The optimum ratio is determined during the optimization, while in the control architecture, this ratio is fixed. Therefore, one controller can control both the methane and water flow rates in the model simulation (to control the methane flow rate with fixed water-methane ratio).

The exhausting fuel from the stack is burned in the combustor of the FPS to generate heat for some of the reactors. This flow rate is not controlled due to: i) this exhausting gas is not enough for the combustor to meet the heat requirements; ii) methane is also input to the combustor and this flow rate is controlled. Therefore, the heat generation rate of the combustor is controlled by the methane flow rate, based on the heat requirement and the exhausting fuel flow rate from the stack. In the model simulation, the methane flow rate

ratio to the steam-methane reformer and to the combustor is fixed but becomes an operational decision variable during the optimization.

Another input which must be controlled is the cooling air flow rate which keeps the reactors at the appropriate temperatures. The flow rate ratios of cooling air among the different reactors and heat exchangers are fixed in the model simulation but become decision variables during the optimization.

4.4.4 PEMFC system control

Figure 4.14 depicts where and what is controlled in the fuel cell system. One MIMO controller is used to control the methane flow rate with fixed water – methane ratio and the cooling air flow rate to the FPS. Therefore, the hydrogen flow rate controller in the SS subsystem control is eliminated. The shaft speed of the compressor is controlled by the voltage input of the motor, together with the cathode air back pressure with another MIMO controller. The anode back pressure controller maintains the anode back pressure to be the same as the cathode. The fuel cell stack voltage is also controlled to meet the power (current) requirements.

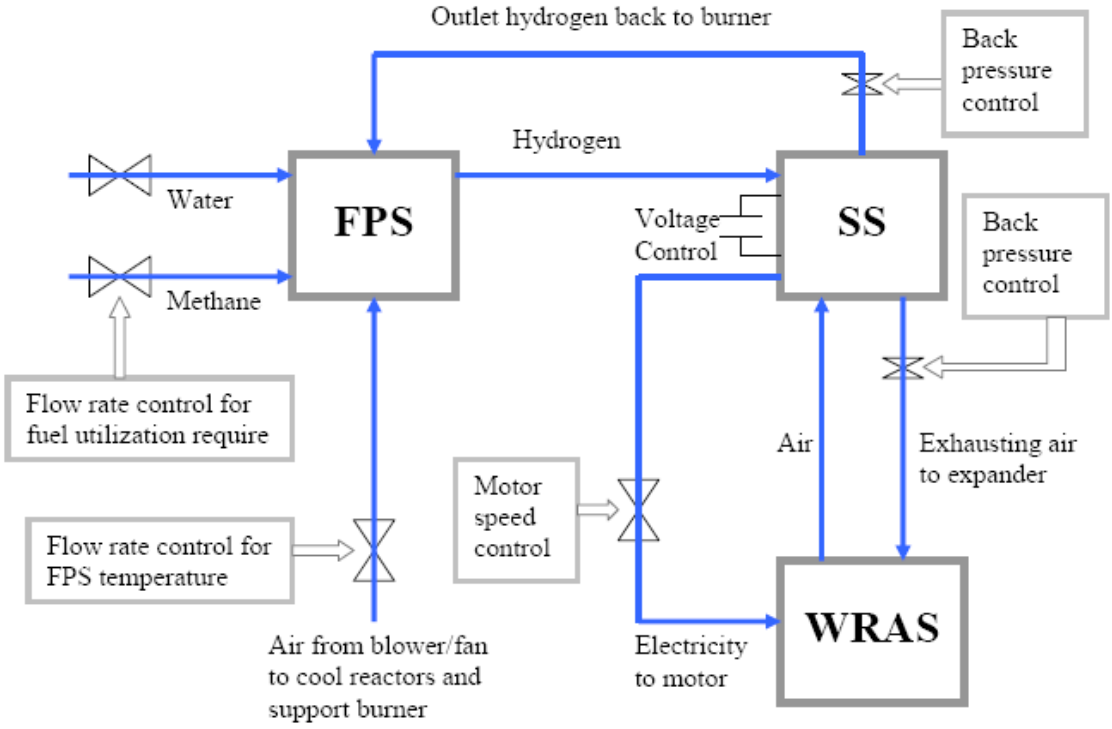

Figure 4.14 Overall schematic depicting where and what is controlled in the PEMFC system.

Chapter 5

Optimization Strategy

Optimization takes a very important role in system synthesis/design procedure. One of the original contributions of this doctoral work is to consider the system dynamics in the process of developing the system and studies different methods of synthesis/design and operation/control optimization of an energy system. Both the principles and details of the optimization approach utilized in this research will be introduced in this chapter.

As discussed in previous chapters, for a dynamic optimization, it is necessary to lay out the control architecture prior to the optimization so that the system can respond during the optimization process to the varying load. The optimal design of the control subsystem then becomes an important issue in the optimization along with that of the rest of the system (i.e. in this case the SS, FPS, and WRAS) process. The effects of the control on the optimization also need to be studied.

During the optimization, due to the large size of the optimization problems involved in complex energy system synthesis/design, and operation/control, various decomposition methods may need to be applied in order to make the optimization problem manageable or even possible. This chapter discusses the application of one type of decomposition strategy, namely, physical, that addresses the need for being able to do large-scale, non-linear optimization. Such physical decomposition is applied to the synthesis/design and operation/control optimization of a 5kW PEMFC system in this doctoral work. Three specific physical decomposition approaches are presented: Local-Global Optimization (LGO), Iterative Local-Global Optimization (ILGO), and Dynamic Iterative Local-Global Optimization (DILGO). The DILGO is based on ILGO and a definition of shadow prices which is capable of handling highly dynamic system optimizations. Furthermore, this chapter also introduces how to apply DILGO approach specifically to the system at hand.

For a deeper understanding of the concepts presented in this chapter, the reader is referred to the work by Muñoz and von Spakovsky (2000a,b,c,d; 2001a,b) and Rancruel and von Spakovsky (2003), and Rancruel (2005). The case is first made for the need of decomposition in the large-scale optimization of energy system synthesis/design. Indeed, the problem in its full complexity is defined as a dynamic, non-linear, mixed integer programming problem (DMINLP).

5.1 The Dynamic, Nonlinear Mixed Integer Programming Problem (DMINLP)

Generally, the synthesis/design and operation/control optimization of an energy system is a dynamic, nonlinear mixed integer programming problem (DMINLP) with equality and inequality constraints. In general terms, this is expressed as

Minimize $f(\vec{x},\vec{y})$ (5.1)

w.r.t $\vec{x},\vec{y}$

subject to $\vec{H}(\vec{x},\vec{y})=\vec{0}$ (5.2)

$\vec{G}(\vec{x},\vec{y})\le\vec{0}$ (5.3)

where $f(\vec{x},\vec{y})$ represents the objective of the optimization, the vector $\vec{x}$ the set of independent synthesis/design variables (such as length, size, etc.) of the system, and $\vec{y}$ the set of operational/control variables (such as pressures, flow rates, gains, etc.). The synthesis/design variables typically correspond to geometric parameters (physical dimensions of components), design flow rates, design pressure ratios, and in a wider sense a number of discrete (e.g., material or technology choices) or binary (e.g., the existence or nonexistence of units or connections in the system configuration) parameters. Operational/control variables can be continuous variables (flow rates, valve settings) or binary variables (e.g., units on or off). The vector of equality constraints, $\vec{H}(\vec{x},\vec{y})=\vec{0}$, represents the mass and energy balances (or other balances such as, for example, those for exergy, momentum, etc.) as well as the performance constraints that the energy system must obey. The vector of inequality constraints, $\vec{G}(\vec{x},\vec{y})\le\vec{0}$, represents physical or artificial limitations imposed upon the system.

The modeling of an energy system typically requires the selection of a number of degrees of freedom represented by parameters which can be varied at will within

acceptable limits. These independent parameters or variables are then used to create two systems of equations to represent the energy system, i.e. equations (5.2) and (5.3).

The DMINLP problem can be a highly complex problem which may not just be difficult to solve but may in fact be impossible to solve given the usual techniques of applied optimization. The complexity arises by virtue of the fact that a large number of degrees of freedom (both synthesis/design and operational variables) might be involved due to a desire to simultaneously optimize not only at a system level but at a detailed component/subsystem level. The complexity also arises because of the presense of detailed load profiles, highly non-linear models, and a mix of discrete and continuous variables. One option is to simplify the DMINLP problem greatly by, for example, reducing the number of independent variables, considering only a single instant in time (i.e. only part of the load profile), assuming only steady state operation and/or perhaps even linearizing certain or all aspects of the problem. The drawback, of course, to any of these measures is a loss of information, which may in fact not be necessary if the problem can be decomposed into a set of smaller problems, the solution to which closely approximates the solution to the combined problem. Physical decomposition is one such form of decomposition.

5.2 Physical Decomposition

Most energy systems can be decomposed into a set of units (subsystems and/or components), each of which has a clearly defined set of coupling functions with the other units of the system such as, for example, mass flow from one unit to another. Such a physical decomposition reduces the overall system optimization problem of synthesis/design and operation/control into a number of unit sub-problem optimizations. Three main approaches to physical (unit) decomposition are presented in the following sections. The first is the Local-Global Optimization (LGO) approach characteristic of most such approaches in the literature and the second is an original development by Muñoz and von Spakovsky (2000a,b,c,d; 2001a,b) called Iterative Local-Global Optimization (ILGO) approach. A third approach, developed by Rancruel and von Spakovsky (2005), is Dynamic Iterative Local-Global Optimization (DILGO).

Unit (physical) decomposition, as opposed to other decomposition strategies, such as time and conceptual decomposition (e.g., Frangopoulus, von Spakovsky, and Sciubba), tries to isolate the influence that each of the units that form a system has in terms of the overall (system-level) objective function. To illustrate the fundamentals of both LGO and ILGO, the simple two-unit system of Figure 5.1 is considered, where $\vec{z}_1$ and $\vec{z}_2$ are the decision variable sets for each unit, each unit is subject to a set of constraints which describe the physical processes present, and u_{12} and u_{21} are functions (in the general case, vectors of functions) that couple the two units. The overall system level objective function, C, is written as the sum of the contributions of each of the units, i.e. $C_1 + C_2$. In turn, the contribution of each unit is composed of two terms as, for example, indicated below for unit 1,

$$C_1 = C_{capital1} + k_1 R_1 \tag{5.4}$$

In equation (5.4), R_1 is some external resource consumed by unit 1 (typically fuel) and $C_{capital_1}$ is a function related to the size of the unit (weight/volume or cost) while k_1 is a conversion factor. In a thermoeconomic problem, $C_{capital_1}$ is the capital cost of unit 1. In a thermodynamic problem, $C_{capital_1}$ is either ignored, as may be the case for a stationary system, or translated into physical terms such as weight, as would be the case for a transportation system.

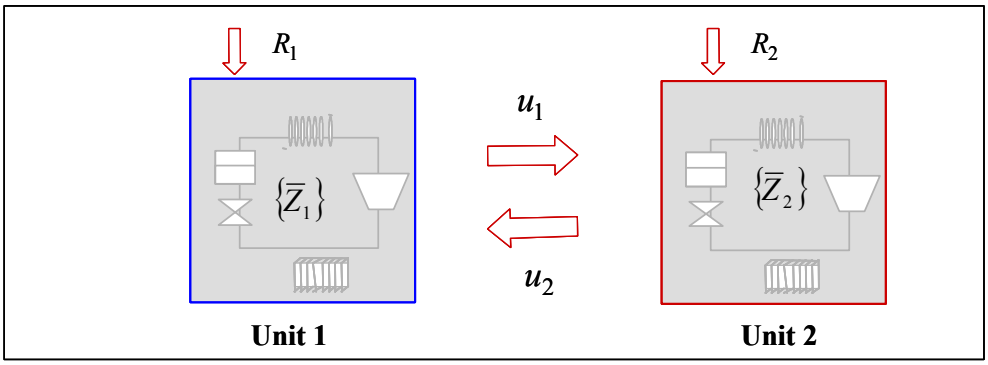

Figure 5.1 Physical decomposition of a 2-unit system (Rancrual, 2005).

5.3 The Local-Global Optimization (LGO) Approach

In the LGO approach, two levels of optimization instead of one are used. At the local or unit level, an optimization for each unit and each set of values of the coupling

functions between units is carried out. These optimum results are then used at a global or system level at which the system synthesis/design and operation/control is optimized with respect to the coupling function values. In order to get a better understanding of the LGO approach, consider the following optimization problem applied to a system decomposed into two units as shown in Figure 5.1.

$$\text{Minimize } C = k_1 R_1\left(\vec{z}_1, u_{12}(\vec{z}_1,\vec{z}_2), u_{21}(\vec{z}_1,\vec{z}_2)\right) + k_2 R_2\left(\vec{z}_2, u_{12}(\vec{z}_1,\vec{z}_2), u_{21}(\vec{z}_1,\vec{z}_2)\right) \tag{5.5}$$

w.r.t. $\vec{z}_1, \vec{z}_2$ and subject to the set of primary constraints

$$\vec{H} = \begin{bmatrix} \vec{h}_1 \\ \vec{h}_2 \end{bmatrix} = \vec{0} \tag{5.5.1}$$

$$\vec{G} = \begin{bmatrix} \vec{g}_1 \\ \vec{g}_2 \end{bmatrix} \le \vec{0} \tag{5.5.2}$$

and to the additional (secondary) constraints

$$u_{12}(\vec{z}_1,\vec{z}_2) - \xi = 0 \tag{5.5.3}$$

$$u_{21}(\vec{z}_1,\vec{z}_2) - \psi = 0 \tag{5.5.4}$$

where R_1 and R_2 are the resources used by units 1 and 2, respectively, k_1 and k_2 their respective unit costs, and $\vec{z}_1$ and $\vec{z}_2$ the set of independent variables for each unit used in the optimization of each unit. Constraints (5.5.3) and (5.5.4) require that the coupling functions take on values of ξ and ψ such that

$$u_{12\,max} \le \xi \le u_{12\,min} \tag{5.5.5}$$

$$u_{21\,max} \le \psi \le u_{21\,min} \tag{5.5.6}$$

The cost of operating each unit is clearly identified in Problem (5.5). The contribution of each unit to the overall objective C is a function of the variables of each unit and the values ξ and ψ of the coupling functions. Therefore, for a given set of values ξ and ψ of the coupling functions, Problem (5.5) can easily be decomposed into two sub-problems, one for each of the units, i.e.

Sub-problem 1:

$$\text{Minimize } C_1 = k_1 R_1\left(\vec{z}_1, \xi, \psi\right) \tag{5.6}$$

w.r.t. $\vec{z}_1$ and subject to

$$\vec{h}_1 = \vec{0} \tag{5.6.1}$$

$$\vec{g}_1 \le \vec{0} \tag{5.6.2}$$

Sub-problem 2:

Minimize $C_2 = k_2 R_2\left(\vec{z}_2, \xi, \psi\right)$ (5.7)

w.r.t. $\vec{z}_2$ and subject to

$$\vec{h}_2 = \vec{0} \tag{5.7.1}$$

$$\vec{g}_2 \le \vec{0} \tag{5.7.2}$$

where for purposes of simplification it has been assumed that the capital costs are zero. Thus, Problem (5.5) is effectively reduced to two smaller problems (Problems (5.6) and (5.7)) by physical decomposition. Problems (5.6) and (5.7) have to be solved several times for different values of ξ and ψ of the coupling functions u_{12} and u_{21}. The values selected for the coupling functions must be included within the limits given by expression (5.5.5) and (5.5.6). It is assumed in using LGO that it is possible to find different sets of values for the independent variable vectors $\vec{z}_1$ and $\vec{z}_2$ which correspond to particular values ξ and ψ of u_{12} and u_{21}.

The results for sub-problems 1 and 2 are a set of optimum values for each objective as a function of the coupling functions such that

$$C_1^* = \min\left(k_1 R_1\left(\vec{z}_1, \xi, \psi\right)\right) \tag{5.8}$$

$$C_2^* = \min\left(k_2 R_2\left(\vec{z}_2, \xi, \psi\right)\right) \tag{5.9}$$

Equations (5.8) and (5.9) imply that there exists a set of unit optimum independent variable vectors $\vec{z}_1^*$ and $\vec{z}_2^*$ that satisfy

$$C_1^* = k_1 R_1\left(\vec{z}_1^*, \xi, \psi\right) \tag{5.10}$$

and $$C_2^* = k_2 R_2\left(\vec{z}_2^*, \xi, \psi\right) \tag{5.11}$$

for each set of values ξ and ψ of the coupling functions u_{12} and u_{21}. Graphically this is shown in Figure 5.2 where each local or unit-level optimum of the local objectives C_1 and C_2 are plotted as a function of the coupling functions u_{12} and u_{21}. A vector of optimum

values for the system-level objective function results from combinations of the sum of the optimum solutions found by solving the local sub-problems, Problems (5.6) and (5.7), i.e. $C^* = C_1^* + C_2^*$.

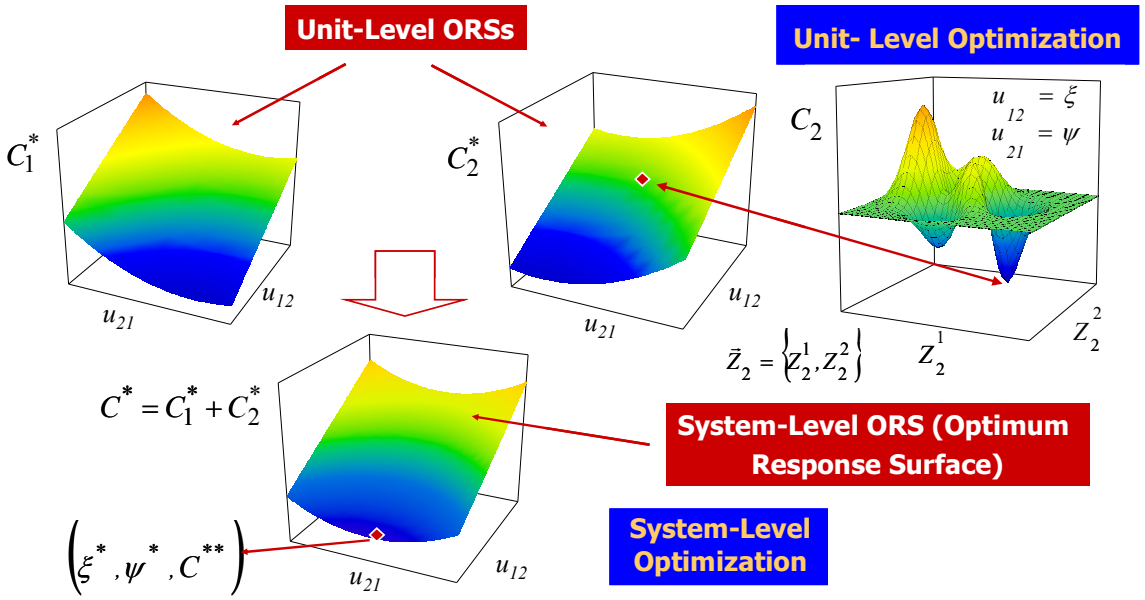

Figure 5.2 Local (unit-level) and global (system-level) optimizations (Rancruel, 2005).

In fact, every point of C^*_1 and C^*_2 versus u_{12} and u_{21} represents a local or unit-level optimum. When these two surfaces called unit-level Optimum Response Surfaces (ORSs) are combined, they form what is called the system-level ORS[3] for the system as a whole (see Figure 5.2). The system-level ORS defines the global or system-level problem given by

$$\text{Minimize } C^* = k_1 R_1(\xi, \psi) + k_2 R_2(\xi, \psi) \tag{5.12}$$

w.r.t. ξ, ψ

$$\text{subject to } \vec{G} = \begin{bmatrix} \xi - u_{12\,\max} \\ -\xi + u_{12\min} \\ \psi - u_{21\,\max} \\ -\psi + u_{21\min} \end{bmatrix} \leq \vec{0} \tag{5.12.1}$$

This system-level optimization problem consists of finding the optimum values of the coupling functions, ξ^* and ψ^*, that minimize the global or system-level objective. At

[3] For a system with more than two coupling functions, the ORS is in fact a hyper-surface.

the system-level, the independent variable vectors $\vec{z}_1$ and $\vec{z}_2$ of each unit do not appear. This is because of the assumption made earlier that there are a unique set of local or unit-level optimum values $\vec{z}_1^*$ and $\vec{z}_2^*$ for every combination of ξ and ψ.

The LGO technique has the advantage of breaking a large problem into smaller sub-problems that can be solved simultaneously. The drawback is the computational burden that this approach has for large, complex systems since each sub-problem must be solved independently many times in order to generate the system-level ORS (whether explicitly or implicitly). This is further compounded by the need for heuristic algorithms to deal with a mix of real and integer variables in the optimization and by the use of computationally expensive (unit) analyzers (i.e. simulators). To circumvent these drawbacks, Muñoz and von Spakovsky (2000a,b,c,d; 2001a,b) developed the Iterative Local-Global Optimization (ILGO) approach.

There are two complementary versions of this approach: ILGO-A and ILGO-B. Both are presented in the following sections. However, before proceeding, the algorithm for LGO is summarized as follows[4]:

- Identify the independent variable vectors ($\vec{z}_1$ and $\vec{z}_2$) and the coupling functions (u_{12} and u_{21}).
- Define and solve the unit-level optimization problems (Problems (5.9) and (5.10)) for different values of ξ and ψ of the coupling functions u_{12} and u_{21} and find a set of local or unit optimum values $\vec{z}_1^*$ and $\vec{z}_2^*$ for every combination of ξ and ψ.
- Define and solve the system-level optimization problem (Problem (5.12)).

5.4 The Iterative Local-Global Optimization (ILGO) Approach

In addition to not having the drawbacks outlined in the previous section for LGO, the ILGO decomposition strategy is an advance over LGO in that it

- eliminates the nested optimizations (whether implicit or explicit) required in standard local-global decomposition approaches;

[4] Note that LGO always results in a explicit or implicit nesting of unit-level optimizations (problems (5.6) and (5.7)) within an overall system-level optimization (problem (5.12)).

- uses an intelligent search based on shadow prices to effectively search the system-level ORS(s) without having to actually generate the ORS(s);
- assures consistency between all local objectives and the system-level objective;
- introduces no constraint inconsistencies from one sub-problem to another;
- is conducive to the parallelization of the various sub-problem optimizations.

In addition, ILGO makes possible the decentralized, integrated synthesis/design and operation/control optimization of systems by allowing multiple platforms and software tools as well as geographically dispersed and discipline diverse teams of engineers to effectively interact both at the unit (local) and the system (global) levels. In the following sections, two versions of ILGO (ILGO-A and ILGO-B) are presented. Even though the presentation is only given for a two unit system (as was done with the LGO approach), both approaches are completely general and applicable to any multiple unit system. In addition, they are applicable whether or not a system is hierarchical[5] or non-hierarchical.

The Iterative Local-Global Optimization (ILGO) approach eliminates the need for implicitly or explicitly (Muñoz and von Spakovsky, 2000a,b,c,d; 2001a,b) creating the ORSs by using a first order Taylor series expansion to approximate the local behavior of the system-level ORS. A formal presentation of this method is given below. Consider a modified version of Problems (5.6) and (5.7) where the two sub-problems are now solved for particular values ξ_o and ψ_o of the coupling functions u_{12} and u_{21}, i.e.

Sub-problem 1:

$$\text{Minimize} \quad C_1 = k_1 R_1\left(\vec{z}_1, \xi_o, \psi_o\right) \tag{5.13}$$

w.r.t. $\vec{z}_1$ and subject to

$$\vec{h}_1 = \vec{0} \tag{5.13.1}$$

$$\vec{g}_1 \le \vec{0} \tag{5.13.2}$$

Sub-problem 2:

$$\text{Minimize} \quad C_2 = k_2 R_2\left(\vec{z}_2, \xi_o, \psi_o\right) \tag{5.14}$$

[5] In a hierarchical system, all the components flow from a principal component.

w.r.t. $\vec{z}_2$, subject to

$$\vec{h}_2 = \vec{0} \tag{5.14.1}$$

$$\vec{g}_2 \le \vec{0} \tag{5.14.2}$$

The resulting values for the optimum solutions are $(C_1^*)_0$ and $(C_2^*)_0$ with corresponding independent variable vectors $(\vec{z}_1^*)_0$ and $(\vec{z}_2^*)_0$. The subscript o that accompanies the optimum solutions serves as a reminder that they are calculated at the initial or reference point. At this point, a first-order Taylor series expansion of the unit-level objective functions is performed about the ORS reference point and the linear terms are taken so that

$$C_1^* = \left(C_1^*\right)_o + \left(\frac{\partial C_1^*}{\partial u_{12}}\right)_o \Delta u_{12} + \left(\frac{\partial C_1^*}{\partial u_{21}}\right)_o \Delta u_{21} \tag{5.15}$$

$$C_2^* = \left(C_2^*\right)_o + \left(\frac{\partial C_2^*}{\partial u_{12}}\right)_o \Delta u_{12} + \left(\frac{\partial C_2^*}{\partial u_{21}}\right)_o \Delta u_{21} \tag{5.16}$$

The partial derivatives in equation (5.15), which are in fact "shadow prices[6]" (von Spakovsky and Evans, 1993), are evaluated at the optimum value C_1^* of the objective for sub-problem 1 based on the choice of ξ_o and ψ_o for u_{12} and u_{21}, respectively. In fact geometrically, these partial derivatives or shadow prices are the slopes of the unit-level ORS at each local (unit-level) optimum point in the u_{12} and u_{21} directions. The shadow prices indicate the relative importance of the coupling functions in terms of the overall system-level objective. Similarly, for sub-problem 2, a set of shadow prices, i.e. slopes, of the surface for unit 2 at ξ_o and ψ_o can be found. Using a more compact notation, equations (5.15) and (5.16) can be written as follows:

$$C_1^* = \left(C_1^*\right)_0 + \lambda_{12}^1 \Delta u_{12} + \lambda_{21}^1 \Delta u_{21} \tag{5.17}$$

$$C_2^* = \left(C_2^*\right)_0 + \lambda_{12}^2 \Delta u_{12} + \lambda_{21}^2 \Delta u_{21} \tag{5.18}$$

[6] A "shadow price" is a type of "marginal cost" since it represents the marginal cost associated with marginal changes in a unit-level or local objective's optimum value with respect to marginal changes in the value of an associated coupling function.

Depending on the sign and absolute value of the partial derivatives or shadow prices for units 1 and 2, an improved restricted optimum[7] value of the system-level objective given by

$$C^* = \left(C_1^*\right)_o + \left(C_2^*\right)_o + \left(\lambda_{12}^1 + \lambda_{12}^2\right)_o \Delta u_{12} + \left(\lambda_{21}^1 + \lambda_{21}^2\right)_o \Delta u_{21} \tag{5.19}$$

can be obtained by changing the values of the coupling functions in the directions and with the magnitudes indicated by the shadow prices. Equation (5.19) is obviously a construction of the restricted optimum local objectives, equations (5.15) and (5.16), and furthermore represents the restricted system-level optimum point which appears on the ORS for the system-level optimization given in Figure 5.2.

The feasibility of solving the optimization problem as stated in equations (5.10) and (5.11) is based on the existence of a set of vectors $\bar{z}_1^*$ and $\bar{z}_2^*$ for each set of values ξ and ψ that minimizes each unit objective function and satisfies the unit constraints. However, this assumption, that every combination of ξ and ψ leads to a feasible solution, may not be warranted for some systems. In fact, it is possible to find simultaneous increases in u_{12} and u_{21}, which due to the characteristics of the units are not physically possible. For these reasons, it is necessary to reformulate the unit-level optimization problems as follow:

Sub-problem 1[8]:

$$\text{Minimize } C_1^{'} = C_1 + \left(C_2^*\right)_o + \left(\lambda_{12}^2\right)_o \Delta u_{12}{}^{(1)} + \left(\lambda_{21}^2\right)_o \Delta u_{21}{}^{(1)} \tag{5.20}$$

w.r.t. $\bar{z}_1$ and subject to the same constraints as in Problem (5.13)

Sub-problem 2:

$$\text{Minimize } C_2^{'} = C_2 + \left(C_1^*\right)_o + \left(\lambda_{12}^1\right)_o \Delta u_{12}{}^{(2)} + \left(\lambda_{21}^1\right)_o \Delta u_{21}{}^{(2)} \tag{5.21}$$

w.r.t. $\bar{z}_2$ and subject to the same constraints as in Problem (5.14)

The above sub-problems have the advantage that in searching for the global optimum for the system as a whole, only values of the independent variables close to the previous

[7] "Restricted optimum" refers to the fact that this is an intermediate system-level optimum on the path to the overall or global system optimum.

[8] Note that this problem is the minimization of cost in unit 1 plus the projected change in cost in the rest of the system (in this case, unit 2) as a consequence of the variation of the local independent variables.

optimum solutions $(\vec{z}_1^*)_0$ and $(\vec{z}_2^*)_0$ found for sub-problems 1 and 2, which lead to feasible solutions, are allowed to participate in the current optimizations of sub-problems 1 and 2. The expressions for the objective functions C_1' and C_2', i.e. equations (5.20) and (5.21), take into account the fact that variations in the independent (decision) variables of the unit being optimized have an impact on the local (unit-level) objective function of both units. For example, variations in the decision variables of unit 1, namely, $(\vec{z}_1^*)_0$, cause changes $\Delta u_{12}^{(1)}$ and $\Delta u_{21}^{(1)}$ in the coupling functions u_{12} and u_{21}, respectively, according to the following relationships:

$$\Delta u_{12}^{(1)} = \frac{\partial u_{12}}{\partial \vec{z}_1} \Delta \vec{z}_1 \tag{5.22}$$

$$\text{and } \Delta u_{21}^{(1)} = \frac{\partial u_{21}}{\partial \vec{z}_1} \Delta \vec{z}_1 \tag{5.23}$$

where the superscript (1) indicates that the changes in the coupling functions are due to variations in $\vec{z}_1$ only[9]. These changes translate into a variation in the optimum value of the local objective function of unit 1 *and* unit 2. The impact on the local objective function of unit 2 (when solving Problem (5.20)) is taken into consideration through the shadow prices (the λ's), i.e.

$$\lambda_{12}^2 \equiv \left(\frac{\partial C_2^*}{\partial u_{12}} \right)_o \tag{5.24}$$

$$\text{and } \lambda_{21}^2 \equiv \left(\frac{\partial C_2^*}{\partial u_{21}} \right)_o \tag{5.25}$$

Therefore, Problems (5.20) and (5.21) are not strictly speaking local or unit-level sub-problems. In the work of Muñoz and von Spakovsky (2000a,b,c,d; 2001a,b) such problems are called *unit-based, system-level optimization problems* since in effect system-level information has now been embedded directly into each local or unit-level objective. It is this embedding that leads to the more general nature of ILGO over LGO

[9] In the same fashion, superscript (2) indicates that the changes in the coupling functions are due to a variation in $\vec{z}_2$ only.

and to the very desirable ILGO feature of eliminating the nested optimizations from which LGO suffers.

Thus, an iterative procedure called ILGO is established where by starting with random values of the coupling functions, new values (ξ and ψ) for these functions are selected based on the slopes. ILGO, therefore, moves intelligently using the shadow prices towards the global (system-level) optimum[10] without having to actually create the ORS in Figure 5.4 or any of the local surfaces shown in Figure 5.3. This and the fact that no nested optimizations of local (unit-level) within global (system-level) are required prove to be major advantages.

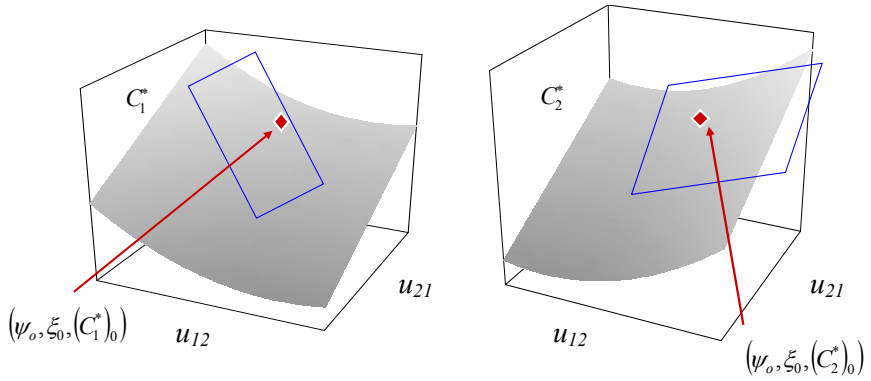

Figure 5.3 Initial restricted unit or local - level optimum points (Rancruel, 2005).

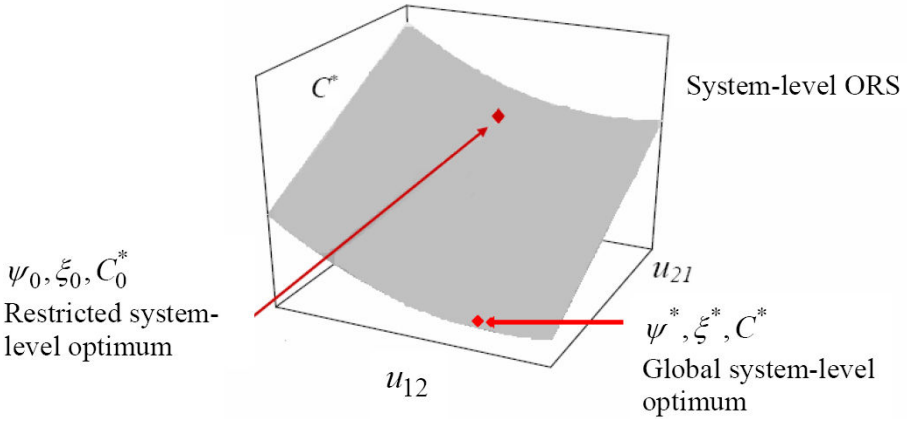

Figure 5.4 The restricted and global system-level optimum points on the system-level ORS.

The algorithm for the ILGO approach as given in Muñoz and von Spakovsky (2000a,b,c,d; 2001a,b) is as follows:

[10] Again, this is meant in an engineering sense.

1- Obtain an initial point of the optimum response surface with u_{12} and u_{21} equal to ξ_o and ψ_o by solving the optimization sub-problems.

2- Calculate the partial derivatives (shadow prices) of the restricted optimum values of the local objective functions C_1^* and C_2^* with respect to ξ and ψ

3- Estimate the maximum allowable values of Δu_{12} and Δu_{21}[11]. If no information is available, assume that the partial derivatives are constant over most of the optimum response surface.

4- The unit-based system-level optimization Problems (5.20) and (5.21) are defined and solved subject to the additional constraint that the values of the increment have to be constrained by a maximum (see Georgopoulos, 2002).

5- Finally, the solutions from the previous step are used to update $\left(\vec{z}_1^*\right)_o$, $\left(\vec{z}_2^*\right)_o$ and ξ_o and ψ_o. Repeat the procedure until no improvement is achieved or until the coupling functions have reached the minimum allowable values.

5.5 Dynamic Iterative Local-Global Optimization (DILGO)

Figure 5.5 shows the physical decomposition of a dynamic system made up of two subsystems applying ILGO. The feedback controllers generate a set of controlled inputs $\vec{w}$ to each unit, which are intended to regulate the set of inputs $\vec{R}$ in order to produce the set of outputs $\vec{P}$ according to pre-defined output reference values $\vec{S}$. As before the streams connecting the two units (i.e. coupling functions) are represented by $\vec{u}$.

Applying physical decomposition (i.e. ILGO) to this two unit system, the following system-level, unit-based optimization problems for each unit are defined:

Sub-problem 1:

$$\text{Minimize } C_1' = C_1 + \left(C_2^*\right)_o + \left(\frac{\partial C_2^*}{\partial u_{12}}\right)_o \Delta u_{12}^{(1)} + \left(\frac{\partial C_2^*}{\partial u_{21}}\right)_o \Delta u_{21}^{(1)} \tag{5.26}$$

w.r.t. $\vec{x}_1, \vec{y}_1, \vec{K}_1$ and subject to a known set of constraints.

Sub-problem 2:

[11] Note that the values of the coupling function could be limited by physical constraints within the system.

$$\text{Minimize } C_2' = C_2 + \left(C_1^*\right)_o + \left(\frac{\partial C_1^*}{\partial u_{12}}\right)_o \Delta u_{12}{}^{(2)} + \left(\frac{\partial C_1^*}{\partial u_{21}}\right)_o \Delta u_{21}{}^{(2)} \tag{5.27}$$

w.r.t. $\vec{x}_2, \vec{y}_2, \vec{K}_2$ and subject to a known set of constraints

and where the $\vec{x}_1$ and $\vec{x}_2$, $\vec{y}_1$ and $\vec{y}_2$, and $\vec{K}_1$ and $\vec{K}_2$ are the synthesis/design, operation and control decision variables, respectively. Unfortunately, the optimization sub-problems defined in this way are not well suited for handling a dynamic process. For instance, the coupling functions $\vec{u}_{ij}$ are changing with time and, therefore, the term Δu_{ij} cannot be defined as the difference of steady state values or the difference of steady state values at the end of a transient. For the same reason the shadow price $\left(\frac{\partial C_i^*}{\partial u_{ij}}\right)$ cannot be defined as is, because its value changes as well with the transient. Thus, in order to adequately use the concepts behind the ILGO approach, two techniques are proposed.

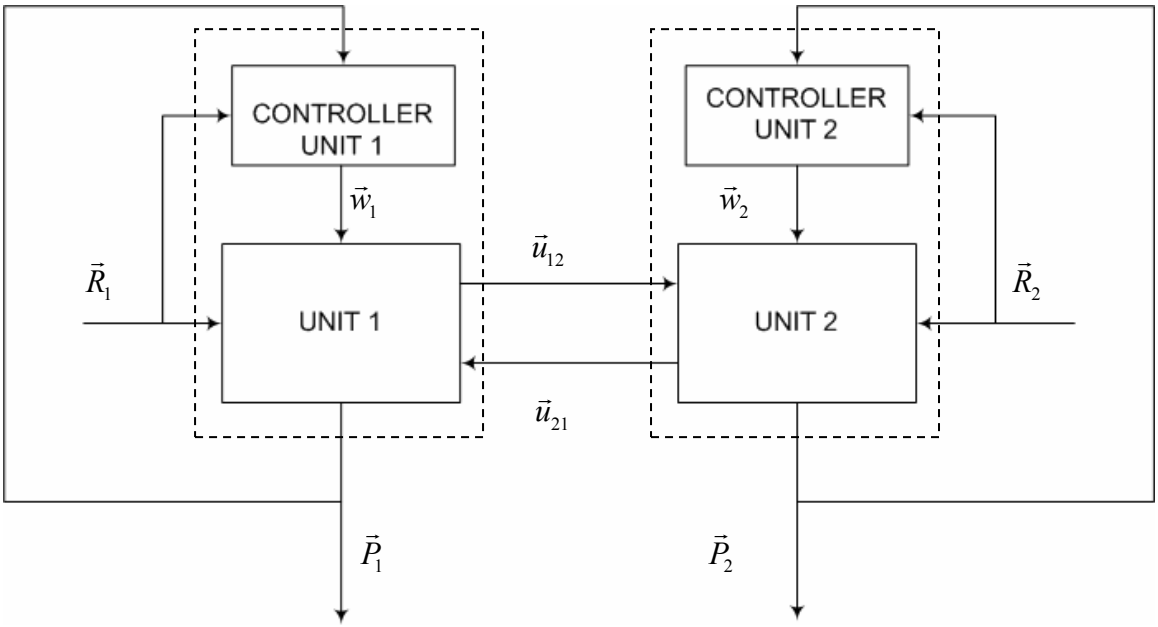

Figure 5.5 Physical decomposition and control subsystem considerations (Rancruel, 2005).

In order to understand the level of complexity of the problem at hand let us first define the unit-level optimization problems as follow:

Unit 1:

$$\text{Minimize } C_1 = \sum_{k=1}^{\tau} \int_{t_{k-1}}^{t_k} \dot{C}_1\left(\vec{x}_1, \vec{y}_{1k}, \dot{\vec{y}}_{1k}, \vec{u}_{12k}, \vec{u}_{21k}, \vec{w}_1, \vec{K}_1\right) dt \tag{5.28}$$

w.r.t. $\vec{x}_1$, $\vec{y}_{1k}$, $\vec{K}_1$ and subject to a known set of constraints

and where $\dot{\vec{y}}_{1k}$ is the time rate of change vector of the operational state variables for unit 1, and $\vec{w}_1$ and $\vec{u}_{12k}$ are defined as

$$\vec{w}_1 = f\left(\vec{x}_1, \vec{y}_{1k}, \dot{\vec{y}}_{1k}, \vec{u}_{12k}, \vec{u}_{21k}, \vec{S}_1, \vec{P}_1, \vec{K}_1\right) \tag{5.28a}$$

$$\vec{u}_{12k} = f\left(\vec{x}_1, \vec{y}_{1k}, \dot{\vec{y}}_{1k}, \vec{u}_{21k}, \vec{w}_1\right) \tag{5.28b}$$

Unit 2:

$$\text{Minimize } C_2 = \sum_{k=1}^{\tau} \int_{t_{k-1}}^{t_k} \dot{C}_1\left(\vec{x}_2, \vec{y}_{2k}, \dot{\vec{y}}_{2k}, \vec{u}_{12k}, \vec{u}_{21k}, \vec{w}_2, \vec{K}_2\right) dt \tag{5.29}$$

w.r.t. $\vec{x}_2$, $\vec{y}_{2k}$, $\vec{K}_2$ and subject to a known set of constraints

and where $\dot{\vec{y}}_{2k}$ is the time rate of change vector of the operational state variables of unit 2, and $\vec{w}_2$ and $\vec{u}_{21k}$ are defined as

$$\vec{w}_2 = f\left(\vec{x}_2, \vec{y}_{2k}, \dot{\vec{y}}_{2k}, \vec{u}_{12k}, \vec{u}_{21k}, \vec{S}_2, \vec{P}_2, \vec{K}_2\right) \tag{5.29a}$$

$$\vec{u}_{21k} = f\left(\vec{x}_2, \vec{y}_{2k}, \dot{\vec{y}}_{2k}, \vec{u}_{12k}, \vec{w}_2\right) \tag{5.29b}$$

Here, the limit on the summation indicates that the dynamic load profile is divided into τ dynamic segments, each segment as indicated in equations (5.28) and (5.29) requiring an integration over the interval t_{k-1} to t_k. These definitions of the optimization sub-problems show a highly coupled dynamic system where the transient response not only depends on the system synthesis/design but also on the controller design, the coupling functions, the actual values of the dynamic operational state variables (initial conditions) and the product and reference values. Additional complexity appears due to the fact that the boundary between coupling functions, unit products, reference values, and control variables is not always clear, i.e. the coupling functions and control variables can be defined as unit products or unit resources.

Now, using the concept of the cost rate $\dot{C}$ introduced in equations (5.28) and (5.29), the dynamic system-level, unit-based optimization problems for units 1 and 2 are given by

Unit 1:

Minimize

$$C_1^{'} = \sum_{k=1}^{\tau}\left(\int_{t_{k-1}}^{t_k} \dot{C}_1(t)dt + \int_{t_{k-1}}^{t_k} \dot{C}_2^*(t)dt + \int_{t_{k-1}}^{t_k} \left(\frac{\partial \dot{C}_2^*(t)}{\partial u_{12}(t)} \right) \Delta u_{12}(t)dt + \int_{t_{k-1}}^{t_k} \left(\frac{\partial \dot{C}_2^*(t)}{\partial u_{21}(t)} \right) \Delta u_{21}(t)dt \right)$$
$$= \sum_{k=1}^{\tau}\left(C_1 + C_2^* + \int_{t_{k-1}}^{t_k} \left(\frac{\partial \dot{C}_2^*(t)}{\partial u_{12}(t)} \right) \Delta u_{12}(t)dt + \int_{t_{k-1}}^{t_k} \left(\frac{\partial \dot{C}_2^*(t)}{\partial u_{21}(t)} \right) \Delta u_{21}(t)dt \right) \quad (5.30)$$

w.r.t. $\vec{x}_1$, $\vec{y}_{1k}$, $\vec{K}_1$ and subject to a known set of constraints

Unit 2:

Minimize

$$C_2^{'} = \sum_{k=1}^{\tau}\left(\int_{t_{k-1}}^{t_k} \dot{C}_2(t)dt + \int_{t_{k-1}}^{t_k} \dot{C}_1^*(t)dt + \int_{t_{k-1}}^{t_k} \left(\frac{\partial \dot{C}_1^*(t)}{\partial u_{21}(t)} \right) \Delta u_{21}(t)dt + \int_{t_{k-1}}^{t_k} \left(\frac{\partial \dot{C}_1^*(t)}{\partial u_{12}(t)} \right) \Delta u_{12}(t)dt \right)$$
$$= \sum_{k=1}^{\tau}\left(C_2 + C_1^* + \int_{t_{k-1}}^{t_k} \left(\frac{\partial \dot{C}_1^*(t)}{\partial u_{21}(t)} \right) \Delta u_{21}(t)dt + \int_{t_{k-1}}^{t_k} \left(\frac{\partial \dot{C}_1^*(t)}{\partial u_{12}(t)} \right) \Delta u_{12}(t)dt \right) \quad (5.31)$$

w.r.t. $\vec{x}_2$, $\vec{y}_{2k}$, $\vec{K}_2$ and subject to a known set of constraints

and where the dynamic shadow price rate based on the dynamic restricted local (unit-based) optimum cost rate and coupling function is defined as

$$\dot{\lambda}_{ij}^{i} = \dot{\lambda}_{ij}^{i}(u_{ij}, t) \equiv \left(\frac{\partial \dot{C}_i^*(t)}{\partial u_{ij}(t)} \right) \quad (5.32)$$

Using this last definition, problems (5.30) and (5.31) can be written as

Unit 1:

$$\text{Minimize } C_1^{'} = \sum_{k=1}^{\tau}\left(C_1 + C_2^* + \int_{t_{k-1}}^{t_k} \dot{\lambda}_{12}^2(u_{12}, t)\Delta u_{12}(t)dt + \int_{t_{k-1}}^{t_k} \dot{\lambda}_{21}^2(u_{21}, t)\Delta u_{21}(t)dt \right) \quad (5.33)$$

w.r.t. $\vec{x}_1$, $\vec{y}_{1k}$, $\vec{K}_1$ and subject to

$$\vec{h}_{1k} = \vec{0} \quad (5.33.1)$$

$$\vec{g}_{1k} \leq \vec{0} \quad (5.33.2)$$

Unit 2:

$$\text{Minimize } C_2' = \sum_{k=1}^{\tau}\left(C_2 + C_1^* + \int_{t_{k-1}}^{t_k} \lambda_{21}^{1}(u_{21},t)\Delta u_{21}(t)dt + \int_{t_{k-1}}^{t_k} \lambda_{12}^{1}(u_{12},t)\Delta u_{12}(t)dt \right) \quad (5.34)$$

w.r.t. $\vec{x}_2$, $\vec{y}_{2k}$, $\vec{K}_2$ and subject to

$$\vec{h}_{2k} = \vec{0} \quad (5.34.1)$$

$$\vec{g}_{2k} \leq \vec{0} \quad (5.34.2)$$

The additional set of constraints

$$\Delta u_{ij\,k} - \varepsilon\ \Delta u_{ij\,k\,\max} \leq 0 \quad (5.35)$$

are also imposed for each sub-problem. In this expression, $\Delta u_{ij\,k\,\max}$ are the maximum allowable values for the coupling functions and the factor ε is added to ensure that the linear Taylor series expansions are a good local representation of the optimum response surface.

The definition of dynamic shadow price rate (equation (5.32)) and its utilization in the dynamic system-level, unit-based optimization Problems (5.33) and (5.34) is well suited for handling the optimization of highly dynamic systems for which no quasi-stationary process assumption can be made. However, the computation of the actual value of the dynamic shadow price rates may become rather time consuming if the system at hand has a very fast dynamic behavior or the transient segments make up most of the load profile. If this is the case it may be useful to define a shadow price not in terms of a dynamic shadow price rate but instead in terms of a shadow price based on the integral of coupling function change over time. However, since that is not the approach here, details of how this is done are not presented here and the reader if interested is referred to Rancruel (2005) instead.

5.6 Applying DILGO to the Dynamic PEMFC Synthesis/Design and Operation/Control Optimization Problem

This chapter presents in detail the procedure followed for the dynamic synthesis/design and operation/control optimization of the proposed PEMFC system, using physical decomposition. The system is decomposed into three different subsystems, the FPS, SS, and WRAS and the coupling functions describing their system-level

interactions are presented. The decomposed optimization problems for the three units considered are defined and the DILGO approach presented in the previous chapter is applied.

5.6.1 System-Level Dynamic Optimization Problem Definition

The interdependence between the three units (subsystem) being synthesized/designed and operated/controlled (the SS, FPS, and WRAS) is quite tight. The result is that the fuel cell system (FCS) at hand constitutes the typical case of a system in which "everything influences everything else". Thus, determining the optimal synthesis/design and dynamic operation/control of the FCS requires that the optimal synthesis/design and dynamic operation/control of each of the subsystem be carried out in an integrated fashion. Individually optimizing each subsystem without consideration for their integration with the rest of the system does not lead to the optimum for the system as a whole. The decomposition approach DILGO described above is a means by which each subsystem can be individually optimized consistent with its integration into the overall system. It is particularly suited to handle the system dynamics which is important when optimizing a system operating under transient conditions for a large fraction of its life cycle. Additionally, these systems can be subject to sudden load changes of considerable magnitude.

How DILGO is applied is discussed in this chapter. However, the next section begins with a description of the overall dynamic system synthesis/design and operation/control optimization problem and is followed in the remaining sections of this chapter with a description of each of the subsystem optimization problems. What follows is the overall system problem definition in terms of total life cycle cost as the objective function.

The system-level optimization problem is that of minimizing the total cost of the system through its entire life cycle. It is formulated as follows in terms of the capital cost of each subsystem and the total operation/control cost:

$$\text{Minimize } C_{\mathrm{T}} = C_{SS} + C_{FPS} + C_{WRAS} + C_{PES} + C_{BBS} + \int_{t=0}^{T} \dot{C}_{fuel} dt \tag{5.36}$$

w.r.t. $\{\bar{x}_{SS}, \bar{y}_{SS}, \vec{K}_{SS}\}$, $\{\bar{x}_{FPS}, \bar{y}_{FPS}, \vec{K}_{FPS}\}$, $\{\bar{x}_{WRAS}, \bar{y}_{WRAS}, \vec{K}_{WRAS}\}$ and subject to

$$\vec{H}_{SS} = \vec{0}, \quad \vec{G}_{SS} \le \vec{0} \tag{5.36.1a, b}$$

$$\vec{H}_{FPS} = \vec{0}, \quad \vec{G}_{FPS} \le \vec{0} \tag{5.36.2a, b}$$

$$\vec{H}_{WRAS} = \vec{0}, \quad \vec{G}_{WRAS} \le \vec{0} \tag{5.36.3a, b}$$

Note that C_{BBS}, and C_{PES} which represent the capital amortization and maintenance costs of the battery bank and power electronics subsystems are assumed fixed and are, thus, not minimized along with the rest of the objective, which consists of the capital, amortization and maintenance costs of each of the remaining subsystems and their associated fuel cost penalties. Thus, C_{SS}, C_{FPS}, and C_{WRAS} represent the capital, amortization, and maintenance costs while $\dot{C}_{fuel}$ is the fuel cost rate which is integrated over the total life cycle (from time zero to time T). For this research work, it is important to note that the optimization problem is being solve not only in terms of the synthesis/design and operational decision variables, $\vec{x}$ and $\vec{y}$, but also in terms of a set of controller gains, $\vec{K}$, which are intended to optimize the system with respect to not only total cost but also the time response. Here, the system's time response to changes in load is set as a constraint.

5.6.2 Decomposition and Coupling Function Definitions

Figure 5.6 shows the selected coupling functions between subsystems. In order for the SS to produce the required gross power, the necessary molar flow rate of hydrogen in the hydrogen-rich gas stream, $\dot{n}_{H_2}$, must be supplied by the FPS at the appropriate pressure, P_{anode}. In the same way, the necessary molar flow rate of air, $\dot{n}_{air}$, must be supplied by the WRAS at $P_{cathode}$. The SS also must satisfy the power demand, $\dot{E}_{WRAS}$, to run the WRAS. The exhausting hydrogen, $\dot{n}_{H_2out}$, and exhausting air, $\dot{n}_{airout}$, is fed back into the FPS and WRAS, respectively.

The followings sections present the system-level, unit-based optimization problems for the three units considered, the SS, WRAS, and FPS, along with a detailed description of their independent (decision) variables and a definition of their dynamic shadow price rates. In each subsystem, the output/command coupling functions are selected to vary in

each system-level unit-based objective function, while the input coupling functions are set as constraints as shown in Table 5.1.

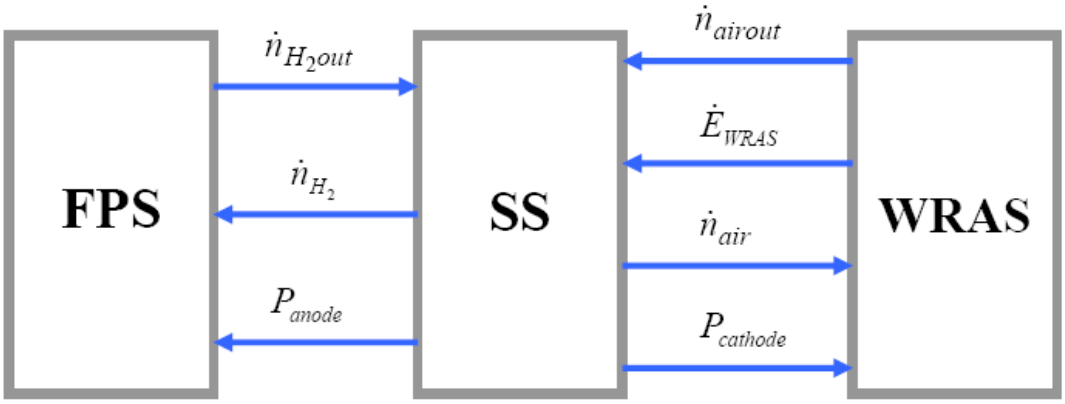

Figure 5.6 Coupling functions between FCS subsystems.

Table 5.1 Coupling functions considered in each subsystem optimization.

SubSystem	Coupling Function	Symbol
SS	Hydrogen flow rate	$\dot{n}_{H_2}$
	Air flow rate	$\dot{n}_{air}$
	System pressure	P_{anode} , $P_{cathode}$
FPS	Outlet hydrogen flow rate from SS	$\dot{n}_{H_2out}$
WRAS	Outlet air flow rate from SS	$\dot{n}_{airout}$
	Outlet air temperature	T_{air}
	Electricity from SS	$\dot{E}_{WRAS}$

5.6.3 SS System-Level, Unit-Based Optimization Problem Definition

The SS system-level, unit-based optimization problem is formulated as follows:

Minimize

$$C'_{SS} = C_{SS} + C^*_{FPS} + C^*_{WRAS} + \int_{t=0}^{T} \dot{\lambda}_{H_2}(t)\Delta\dot{n}_{H_2}(t)dt + \int_{t=0}^{T} \dot{\lambda}_{P_{anode}}(t)\Delta P_{anode}(t)dt + \int_{t=0}^{T} \dot{\lambda}_{air}(t)\Delta\dot{n}_{air}(t)dt + \int_{t=0}^{T} \dot{\lambda}_{P_{cathode}}(t)\Delta P_{cathode}(t)dt \quad (5.37)$$

w.r.t. N_{cells} , A_{cell} , T_{stack} , $\vec{K}_{SS}$ and subject to

$$\vec{h}_{SS} = \vec{0} \tag{5.37.1}$$

$$\vec{g}_{SS} \le \vec{0} \tag{5.37.2}$$

$$\begin{bmatrix} \dot{n}_{H_2out} - \dot{n}_{H_2out_{\max}} \\ \dot{n}_{airout} - \dot{n}_{airout_{\max}} \\ \dot{E}_{WRAS} - \dot{E}_{WRAS_{\max}} \end{bmatrix} = \vec{0} \tag{5.37.3}$$

where N_{cells} is the stack cell number, A_{cell} the activity area of each cell, T_{stack} the stack operation temperature, $\vec{K}_{SS}$ the controller gains, and the vector of equality constraints, $\vec{h}_{SS}$, represents the thermodynamic, kinetic, and geometric models of the SS while the vector of inequality constraints, $\vec{g}_{SS}$, represents physical limitations imposed upon the subsystem. The upper limit T on the integrals is the length of the load profile, i.e. 48 hours. Equation (5.37.3) indicates that the coupling functions $\dot{n}_{H_2out}$, $\dot{n}_{airout}$, and $\dot{E}_{WRAS}$ must take the proper values dictated by the solution of the WRAS and FPS system-level, unit-based optimization problems described in the following section. Furthermore, note that the summations over τ time intervals of transient behavior which appear in equations (5.33) and (5.34) are missing in equation (5.37) above. The reason is that for the optimizations performed here, each decision variable has only one optimum value in the entire load profile.

The shadow price rates are defined as

$$\dot{\lambda}_{H_2}(t) = \frac{\partial \dot{C}^*_{FPS}}{\partial \dot{n}_{H_2}(t)} \tag{5.38}$$

$$\dot{\lambda}_{P_{anode}}(t) = \frac{\partial \dot{C}^*_{FPS}}{\partial P_{anode}(t)} \tag{5.39}$$

$$\dot{\lambda}_{air}(t) = \frac{\partial \dot{C}^*_{WRAS}}{\partial \dot{n}_{air}(t)} \tag{5.40}$$

$$\dot{\lambda}_{P_{cathode}}(t) = \frac{\partial \dot{C}^*_{WRAS}}{\partial P_{cathode}(t)} \tag{5.41}$$

The $\dot{\lambda}$ represent the rate of marginal changes in the optimum value of the FPS and WRAS total costs due to marginal changes in the value of the coupling functions $\dot{n}_{H_2}$, P_{anode}, $\dot{n}_{air}$, and $P_{cathode}$, respectively.

Finally, the terms $\Delta\dot{n}_{H_2}$, ΔP_{anode}, $\Delta\dot{n}_{air}$, and $\Delta P_{cathode}$ characterize the effect that the variations in the SS decision variables have on the coupling functions and are given by

$$\Delta\dot{n}_{H_2} = \dot{n}_{H_2} - \dot{n}_{H_2}{}^0 \tag{5.42.1}$$

$$\Delta P_{anode} = P_{anode} - P_{anode}{}^0 \tag{5.42.2}$$

$$\Delta\dot{n}_{air} = \dot{n}_{air} - \dot{n}_{air}{}^0 \tag{5.42.3}$$

$$\Delta P_{cathode} = P_{cathode} - P_{cathode}{}^0 \tag{5.42.4}$$

where the superscript "0" refers to the final coupling function value obtained in the previous DILGO iteration.

5.6.4 FPS System-Level, Unit-Based Optimization Problem Definition

The system-level, unit-based optimization problem for the FPS is defined as follows:

$$\text{Minimize } C'_{FPS} = C_{FPS} + C^*_{SS} + C^*_{WRAS} + \int_{t=0}^{T} \dot{\lambda}_{H_2OUT}(t)\Delta\dot{n}_{H_2OUT}(t)dt \tag{5.43}$$

w.r.t. $\vec{x}_{FPS}$, $\vec{K}_{FPS}$ and subjet to

$$\vec{h}_{FPS} = \vec{0} \tag{5.43.1}$$

$$\vec{g}_{FPS} \le \vec{0} \tag{5.43.2}$$

$$\begin{bmatrix} \dot{n}_{H_2} - \dot{n}_{H_2\max} \\ P_{anode} - P_{anode_{\max}} \end{bmatrix} = \vec{0} \tag{5.43.3}$$

where the vector of equality constraints, $\vec{h}_{FPS}$, represents the thermodynamic, kinetic, and geometric models of the FPS while the vector of inequality constraints, $\vec{g}_{FPS}$, represents physical limitations imposed upon the subsystem. Equation (5.43.3) indicates that the coupling functions $\dot{n}_{H_2}$ and P_{anode} must take the proper values dictated by the solution of the SS system-level, unit-based optimization problem described in the previous section.

The shadow price rates are defined as

$$\dot{\lambda}_{H_2out}(t) = \frac{\partial \dot{C}^*_{SS}}{\partial \dot{n}_{H_2out}(t)} \tag{5.44}$$

The term $\Delta \dot{n}_{H_2out}$ is given by

$$\Delta \dot{n}_{H_2out} = \dot{n}_{H_2out} - \dot{n}_{H_2out}{}^0 \tag{5.45}$$

where the superscript "0" refers to the final coupling function value obtained in the previous DILGO iteration.

5.6.5 WRAS System-Level, Unit-Based Optimization Problem Definition

The WRAS system-level, unit-based optimization problem is formulated as follows:

$$\text{Minimize} \quad C'_{WRAS} = C_{WRAS} + C^*_{SS} + C^*_{FPS} + \int_{t=0}^{T} \dot{\lambda}_{airout}(t)\Delta \dot{n}_{airout}(t)dt + \int_{t=0}^{T} \dot{\lambda}_{\dot{E}_{WRAS}}(t)\Delta \dot{E}_{WRAS}(t)dt \tag{5.46}$$

w.r.t. $\vec{x}_{WRAS}$, $\vec{K}_{WRAS}$ and subjet to

$$\vec{h}_{WRAS} = \vec{0} \tag{5.46.1}$$

$$\vec{g}_{WRAS} \le \vec{0} \tag{5.46.2}$$

$$\begin{bmatrix} \dot{n}_{air} - \dot{n}_{air_{\max}} \\ P_{cathode} - P_{cathode_{\max}} \end{bmatrix} = \vec{0} \tag{5.46.3}$$

where the vector of equality constraints, $\vec{h}_{WRAS}$, represents the thermodynamic, kinetic and geometric models of the WRAS while the vector of inequality constraints, $\vec{g}_{WRAS}$, represents physical limitations imposed upon the subsystem. Equation (5.46.3) indicates that the coupling functions $\dot{n}_{air}$ and $P_{cathode}$ must take the proper values dictated by the solution of the SS system-level, unit-based optimization problem described in the previous section.

The shadow price rates are defined as

$$\dot{\lambda}_{airout}(t) = \frac{\partial \dot{C}^*_{SS}}{\partial \dot{n}_{airout}(t)} \tag{5.47}$$

$$\dot{\lambda}_{\dot{E}_{WRAS}}(t) = \frac{\partial \dot{C}^{*}_{SS}}{\partial \dot{E}_{WRAS}(t)} \tag{5.48}$$

The terms $\Delta \dot{n}_{airout}$, and $\Delta \dot{E}_{WRAS}$ are given by

$$\Delta \dot{n}_{airout} = \dot{n}_{airout} - \dot{n}_{airout}{}^{0} \tag{5.49.1}$$

$$\Delta \dot{E}_{WRAS} = \dot{E}_{WRAS} - \dot{E}_{WRAS}{}^{0} \tag{5.49.2}$$

where again the superscript "0" refers to the final coupling function value obtained in the previous DILGO iteration.

5.6.6 Solution Approach

The necessary steps for applying DILGO to the PEMFC system in order to identify the final synthesis/design and operational/control that minimizes the total life cycle cost over the entire load profile are summarized below:

1. Solve the system-level, unit-based optimization problem for the SS. Since no information about the FPS and the WRAS exists in the first iteration of DILGO, set the shadow price rates $\dot{\lambda}_{H_2}$, $\dot{\lambda}_{P_{anode}}$, $\dot{\lambda}_{air}$, and $\dot{\lambda}_{P_{cathode}}$, equal to zero and use initial estimates for the parasitic power demand, $\dot{E}_{WRAS}$, and the outlet flow rates $\dot{n}_{H_2out}$ and $\dot{n}_{airout}$.
2. Calculate the shadow price rates $\dot{\lambda}_{H_2out}$, $\dot{\lambda}_{airout}$, and $\dot{\lambda}_{\dot{E}_{WRAS}}$ based on the optimum SS capital cost C^{*}_{SS}. Each shadow price rate is a 48 hours profile, because a 48 hours load profile is applied in this dynamic operation.
3. Solve the system-level, unit-based optimization problem for the FPS unit with values of $\dot{\lambda}_{H_2out}$, $\dot{n}_{H_2}$, and P_{anode} calculated in steps 1 and 2. Also, solve the system-level, unit-based optimization problem for the WRAS unit with values of $\dot{\lambda}_{airout}$, $\dot{\lambda}_{\dot{E}_{WRAS}}$, $\dot{n}_{air}$, and $P_{cathode}$ calculated in steps 1 and 2.
4. Calculate the shadow prices based on the optimum FPS total cost C^{*}_{FPS}. Also, calculate the shadow prices based on the optimum WRAS total cost C^{*}_{WRAS}.

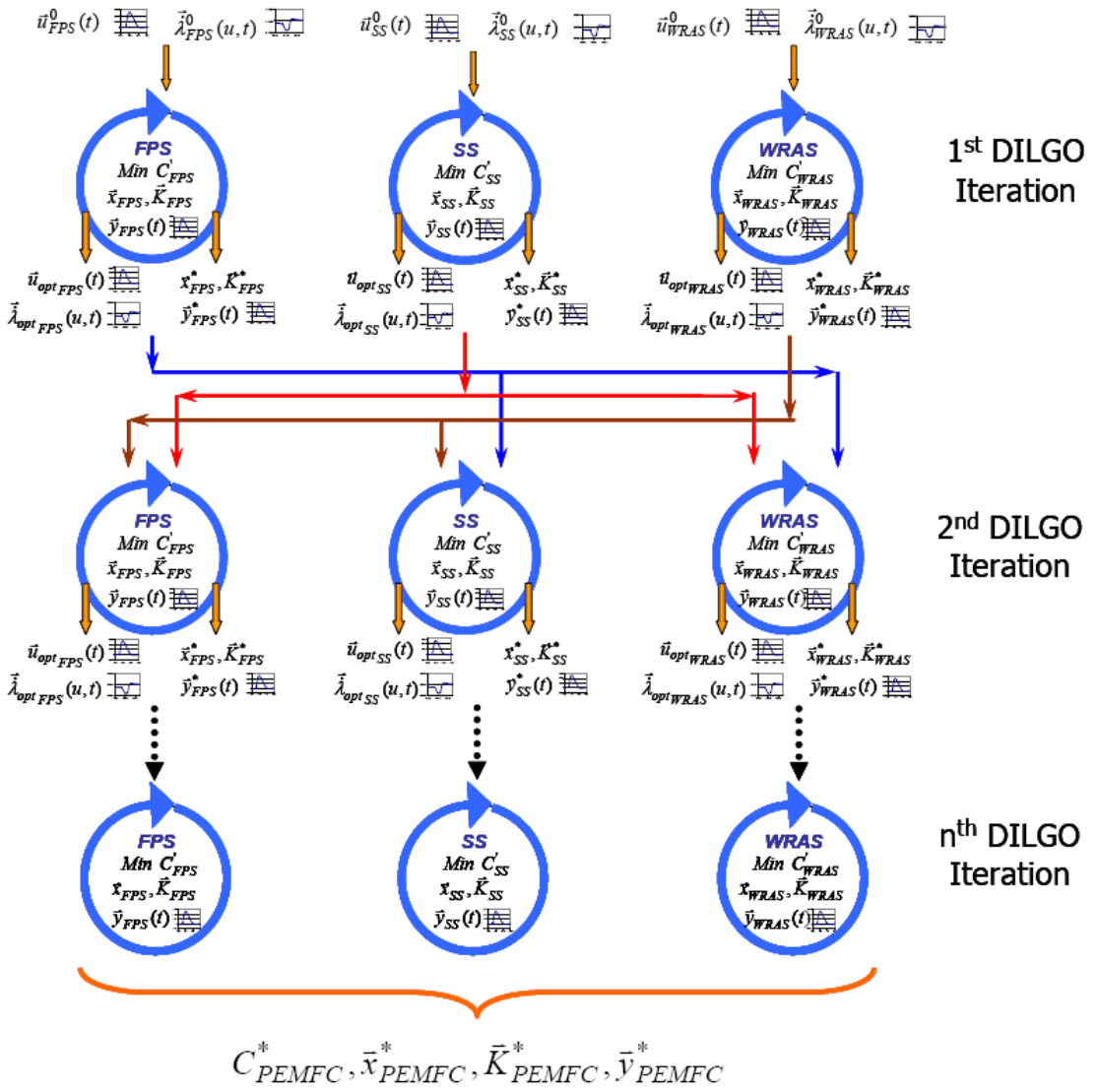

Figure 5.7 The DILGO decomposition strategy for optimization used in the multi-level synthesis/design and operation/control optimization of the 5kW PEMFC system.

5. Repeat steps 1 through 6 until no further improvement in the system-level objective function, i.e. C_{FCS}, is achieved or until the coupling functions have reached the minimum or maximum allowable values.
6. Identify the synthesis/design and dynamic/operational values of the decision variables that minimize the total cost of the FCS over the entire load profile.
7. Proceed with a control stability analysis. If stability problems are found, redefine the range for the control gains or apply conceptual decomposition by adding a new segment to the load profile which challenges the system. This was not necessary in this doctoral work.

The optimization tool of the commercial dynamic development environment package gPROMS® (2003) was used to solve optimization problems. This software provides a MINLP optimization algorithm suitable for solving dynamic problems. The procedure described above is the same regardless of whether or not the objective function is the total life cycle cost or system time response. Figure 5.7 shows the coupling function flows between subsystems and the system DILGO strategy for the optimization.

Once the shadow prices are computed for the first DILGO iteration and new feasible values of the coupling functions are defined, the second DILGO iteration can proceed. Thus, all the subsystem optimizations can be performed in parallel (see Figure 5.7) from the second DILGO iteration onward. At the end of each DILGO iteration, new values of the coupling functions are generated and new values of the shadow prices are computed. This information is updated into each subsystem optimization problem. The procedure from steps 1 to 6 is repeated until convergence is reached. Convergence implies that the variation in the system-level, unit-base objective function for each subsystem is below a predefined limit (e.g., less than 0.2 %).

5.6.7 Decision Variables in the PEMFC System Dynamic Synthesis/Design and Operation/Control Optimization

The PEMFC system dynamic synthesis/design and operation/control optimization decision variables considered in this research are listed in Table 5.2a and b.

Table 5.2a. FPS, WRAS, and SS control decision variables during optimization.

SS			**SS**		
Current Controller Gains	*K(1)*	*K(4)*	Fuel Utilization Controller Gains	*K(7)*	*K(10)*
	K(2)	*K(5)*		*K(8)*	*K(11)*
	K(3)	*K(6)*		*K(9)*	*K(12)*
WRAS			**FPS**		
Cooling Air Flow Rate Controller Gains	*K_c(1)*	*K_c(3)*	Reformate Temperature Controller Gains	*Kc(1)*	*Kc(3)*
	K_c(2)	*K_c(4)*		*Kc(2)*	*Kc(4)*
PEMFC Operating Pressure Controller Gains	*K_c(5)*	*K_c(7)*	Methane Inlet Flow Rate Controller Gains	*Kc(5)*	*Kc(7)*
	K_c(6)	*K_c(8)*		*Kc(6)*	*Kc(8)*

Table 5.2b. FPS, WRAS, and SS synthesis/design and operation decision variables during optimization.

Subsystem	Variable Definition	Variable Symbol	Subsystem	Variable Definition	Variable Symbol
FPS			**FPS**		
SMR	Length	L_{SMR} (m)	LTSR	Length	L_{LTSR} (m)
	Diameter	D_{SMR} (cm)		Diameter	D_{LTSR} (cm)
	Steam-carbon ratio	R_{SC}	PrOx	Length	L_{PrOx} (m)
PH_I	Length	L_{PHI} (m)		Diameter	D_{PrOx} (cm)
	Height	H_{PHI} (mm)	Cooling Air Flow Fraction	To HTSR	y_{HTSR}
	Channel No.	N_{PHI}		To HX_II	y_{HXII}
PH_II	Length	L_{PHII} (m)		To LTSR	y_{LTSR}
	Height	H_{PHII} (mm)		To PrOx	y_{PrOx}
	Channel No.	N_{PHII}	Natural Gas Flow Ratio	To SMR	y_{Fuel_SMR}
HX_I	Length	L_{HXI} (m)		To Combustor	y_{Fuel_comb}
	Height	H_{HXI} (mm)	HTSR	Reformate inlet temperature	T_{inlet} (K)
	Channel No.	N_{HXI}		Length	L_{HTSR} (m)
HX_II	Length	L_{HXII} (m)		Diameter	D_{HTSR} (cm)
	Height	H_{HXII} (mm)	HX_III	Length	L_{HXIII} (m)
	Channel No.	N_{HXII}		Height	H_{HXIII} (mm)
WRAS				Channel No.	N_{HXIII}
Motor	Torque	TQ_{motor} (Nm)	SG	Length	L_{SG} (m)
	Rpm	RPM_{motor}		Diameter (cm)	D_{SG} (cm)
Compressor	Pressure ratio	PR_{comp}		Tube No.	N_{SG}
	Mass flow rate	M_{comp} (kg/s*K$^{1/2}$)	**SS**		
Expander	Pressure ratio	PR_{exp}		Activity area	A_{cell} (cm×cm)
	Mass flow rate	M_{exp} (kg/s*K$^{1/2}$)		Cell No.	N_{cells}
				Operating pressure	P (bar)

5.7 Looped Optimization Strategy

In a typical energy system synthesis/process design, the system is developed (only sometimes involving mathematical optimization) at full load condition followed by the design of the control architecture of the system for dynamic operation. In a typical energy system dynamic synthesis/design process, design of the control architecture is done prior to the synthesis/design process, due to the fact that the system must be developed based on some representative dynamic load profiles and the system itself can not, of course, without controls perform the dynamic tracking of the profile. Therefore, the control effects on the dynamic development (in the present case, dynamic synthesis/design and operation) of the system need to be studied, since there are a number of questions which

need to be answered such as i) if the controllers affect the optimization results, ii) if the controllers need to be optimized during the optimization process and it so how this should be done, iii) etc.

This section outline a looped optimization strategy utilized to study the relation between the control architecture design and the dynamic synthesis/design and operation optimization of energy systems. Figure 5.8 shows a schematic of the looped optimization strategy applied to the WRAS, which although it is not as complex as the whole system is nonetheless still highly nonlinear and, thus, indicative of the issues at hand. As shown in Figure 5.8, the optimization loop consists of the following steps:

Step 1: Develop the state space based multi-input/multi-output (MIMO) control architecture for the WRAS as depicted schematically in Figures 4.10 and 4.11 of Chapter 4.

Step 2: Since the application of state space control techniques is limited to linear system, a linear representation of the highly non-linear model of the WRAS for an initial fixed synthesis/design (i.e. one with fixed synthesis/design and operation decision variable values) must be found. This is done using gPROMS^{TM} which has the capability of providing a linearized representation (state space representation) of even highly non-linear system at a given operating point.

Step 3: Transfer the linearized WRAS model to Matlab^{TM} and use the Matlab^{TM} control toolkit and the state space representation (linearized representation) of the WRAS to establish the control gains of the WRAS's state space based MIMO control architecture.

Step 4: Transfer the control gains back to the controllers in the non-linear gPROMS^{TM} model of the WRAS and test the behavior of the state space based MIMO controllers over the entire (48 hr) load profile to ensure proper behavior at all load conditions.

Step 5: If stability problems occur return to the Matlab environment in order to 'move' the poles for increased stability and recalculate the gains (Repeat Step 3). If there are no stability problems, proceed to step 6.

Step 6: In the gPROMS™ environment perform a dynamic synthesis/design and operation optimization of the WRAS over the entire load profile, using the particular state space based MIMO controllers established in Steps 3 to 5.

Step 7: Compare the optimal synthesis/design and operation decision variable values with the initial ones on which the controller designs established in Steps 2 to 5 are based. If they are different, repeat Steps 2 to 7. If they are the same within an acceptable tolerance, the looped optimization process is finished.

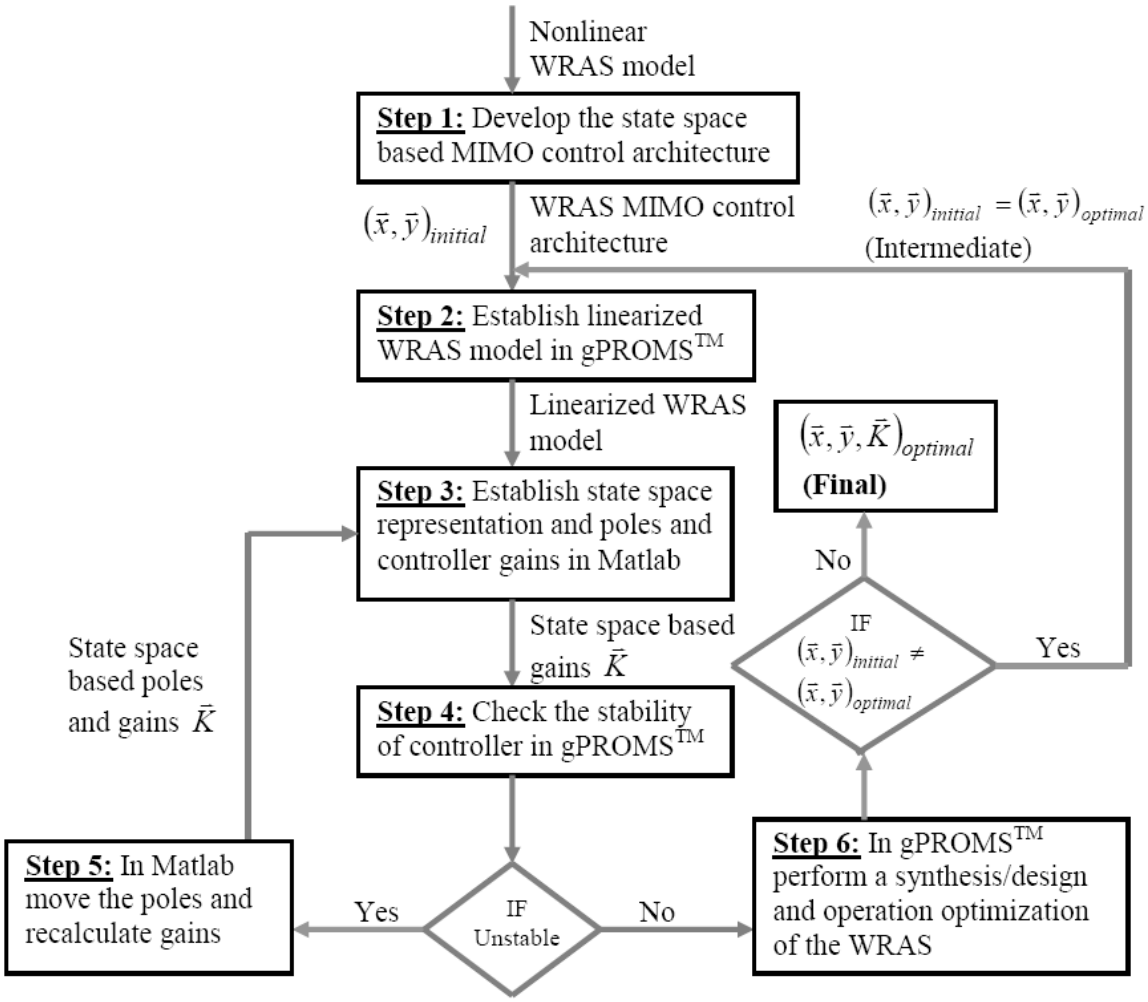

Figure 5.8 Schematic of the looped optimization strategy applied to the WRAS.

In this looped optimization strategy, the goal for control is to eventually find the optimal control architecture design consistent with the optimal synthesis/design and operation of the subsystem or system which must dynamically follow the load profile. In Step 6, the controller gains, $\bar{K}$, are not considered as decision variables. In each iteration of the looped optimization procedure at the end of which an optimal subsystem or system

synthesis/design, $\bar{x}_{optimal}$, and operation, $\bar{y}_{optimal}$, is found, a new control system architecture is found which allows the optimal subsystem or system to have the same response characteristics such as response time and overshoot as that of the synthesis/design with which the optimization of Step 6 began. Thus, since in this looped optimization the subsystems or systems synthesis/design and operation are optimized separately from the control, the procedure can be used to study the relation between optimal state space based control and dynamic synthesis/design and operation optimization.

Chapter 6

Results and Discussions

In this chapter, results of this doctoral work are presented consisting of simulation, control and optimization of the 5kW PEMFC system. First, results of the PEMFC system and subsystems simulation and dynamic responses at various conditions are presented. Then, to illustrate the control effect on the optimization, a looped optimization strategy is presented. In the looped optimization, the state space design method is used in the loop to help design controllers consistent with the optimal synthesis/design and operation of a given subsystem. The results are than compared to those resulting from the direct dynamic optimization of the controller designs in which the gains for the controllers are part of the decision variable set for the overall synthesis/design and operation optimization. The control effect on the optimization can be obtained from this looped optimization and its comparison to the overall optimization. Finally, results for the different optimization strategies utilized in this research are introduced. Comparisons are made between dynamic optimization and steady state optimization to illustrate the advantages of the dynamic optimization. The decomposition strategy, DILGO, is utilized for the overall system optimization. Also, the whole PEMFC system is optimized in a single-level optimization. These single-level optimization results are then compared with the results from the multi-level optimization technique, DILGO, and the results discussed.

6.1 Model Validation

The validations for several key component models of the proposed 5kW PEMFC system are presented in this section by comparing with the literature. The fuel cell voltage-current, power-current relations are always the most crucial characteristics in a fuel cell system. Figure 6.1 presents a comparison between the experimental results found

in Ceraolo, Miulli, and Pozio, 2002, and the fuel cell model simulation results produced here for steady state cell voltage and cell power density at different current densities. The comparisons show good agreements between the experimental data and the model simulations.

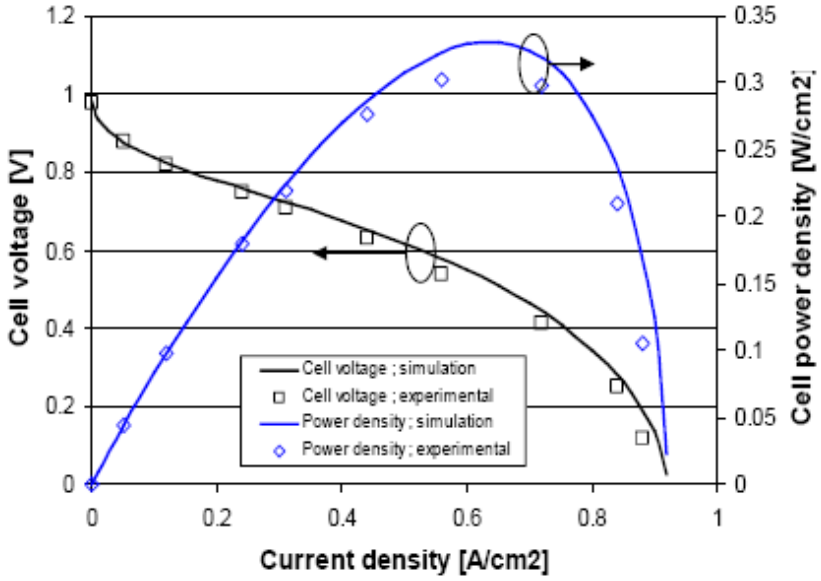

Figure 6.1 Comparison of simulated and measured cell voltage and cell power density at a cell temperature of 70°C and at inlet air flow rate of 1500 scc/min.

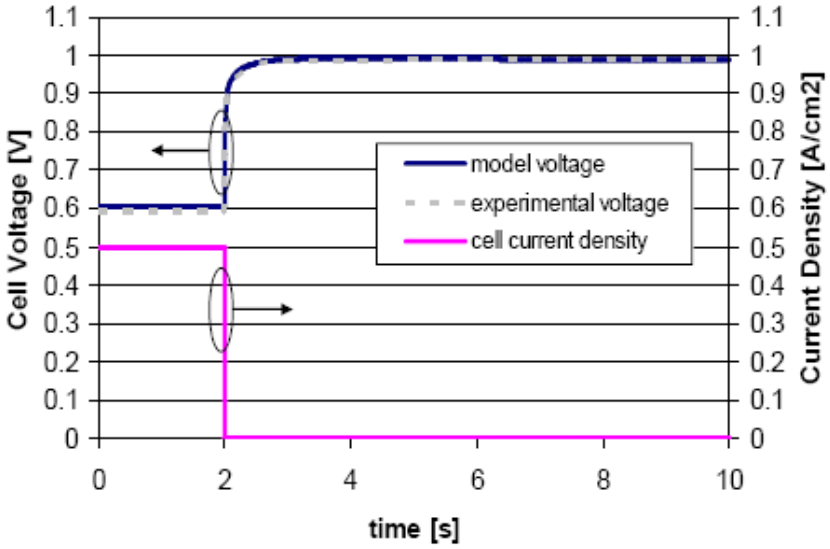

Figure 6.2 Comparison of experimental and simulated cell dynamic response at a cell temperature of 70°C; air and hydrogen pressures of 3 bar and 2 bar; an air and hydrogen flow rates of 1500 scc/min and 1400 scc/min, respectively.

With respect to fuel cell dynamics, Figure 6.2 shows a comparison of experimental and simulated cell voltage dynamic response to a sudden change in cell current density. The simulated cell voltage change has the same characteristics as the experimental results

(e.g., response time, magnitude, etc.). There is a small voltage overshoot in the cell voltage response to sudden current reduction, which can be observed more clearly in Figure 6.10 due to different vertical axis scales. This is due to the fact that the proton concentration near the cathode catalyst increases very fast as the cell current increases, while if the cell current decreases very fast the proton concentration decreases more slowly following the slow dynamics of the excess water removal from the cathode catalyst layer.

As to the FPS model validations, the kinetic equations (chemical reaction rate equations) used in each reactor are from published results (shown in Chapter 3) that are based on theoretical/experimental analyses and utilized broadly in a lot of applications. In the FPS, the major component for hydrogen generation is the SMR. Figure 6.3 presents the kinetics of SMR between the model produced in this study and the literature. The SMR model is simulated at the same steam-carbon ratio (3.0) as the reference. As seen in Figure 6.3, the model predicts well to the reference data, and also shows that the methane conversion increases as space time increases and finally reaches the equilibrium limit. Note, that the term "space time" is used in the chemical engineering literature to designate the ratio between the fuel flow rate and the reactor size, the latter of which is represented here by the weight of the catalyst, W_{cat}.

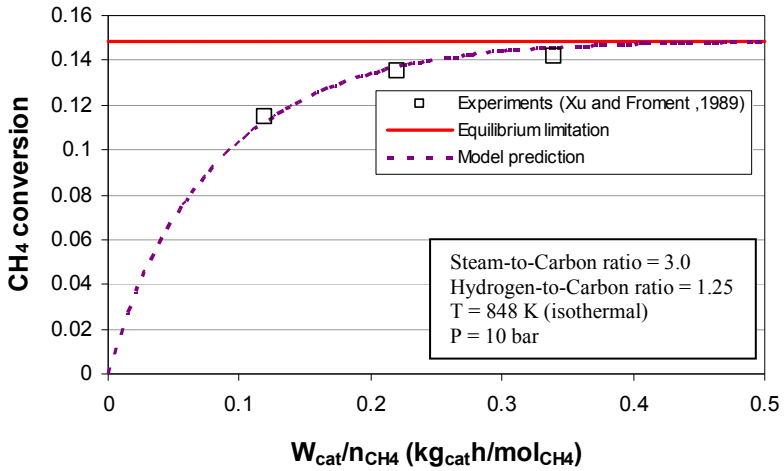

Figure 6.3 Comparison of SMR kinetics between simulation and literature (Kim, 2008).

In Figure 6.4, comparisons are made between the SMR model predictions for equilibrium and these found in Larminie and Dicks (2003). In this figure, the lines (marked with H_2, H_2O, CO, CO_2, and CH_4) represent the equilibrium concentrations of

steam reformation reactant gases as a function of temperature. The simulation results for the SMR model at equilibrium condition at different temperatures are shown as individual points. The simulation results are in good agreement with those found in the literature.

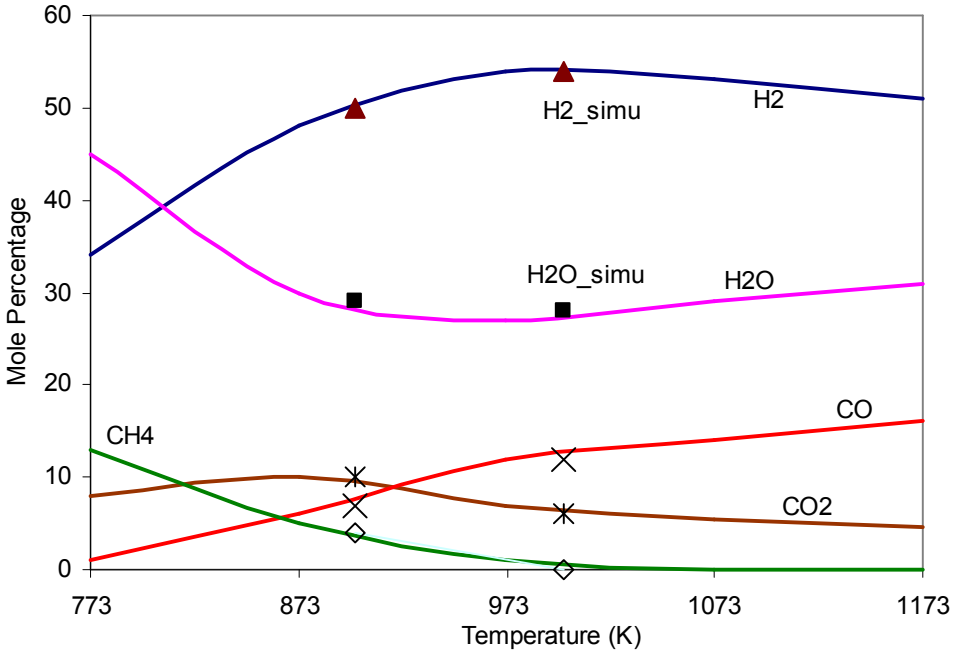

Figure 6.4 Comparison between simulated equilibrium concentrations in the SMR with values found in the literature.

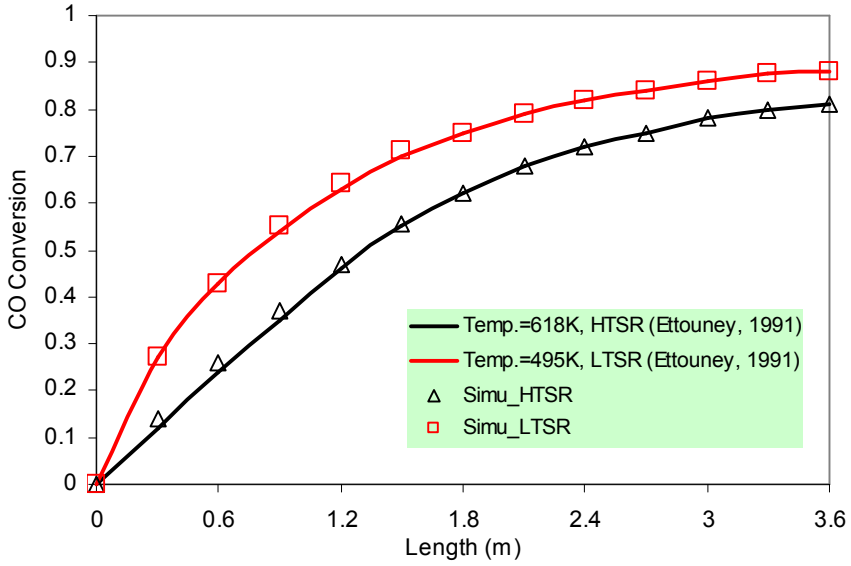

Figure 6.5 Comparisons of predicted CO conversions in the HTSR and LTSR.

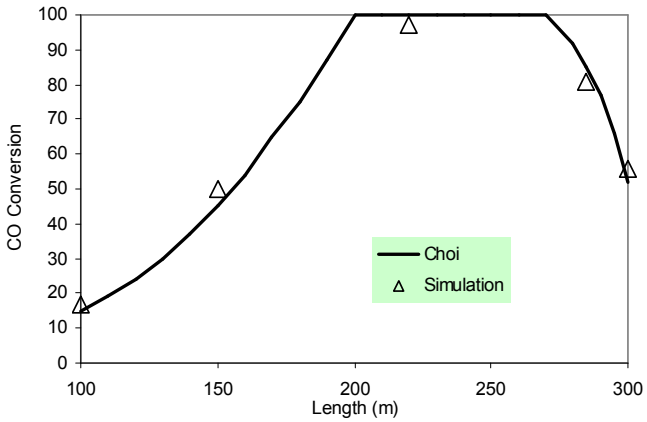

Figure 6.6 Comparison of predicted CO conversions in the PrOx at inlet conditions of 14% H_2O, 1% CO, and an O_2/CO ratio of 1.2.

The major objective of both the HTSR and LTSR is to reduce the CO concentration in the hydrogen rich fuel. It is very important to verify the CO conversion inside the reactors. Due to the reason that there is only one major reaction inside of these two reactors (i.e. the water-gas shift reaction), validation of the CO conversion also validates the conversion concentrations of all of the other constituents (e.g., a 1 mol reduction in CO causes a 1 mol increase in CO_2). Thus, if the predicted CO concentrations match those found in the literature then other constituent concentrations will be correct. Figure 6.5 shows comparisons between the predicted conversion of CO and the analytical/experimental results found in Ettouney (1991) for both the HTSR and LTSR. The comparisons show good agreement.

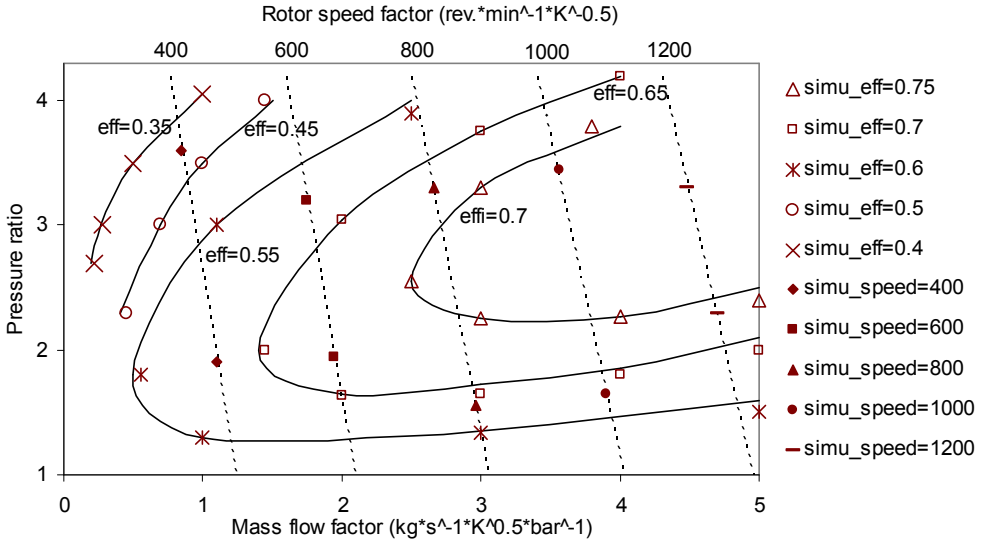

Figure 6.7 Comparison of compressor performance map between simulation and reference.

In the PrOx, extra air is fed into the flow mixture to burn the remaining CO. Figure 6.6 shows a comparison of the predicted CO conversions with the analytical/experimental results found in Choi (2004). The comparison shows good agreement.

In the WRAS, a compressor is utilized to supply air to the fuel cell stack at the required flow rate and pressure. The compressor map is simulated using the polynomial model equations given in Chapter 3. Different operating points representing compressor performance are generated by the compressor model and are plotted on the practical compressor performance map shown in Figure 6.7. The simulated speed lines fit the reference speed lines very well due to the fact that the speed lines are linear and easy to simulate. On the other hand, the efficiency lines are much more difficult to fit. Therefore, the simulated results have some difference with the reference, but nonetheless are still very close. The expander is also simulated using the polynomial model equations and the performance map is generated by running the model at different conditions. The results are plotted into the reference expander performance map shown in Figure 6.8. The simulated speed lines fit the reference speed lines very as well as the compressor map due to the linearity. And there is little error in the efficiency lines simulation. To verify the electrical motor model, the model is run at specific torques and speeds to calculate the motor efficiencies. Figure 6.9 shows the comparison between the electrical motor model simulation results and the motor reference performance map. Good agreements between the simulation and the reference at difference motor efficiencies are proved.

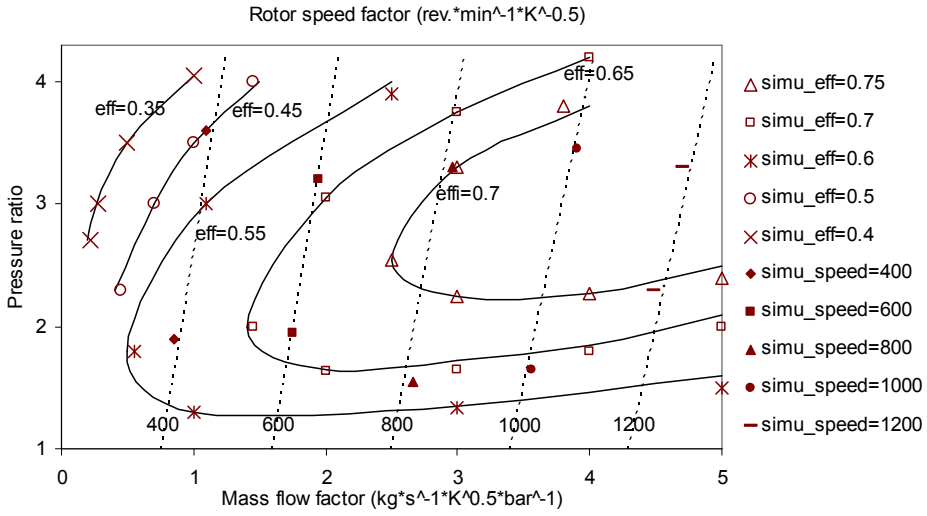

Figure 6.8 Comparison of expander performance map between simulation and reference.

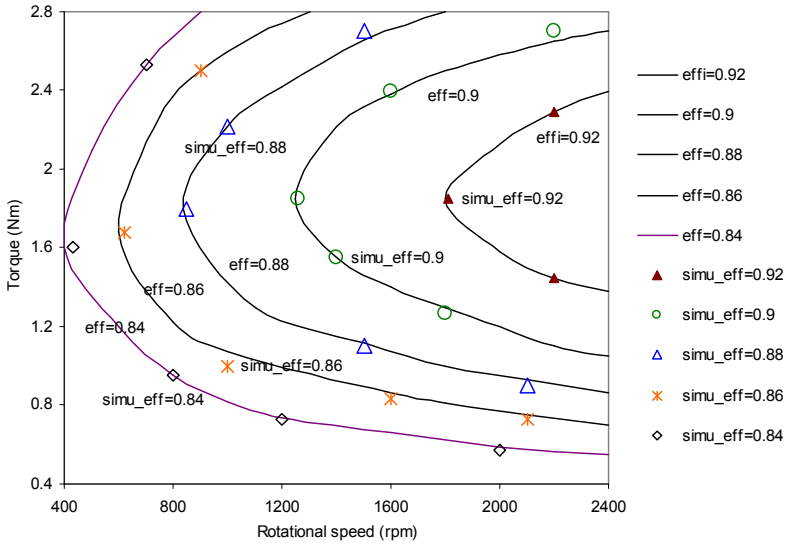

Figure 6.9 Comparison of motor performance map between simulation and reference.

6.2 Simulation Results and System Dynamic Response

6.2.1 The SS

This section presents the results of the model simulations and dynamic responses of the PEMFC system as well as its subsystems. The ultimate goal of a fuel cell system is to generate electrical energy. Thus, the most important relation in a fuel cell system is between the current and voltage. Figure 6.10 shows the dynamic response of the cell voltage to step changes (increase then decrease) in current density in the SS.

As expected, the voltage responds very fast to the current change due to the fact that electrical signals usually have very short response times. In this model, the proton concentration in the catalyst layer is assumed to be a function of the cell current since if the cell current rises, water production and hydration of the polymeric electrolyte near the cathode catalyst layer tend to rise as well, causing an increase in the number of mobile protons. This explains the voltage overshoot visible in Figure 6.10 due to the sudden drop in current density. When the current increases very fast, the proton concentration near the cathode catalyst layer increases very fast as well, while if the cell current decreases very fast, the proton concentration decreases more slowly following the slow dynamics of the excess water removal from the cathode catalyst layer.

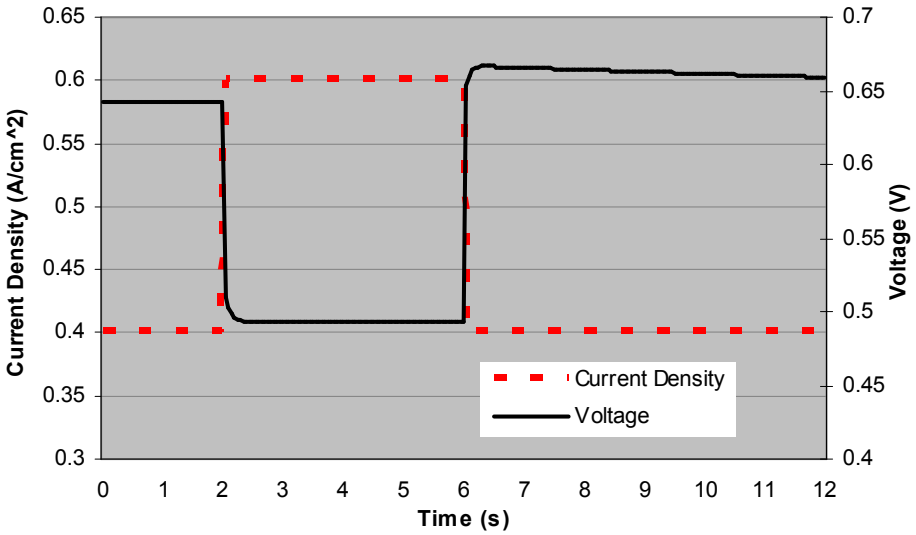

Figure 6.10 Cell voltage responses to sudden changes in current density.

In the SS, as the power requirement changes, both the cell current and voltage will change to meet the desired power output. The SS response to a power requirement step change (changes from 5kW to 4.5kW at 0.03s and changes from 4.5kW to 5kW at 0.09s) is shown in Figure 6.11. It illustrates how the cell voltage, current density and, therefore, the output power response to the sudden power requirement change. The output power response time is very short even with relatively slow responses in voltage and current. This result may lead to the conclusion that it is not necessary for the current and the voltage to respond too quickly as long as their combination gives the correct power. However, this is not correct. The reason that the current and the voltage response is slow is due to the small different which exists between the output power and the power requirements. For a single power density output of the fuel cell and with other conditions such as pressure and temperature fixed, there is only one combination between current and voltage (with only considering the power density range from zero to the maximum point). Before the current and voltage reach steady state, their combinations do not give the correct power required but nonetheless very close. In particular, in Figure 6.11, it is evident that there is a step change in the current signal as well as the power signal. This will make the output power of the fuel cell be very close to the power requirement, which will make the difference between them to be very small. This small difference or so-called, error, makes the controllers work ‘slowly’.

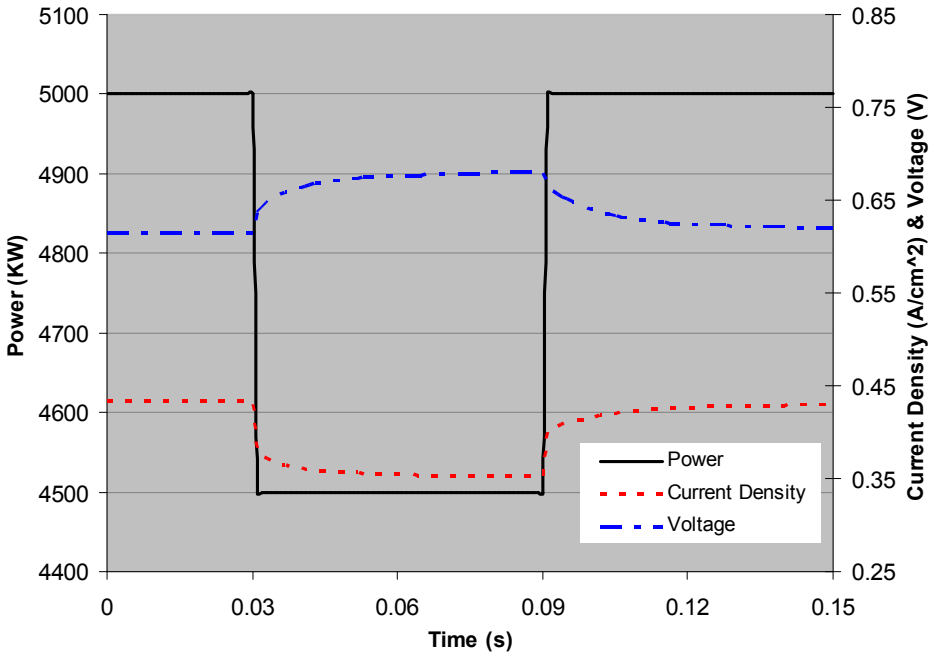

Figure 6.11 Response time of stack power, cell voltage and current density.

6.2.2 The FPS

In contrast to the SS (and the WRAS, for that matter), the FPS has orders of magnitude longer response times. This leads to difficulties in synthesizing/designing and operating/controlling the fuel cell system as a whole. In various PEM fuel cell applications with fuel reforming, batteries have to be used to meet the fast dynamic requirements before the FPS is able to catch up to the new power requirements which the system sees. In transportation applications, a fuel cell vehicle will use a hydrogen tank instead of an on board reformer, even this makes problems with too high pressure or too expensive materials. Figure 6.12 shows the simulated dynamic response of the hydrogen generation/flow rate of the proposed FPS to the hydrogen requirements. As shown in this figure, it takes the FPS around 100 seconds to meet the steady state condition, which is much slower than the SS and the WRAS.

The slow response of the FPS is due to the relative slowness of the chemical reactions and thermal responses in the reactors and heat exchangers. Figure 6.13 presents the dynamic responses of the hydrogen outlet flow rate, cooling air flow rate and methane flow rate (to the combustor) to the hydrogen requirement step change. At time equal to 100s, the hydrogen requirement changes in a step change from 0.0565 mol/s to 0.0476

mol/s as a result of a decreasing step power requirement from the SS. Therefore, the FPS needs less air to cool the reactors, less methane to the cathode, and less hydrogen to the SS. Thus, the temperature controller in the FPS changes the cooling air flow rate in order to keep the reactors at the desired temperatures. An overshoot of the air flow rate response can be seen in Figure 6.13. In this figure, the methane flow rate responses to the combustor also appears (note that it is multiplied by 10 in order to be able to present it on the same figure) and decreases without overshoot with decreasing hydrogen generation rate due to the reduced heat requirement. Due to the slow hydrogen flow rate response of the FPS, the FU of the fuel cell stack also changes from the desired operating value (85%) and reached back again, as shown in the up left corner in Figure 6.13.

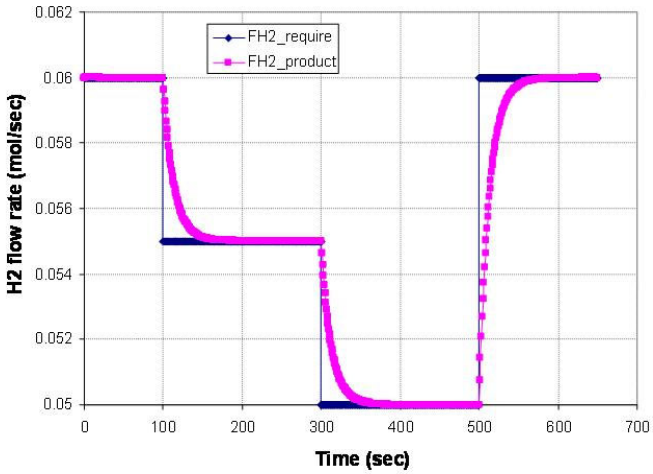

Figure 6.12 Hydrogen flow rate response of the FPS.

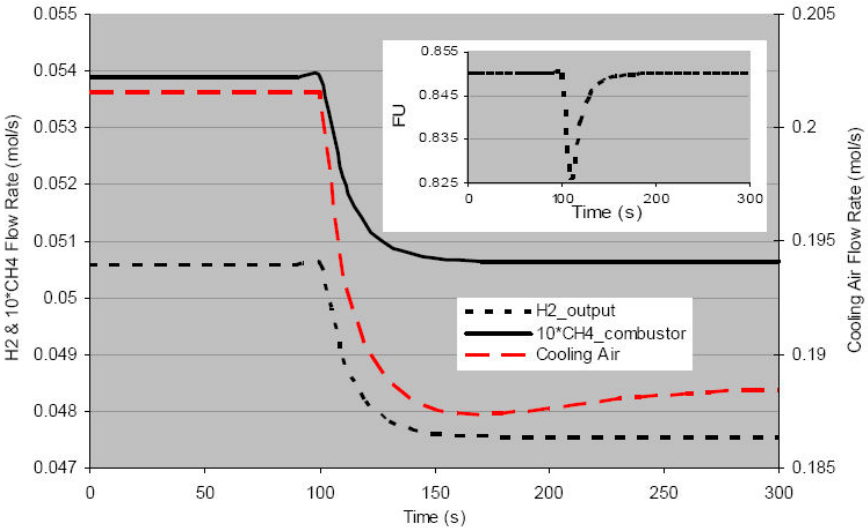

Figure 6.13 Dynamic responses of the hydrogen, cooling air, and methane (to the combustor) flow rates as a result of a step change in the hydrogen requirement (at time=100s) to the FPS.

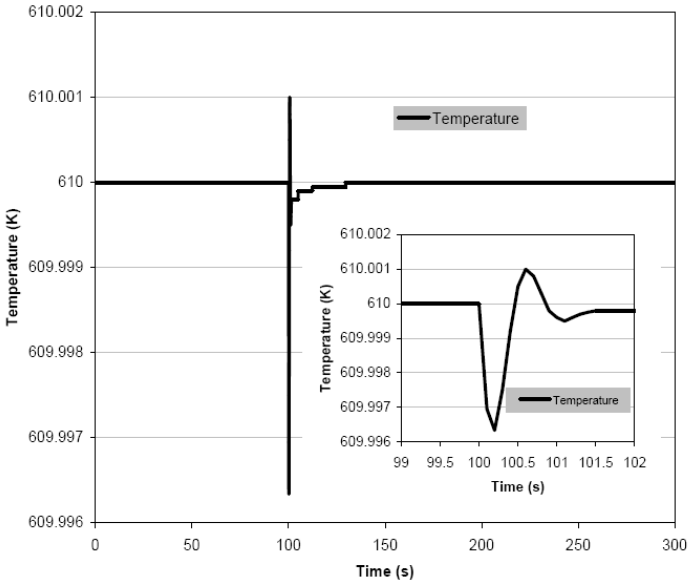

Figure 6.14 HTSR inlet fuel mix inlet temperature dynamic response to the power requirement change.

Figure 6.14 presents the variations in temperature at the control point due to changes in the cooling air flow rate. As indicated in Chapter 4, the fuel mixture temperature at the inlet of the HTSR is the one monitored and controlled (see Figure 4.12). As can be seen from Figure 6.14, the temperature controller works very well, only allowing the temperature to vary a little, almost negligibly, after the time the step change occurred. With this controller, the cooling air flow rate changes simultaneously with the hydrogen flow rate, as shown in Figure 6.13. The small figure (at the right-bottom corner) in Figure 6.14 presents the details of the temperature change.

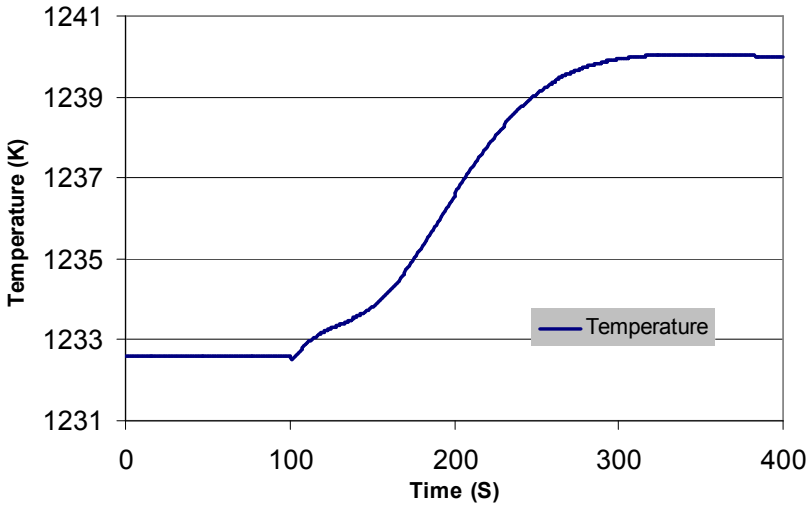

Figure 6.15 SMR fuel inlet temperature dynamic responses to the power requirement change.

Due to the fact that there is only one temperature monitored and controlled, the operating temperatures of all the reactors will have new values, when the system is operated at a new operating point, because the system is highly non-linear. Figure 6.15 shows the SMR inlet temperature changing with the same step change. Even when the control point temperature at the HTSR inlet is maintained constant, the SMR inlet temperature will change and require considerable time (in this case, for example, over 200 sec) to reach another steady state value after this step change.

For better understanding of the control architecture design, a number of comments on the results shown in Figure 6.13, 6.14, and 6.15 can be made. They are as follow:

1. In a complex system control architecture design, such as that proposed for the FPS with only a few points controlled, there is no guarantee that properties at other points in the system can also be kept constant during the dynamic operation with the controller. In most cases, their values will change to different ones at different operating points.
2. With only one or a few points which are monitored and controlled, variations in all the other variables across the entire load profile must be checked to ensure that they are still within acceptable ranges.
3. When more properties are controlled in a system, the whole system can be controlled better and in more detail. However, this increases the required equipment cost sometimes significantly in a real system in terms of measurement equipment, control equipment, etc.
4. The properties to be controlled, particularly when the number controlled is limited to only a few, need to be chosen intelligently based on system analysis and experiences to compromise the control quality and cost.

Figure 6.16 shows the 3D reformate temperature profile inside the SMR over the 48 hour load profile introduced in Chapter 4. With the HTSR inlet temperature as the controlled variable for the duration of system operation, the reformate temperature inside the SMR changes with location and time but still within a reasonable range. In fact, with the control architecture design developed for the FPS, the subsystem works well over the entire operating range of pressure, temperature, etc.

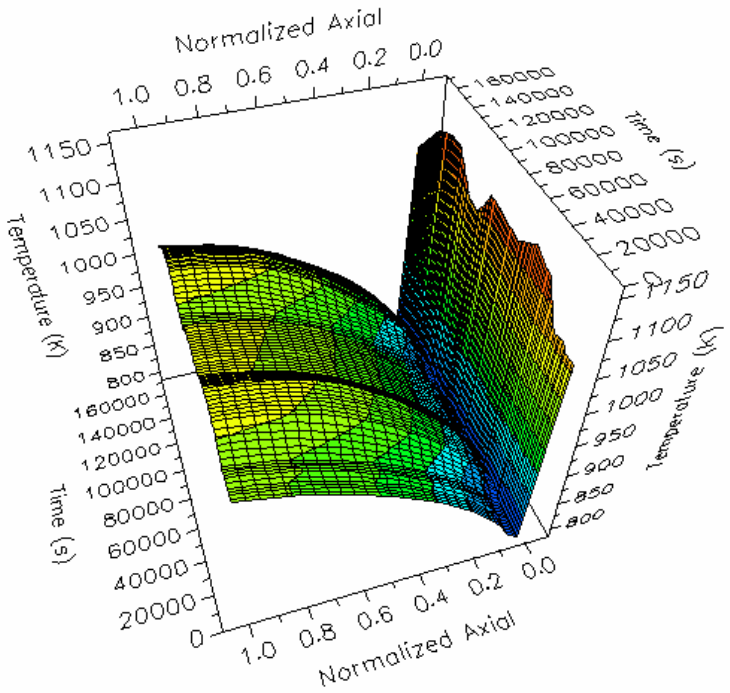

Figure 6.16 Reformate 3D temperature profile inside the SMR over the 48 hours of operation.

There are two major effects in any chemical reactor which change the temperature. One is the chemical reactions and the other the heat transfer. In the SMR, hot gas supply energy to the steam-methane mixture. The temperature of the steam-methane mixture will initially decrease due to the fact that the chemical reactions which are endothermic dominate in the inlet section. As the reactions approach equilibrium, their rates decrease and the heat transfer becomes more and more important. The mixture temperature, thus, keeps increasing in the rear section of the reactor as shown in Figure 6.16. Furthermore, at different times, the SMR inlet temperatures are different due to this variable is not directly controlled and the fact that the system is highly nonlinear. However, the variation is not large and is within a reasonable range (1050-1150 K).

Figure 6.17 presents the reformate temperature distributions inside the HTSR and the PrOx. As was the case with the SMR, these two temperature profiles are also determined by the exothermic chemical reactions and heat transfer present. Because the water-gas shift reaction is slightly exothermic in the HTSR and there is combustion inside the PrOx, the temperature of the reformate mixture increases at first and then decreases in the rear part of these reactors when the heat transfer becomes more and more dominant.

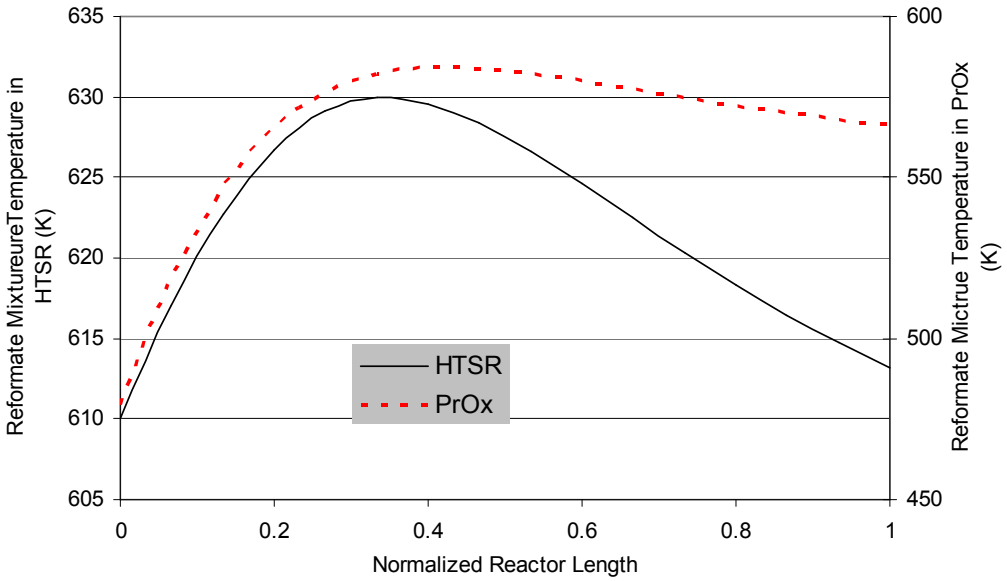

Figure 6.17 Reformate mixture temperature profile inside the HTSR and PrOx.

Figures 6.18 to 6.21 show the constituent mole fractions in each reactor as the fuel cell system is operated at full load and steady state. In particular, Figure 6.18 presents the changes in the CH_4, H_2, H_2O, CO_2 and CO mole fractions along the SMR length. The inlet steam-methane ratio is 3. As shown in the figure, both CO and CO_2 are generated together with hydrogen. Each of the CH_4, H_2 and H_2O mole fractions reach a relatively stable value (near equilibrium) in the middle of the reactor while the CO and CO_2 mole fractions keep changing in the latter half of the reactor. This is because of the chemical dynamics of the reactions inside the SMR, i.e. the rates of reaction between CH_4 and H_2O are relatively fast compared to the water-gas shift reaction. The reactor length is a design decision variable in the optimizations.

After the SMR, two water-gas shift reactors, the HTSR and LTSR are used to generate more hydrogen as well as reduce the CO. From the aspect of hydrogen generation, the water-gas shift reaction favors low temperature. Conversion of CO at low temperature is characterized by low energy consumption, high hydrogen yield, as well as reduced equipment cost. However, the catalysts used in CO conversion at low temperatures have a much lower resistance to poisoning and thermal stresses. Thus, a good solution is to utilize a HTSR to reduce the CO concentration first and then use a LTSR to draw the reaction in the direction of much lower CO concentration at equilibrium at low temperature. Figured 6.19 and 6.20 present the constituent mole

fractions along the HTSR and LTSR length. The mole fraction of hydrogen is given on the right-side vertical axis. As shown in these two figures, the CO mole fraction decreases in both reactors. In Figure 6.19, it is seen that the CO mole fraction reaches an equilibrium value at the relatively high temperature found in the HTSR. This equilibrium value changes in the LTSR and the mole fraction of CO is reduced further, as shown in Figure 6.20.

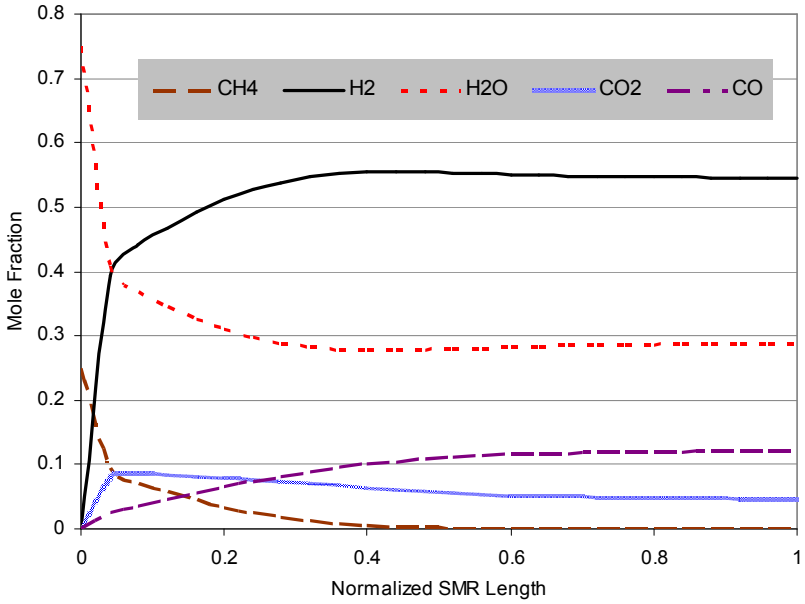

Figure 6.18 Constituent mole fractions along the normalized SMR length.

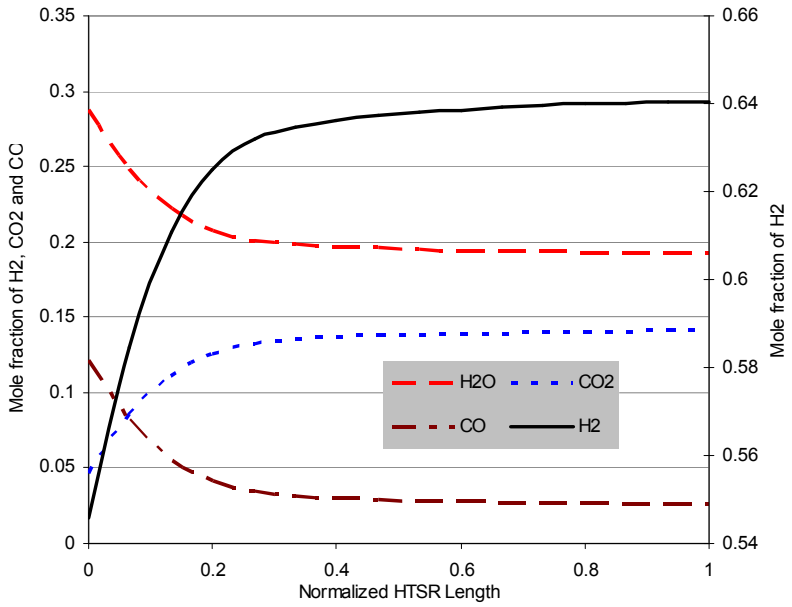

Figure 6.19 Constituent mole fractions along the normalized HTSR length.

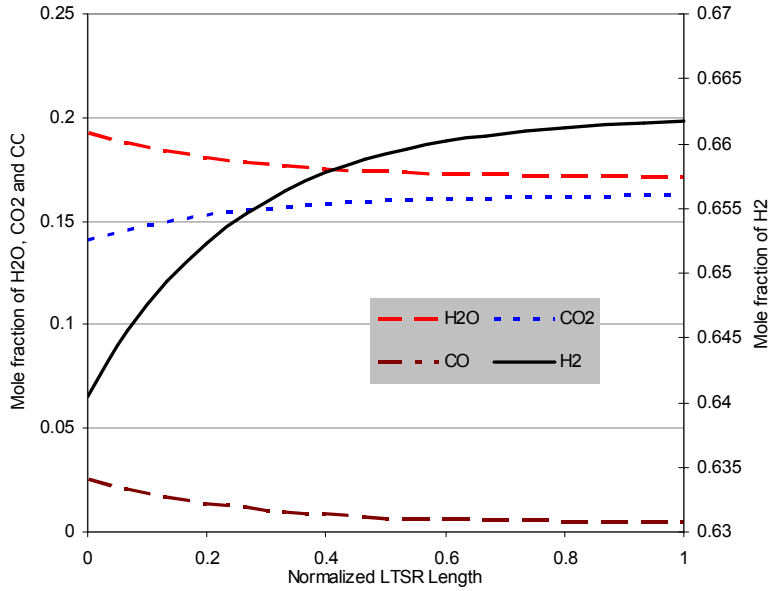

Figure 6.20 Constituent mole fractions along the normalized LTSR length

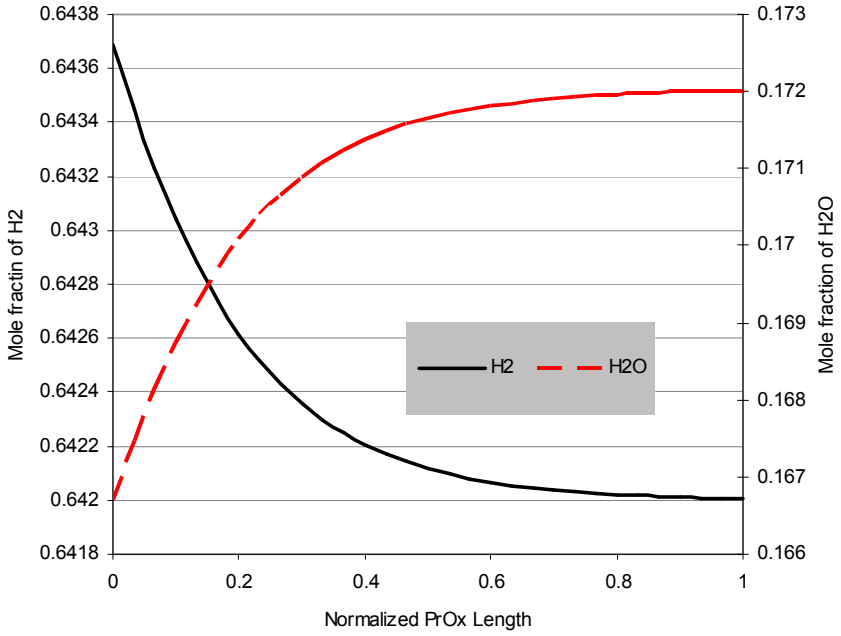

Figure 6.21a Constituent mole fractions along the normalized PrOx length.

Figure 6.21a and 6.21b present the mole fractions of H_2O, H_2 and CO, CO_2 respectively, inside the PrOx. As shown in these two figures, due to the combustion present, the mole fraction of CO and H_2 decrease and the concentration of CO_2 and H_2O increase. In fact, the PrOx must reduce the CO concentration below 10 PPM in order to avoid the possibility of poisoning the catalyst in the fuel cell stack. During the

optimizations of the FPS this concentration level is set as a constraint. Also note that from Figures 6.18 to 6.21, the outlet constituent mole fraction of each figure is the inlet mole fraction of the following figure. The only exception is the PrOx because extra air is injected into the PrOx in order to combust the CO.

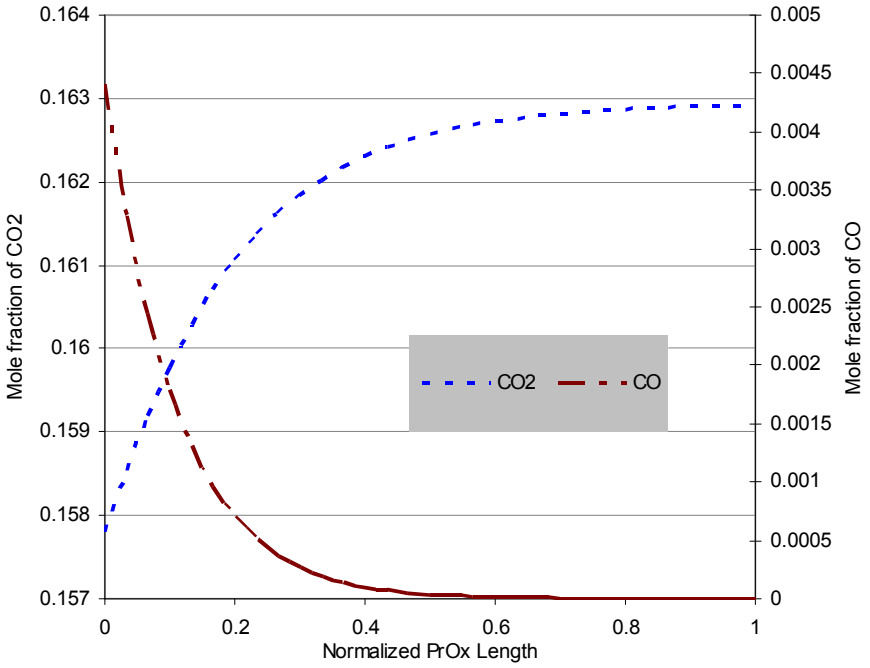

Figure 6.21b Constituent mole fractions along the normalized PrOx length.

6.2.3 The WRAS

Turning now to the WRAS, the control architecture of the WRAS needs to be able to control the air supply at a range of pressures and flow rates. Of course, these requirements must be within the operating ranges of the equipment. In the proposed WRAS, the pressure is controlled by a servo valve with a very short response time. The shaft speed of the compressor is controlled by an electrical motor which also is able to respond quickly to a dynamic load change. Figure 6.22 and 6.23 show the detailed transient responses of pressure and flow rate delivered by the WRAS. As can be seen in these figures, the dynamic responses of the WRAS are much shorter than those for the FPS. When requirements of both pressure and flow rate are changed, the WRAS can respond relatively quickly due to the control constructor inside the system.

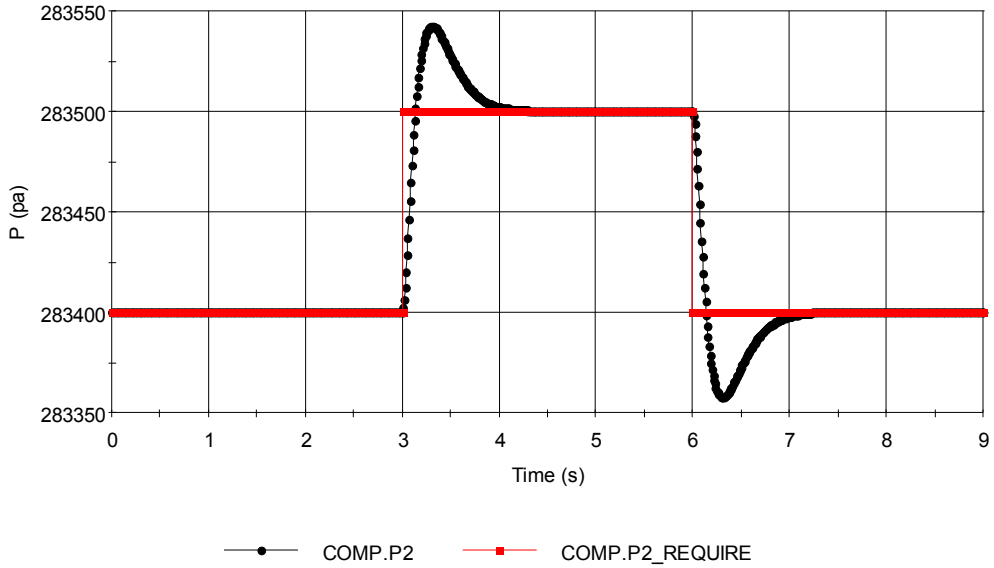

Figure 6.22 WRAS pressure responses to sudden changes in the pressure and flow rate requirements.

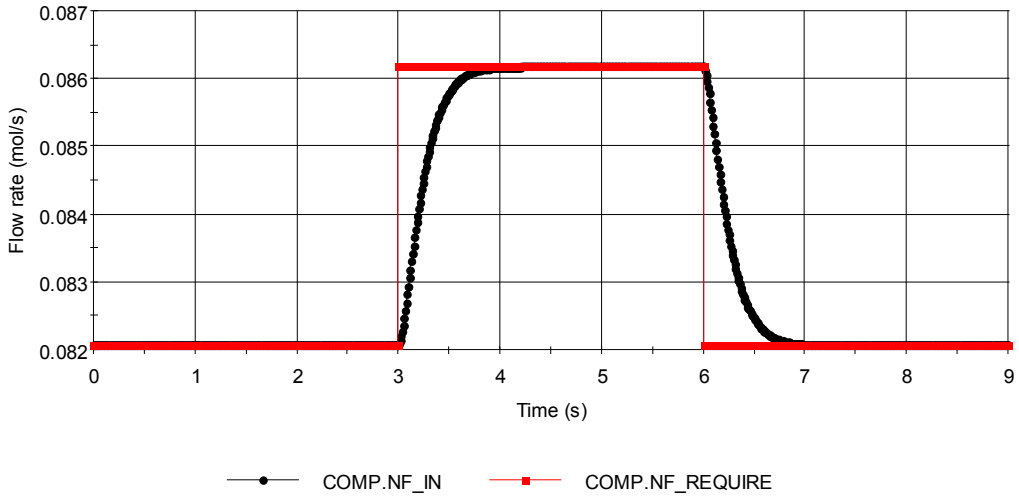

Figure 6.23 WRAS flow rate responses to sudden changes in the pressure and flow rate requirements

6.3 Control Effect on the Dynamic Optimization

The looped optimization strategy introduced in section 5.7 is applied to the WRAS, which although it is not as complex as the whole system is nonetheless still highly nonlinear. The looped optimization on the WRAS reaches an optimum solution, $\left(\bar{x}, \bar{y}, \bar{K}\right)_{optimal}$ (final), after four iterations as shown in Figure 6.24 (the first five bars). On the other hand, a more direct or non-looped optimization strategy, dynamic synthesis/design and operation/control optimization, is also applied on the WRAS in

which the gains of the controllers are part of the decision variable set for the overall optimization. In effect, Step 6 is performed with $\vec{x}$, $\vec{y}$ and $\vec{K}$ as decision variables so that looping back to Step 2 never occurs. The requirements of the dynamic responses, i.e. settling time and overshoot, are treated as constraints in the optimization. This optimization result is shown in the last bar in Figure 6.24. The final results from these two optimization approaches are shown to be almost identical.

The implication of Figure 6.24 is that the controller gains should be treated as decision variables simultaneously with those for synthesis/design and operation. Furthermore, the question can be asked as to why it takes the looped optimization several iterations to find the final optimal results. The reason is that in each iteration of this looped optimization where the controller design acts as a limitation/constraint on the optimization of the Step 6, the dynamic system is not stable for all the possible values of the synthesis/design and operation decision variables. Therefore, in each loop, the optimization is only able to find the optimum system or subsystem which can be controlled by the particular controllers in place. As shown in Figures 6.25 and 6.26, for step changes in both flow and pressure requirements, the dynamic responses, i.e. settling time and overshoot of the signals, are different between the optimal (final optimization results from looped optimization) and the original WRAS with which the looped optimization began.

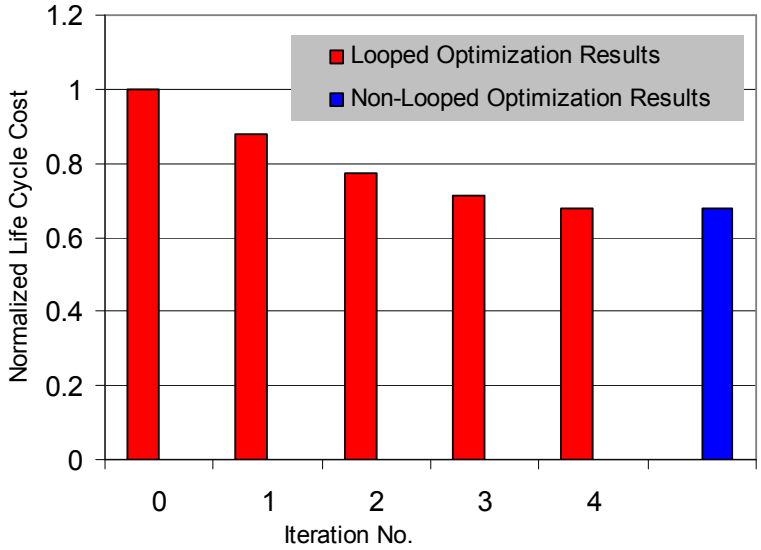

Figure 6.24 Results of looped and non-looped optimizations.

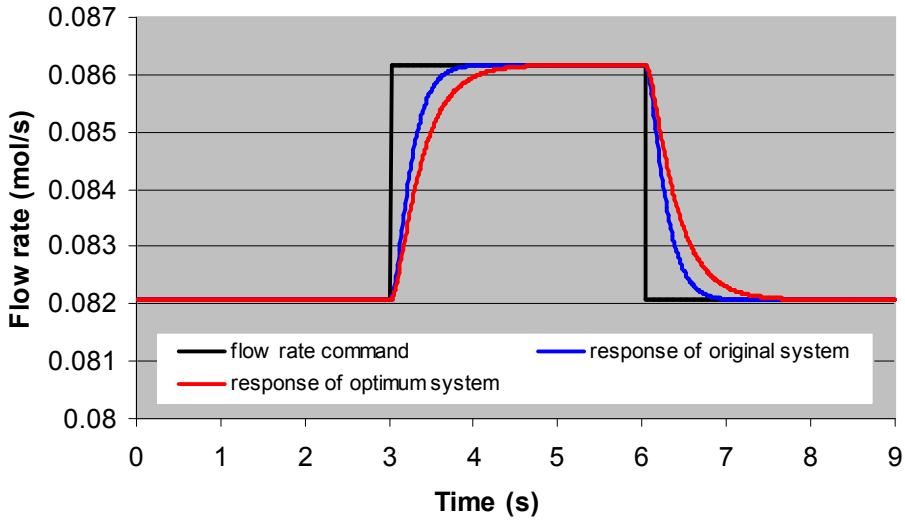

Figure 6.25 Comparison of the dynamic responses to step changes in the flow rate requirement between the original and the optimal WRAS.

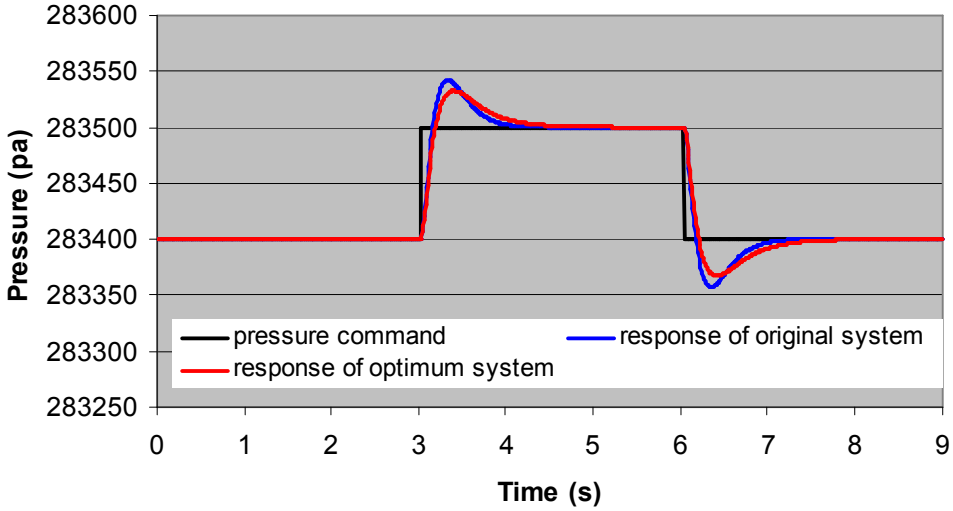

Figure 6.26 Comparison of the dynamic responses to step changes in the pressure requirement between the original and the optimal WRAS.

6.4 Development Procedure for the State Space Based MIMO Controllers

In this section, further discussion is given about the procedure for developing the control architecture design as applied in this doctoral work, using with the WRAS as an example. To design a state space based MIMO controller for a subsystem (e.g. WRAS) or system, linearization of the subsystem or system dynamic model is necessary. For the purposes of controlling the WRAS, two inputs are chosen, namely, motor voltage and servo valve current, while the two outputs chosen as control variables are the air flow rate

and outlet pressure (as shown in Chapter 4). As mentioned above, gPROMS™ has the capability of generating a linear representation (state space representation) of a nonlinear (even highly nonlinear) model at a giving operating condition based on selected input and output variables. As shown in the state space representation where $\vec{U}$ represents the inputs and $\vec{Y}$ the outputs, the gPROMS™ linearization determines the values of the matrixes A, B, C, and D to represent the WRAS.

$$\dot{\vec{X}} = A\vec{X} + B\vec{U} \quad 6.1$$

$$\vec{Y} = C\vec{X} + D\vec{U} \quad 6.2$$

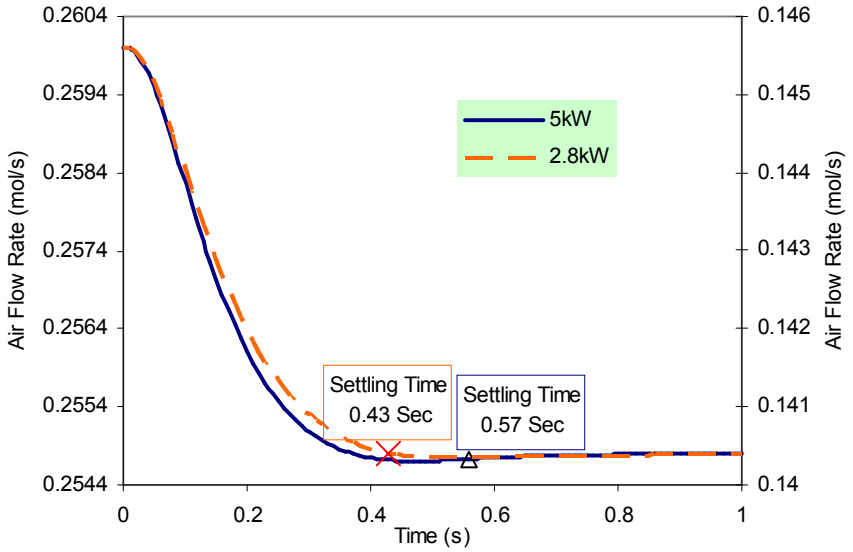

Figure 6.27 Dynamic responses of the WRAS at different operating points.

With the linearized model, Matlab is used to apply the control design analysis to the subsystem or system. Considering the WRAS control requirements, the two dominant poles for the close loop WRAS control system are placed at -10+10i and -10-10i (corresponds to 4.32% overshoot and 0.4 second settling time) to calculate the values of the controller gains, as shown in section 4.3.3. Other poles can be placed to anywhere to the left of these two poles. After this, the controller design determined in Matlab based on the linear model can be applied to the WRAS to control the nonlinear model in gPROMS™. Figure 6.27 shows the dynamic response of the nonlinear WRAS at different operating points to a step change with the controller designed (0.4 second settling time). Operated at the operating point for which the system was linearized (5 kW in this case), the WRAS shows the same response characteristics with the design, which

is around 0.4 second settling time. When the WRAS is operated at the other operating point (i.e. 2.8 kW in this case), the response characteristics are different from the design, which is 0.57 second settling time in this case. Because of the nonlinearity of the WRAS, different operating points generate different linearized models, which need different controllers to give the same dynamic response characteristics. As shown in the figure, the response characteristics (at 2.8 kW) are still acceptable for fuel cell operating requirements, and the final values of the controller gains are decided by the optimization.

6.5 Comparison between Dynamic and Steady State Optimizations

In this section, the dynamic synthesis/design and operation/control optimization results are compared with those for steady state optimization. The focus is on the FPS which is the most complex of all the subsystems.

In the dynamic optimization, the controller gains are treated as decision variables during the optimization together with the synthesis/design and operation decision variables such as pressure, temperature, geometries, etc. In the steady state optimization, the system is optimized at full load after which the control architecture is designed (the gains determined) to operate the optimum system obtained from the steady state optimization. The optimal steady state system with controllers is then operated under the same dynamic load profile used in the dynamic optimization in order to determine the life cycle cost. The life cycle costs of these two optimized systems can then be compared. The FPS in the PEMFC system is chosen for this comparative analysis due to its complexity and highly nonlinear behavior.

Figure 6.28 shows a comparison between the life cycle costs (including capital and operating costs) of the initial FPS with which the optimizations begin, the optimum FPS obtained from the dynamic optimization, and optimum FPS obtained from the steady state optimization. All three FPSs are operated using the same dynamic 48-hour load profile given at the end of Chapter 3. The dynamic and the steady state optimizations improve the life cycle costs by 19% and 6%, respectively over that of the initial FPS, with the dynamic optimization providing an improvement more that 3 times as great as that from the steady state optimization. It must also be emphasized here that the initial FPS was arrived at after a very lengthy process of modeling, simulation and analysis (no

optimization), so that for example, the 19% improvement afforded by the dynamic optimization is even more significant than indicated by the numbers. Figure 6.29 presents the analysis or optimization results for the lengths of the four reactors (SMR, HTSR, LTSR, and PrOx) obtained for the three different FPSs. The dynamic optimization yields smaller reactors than those for the steady state optimization due to the fact that the dynamic optimization considers the entire load profile during the optimization process resulting in a set of reactors that do not reduce system efficiency much but save on capital cost. Furthermore, even though the decrease in the sizes of the reactors for the optimized FPSs is dramatic, there is a less significant drop in life cycle costs due the fact that fuel or operating represents a large portion of these costs.

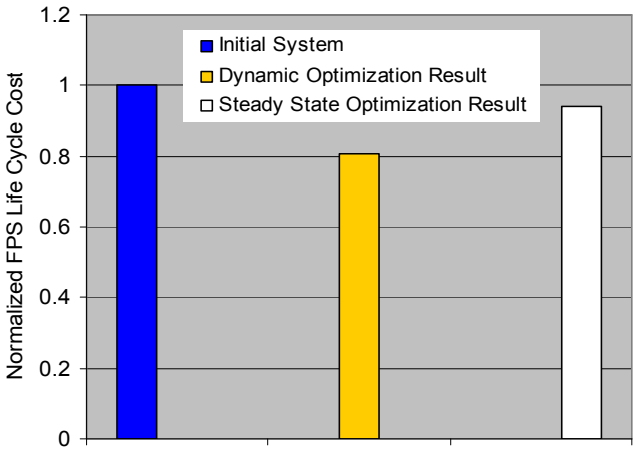

Figure 6.28 Life cycle cost results for the FPS dynamic and steady state optimizations.

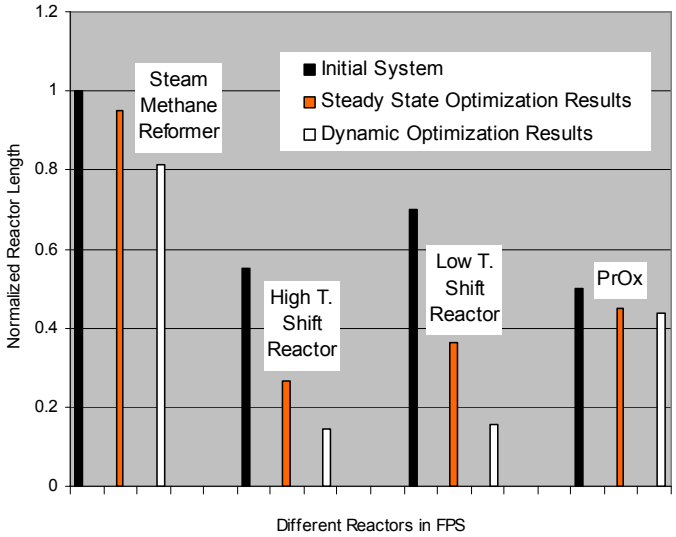

Figure 6.29 Reactor size comparisons between the three FPSs.

6.6 Dynamic Optimization with Decomposition Strategy

6.6.1 Optimal Results

Optimization is a very important tool for energy system synthesis/design and operation/control. In the case of large complex optimization problems, the practicality of finding solutions, computational time, and cultural factors of the work environment are all barriers which must be overcome. As discussed in Chapter 5, different types of decomposition strategies can be used to overcome these barriers by reducing the large, complex optimization problems, to separate one big optimization problem into several relatively smaller sized problems to solutions to which closely approximate those of the larger. In particular, the physical decomposition technique, DILGO, discussed in Chapter 5 is utilized here in order to solve the PEMFC system synthesis/design and operational/control optimization problem. Detailed information on subsystem decision variables, coupling functions, and objective functions are also presented in Chapter 5.

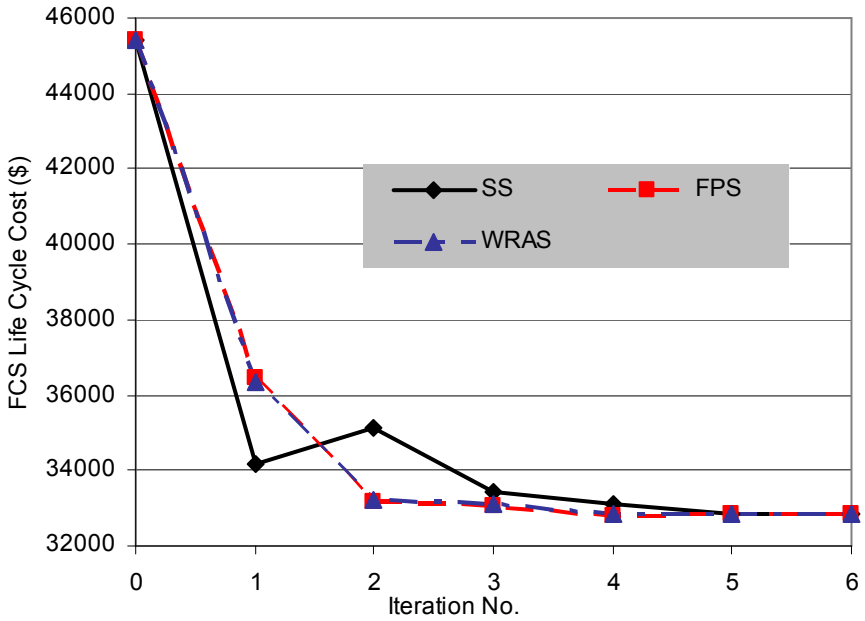

Figure 6.30 SS, FPS, and WRAS system-level, unit-based DILGO optimization results.

The solutions to the FPS, WRAS, and SS system-level, unit-based optimization problems in terms of FCS life cycle costs for each iteration of the DILGO approach are shown in Figure 6.30. In these system-level, unit-based optimizations, the objective function for each subsystem is the sum of the FCS life cycle cost and the integrals which

account for costs associated with the dynamic shadow prices and incremental changes in the coupling functions (details are given in Chapter 5). Thus, as is seen in Figure 6.30, the FCS life cycle cost need not be monotonically decreasing through out all the DILGO iterations as the SS. What must, on the other hand, occur is that all three system-level, unit-based objectives (one for each subsystem) must converge to the same optimal FCS life cycle cost. As can be seen in the figure, this occurs at the fifth DILGO iteration.

Table 6.1 Optimum costs of the PEMFC system and its subsystem for each iteration of the DILGO procedure.

DILGO Iteration No.	PEMFC ($)	SS ($)	FPS ($)	Natural Gas ($)	WRAS ($)	Percentage Improvement
0	45434.65	1556.07	4073.47	39035.57	769.52	---
1	36337.97	1733.17	3908.73	29870.84	825.21	20.02
2	33223.51	2663.57	3966.74	25692.18	901.00	8.57
3	33137.66	2856.14	3638.82	25692.18	951.27	0.26
4	32832.95	2856.14	3638.82	25392.88	945.08	0.92
5	32826.76	2856.14	3638.82	25387.47	945.08	0.02
6	32826.76	2856.14	3638.82	25387.47	945.08	0

The optimal PEMFC system life cycle costs, the capital costs of each subsystem, and the fuel cost are presented in Table 6.1. The PEMFC system life cycle costs are those based on the WRAS system-level, unit-based optimization. One reason is that the convergence speed of each subsystem is different. Thus, the FCS life cycle cost from different subsystem optimizations is different during the DILGO optimization procedure. Another reason is that in each iteration, the SS system-level, unit-based optimization problem is performed first, followed by that for the FPS and then that for the WRAS. In the SS optimization, the costs of the FPS and WRAS are from the last DILGO iteration. In the FPS optimization, the cost of the SS is from the same DILGO iteration while the cost of the WRAS is from last DILGO iteration. For the WRAS optimization, both the costs of the SS and FPS are from the same DILGO iteration. Therefore, in each DILGO iteration, the FCS life cycle costs from each subsystem are different as shown in Figure 6.30. Of course, whether or not one uses all the subsystem costs from the previous iteration as night be the case if the all the subsystem system-level, unit-based optimizations were done in parallel instead of in series matters not in terms of the final

convergence of the DILGO procedure since for any given subsystem optimization, the life cycle costs of the other subsystems remain constant.

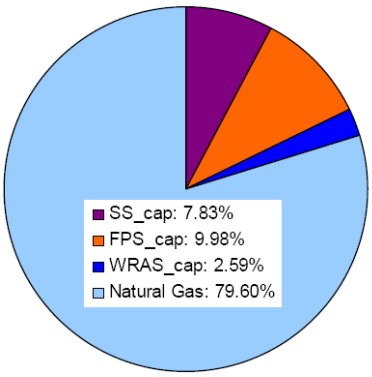

Figure 6.31 PEMFC system life cycle cost breakdown.

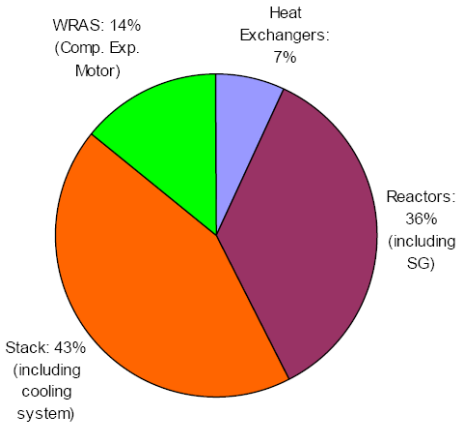

Figure 6.32 PEMFC system component capital cost breakdown.

As shown in Figure 6.30 and Table 6.1, the global optimum value for the life cycle cost of the PEMFC system is obtained in six iterations of DILGO where the zeroth DILGO iteration represents the cost of the initial system. Here again, it must be emphasized that the initial FCS was arrived at after a very lengthy process of modeling, simulation, and analysis (no optimization). As can be seen in the figure and table, some improvement is achieved in the system-level objective function in each DILGO iteration; and a significant improvement (28.57%) in the value of the system-level objective function is observed upon completion of the first two DILGO iterations. The relatively flat behavior of the FCS life cycle cost for the last three DILGO iterations indicates that the overall iterative optimization scheme is converged, i.e. no significant improvement is achieved after DILGO iteration 4. This observation is verified by running the problem until the sixth DILGO iteration with no observable change in the independent variables or the system-level objective function. The final optimal FCS life cycle cost is lower by $16,302 (US) than that of the initial FCS, which translates into a 29.79% decrease. The PEMFC system life cycle cost breakdown is shown in Figure 6.31, while Figure 6.32 presents the breakdown of PEMFC system component capital cost. The stack cost includes not only the costs of the fuel cell stack but those of the cooling cycle consisting of a fan, a radiator, and a pump. The costs of the reactors include not only the chemical reactors but the combustor and steam generator as well. The heat exchanger costs consist

of all the compact heat exchangers and mixtures in the FPS. The WRAS cost represents the costs of the compressor, expander, and the electrical motor.

Optimum results for the SS, FPS, and WRAS synthesis/design and operation/control decision variables appear in Tables 6.2a and 6.2b. The optimum PEMFC system configuration is shown in Figure 6.33. Comparing with the initial system (Figure 3.1), pre-heater I (PH_I) and heat exchanger III (HX_III) are eliminated from the system based on the system synthesis/design and operation/control optimization results shown in Table 6.2a. Figure 6.34 presents the optimal PEMFC system life cycle cost as a function of time.

Table 6.2a. FPS, WRAS, and SS optimum values for the synthesis/design and operation decision variables.

Subsystem	Component Variable	Optimal Value	Subsystem	Component Variable	Optimal Value
FPS			**FPS**		
SMR	L_{SMR} (m)	0.9	LTSR	L_{LTSR} (m)	0.5
	D_{SMR} (cm)	2		D_{LTSR} (cm)	9
	R_{SC}	3	PrOx	L_{PrOx} (m)	0.3
PH_I	L_{PHI} (m)	0		D_{PrOx} (cm)	7
	H_{PHI} (mm)	N/A	Cooling Air Flow Ratio	y_{HTSR}	0.2
	N_{PHI}	N/A		y_{HXII}	0.32
PH_II	L_{PHII} (m)	0.17		y_{LTSR}	0.12
	H_{PHII} (mm)	4		y_{PrOx}	0.35
	N_{PHII}	4	Natural Gas Flow Ratio	$y_{Fuel\ SMR}$	0.74
HX_I	L_{HXI} (m)	0.27		$y_{Fuel\ comb}$	0.26
	H_{HXI} (mm)	4	HTSR	T_{inlet} (K)	650
	N_{HXI}	4		L_{HTSR} (m)	0.45
HX_II	L_{HXII} (m)	0.25		D_{HTSR} (cm)	9
	H_{HXII} (mm)	4	HX_III	L_{HXIII} (m)	0
	N_{HXII}	3		H_{HXIII} (mm)	N/A
WRAS				N_{HXIII}	N/A
Motor	TQ_{motor} (Nm)	4	SG	L_{SG} (m)	1.2
	RPM_{motor}	4000		D_{SG} (cm)	0.6
Compressor	PR_{comp}	2.1		N_{SG}	10
	M_{comp} (kg/s*K$^{1/2}$)	0.17	**SS**		
Expander	PR_{exp}	2		A_{cell} (cm×cm)	28×28
	M_{exp} (kg/s*K$^{1/2}$)	0.16		N_{cells}	42
				P (bar)	2.2

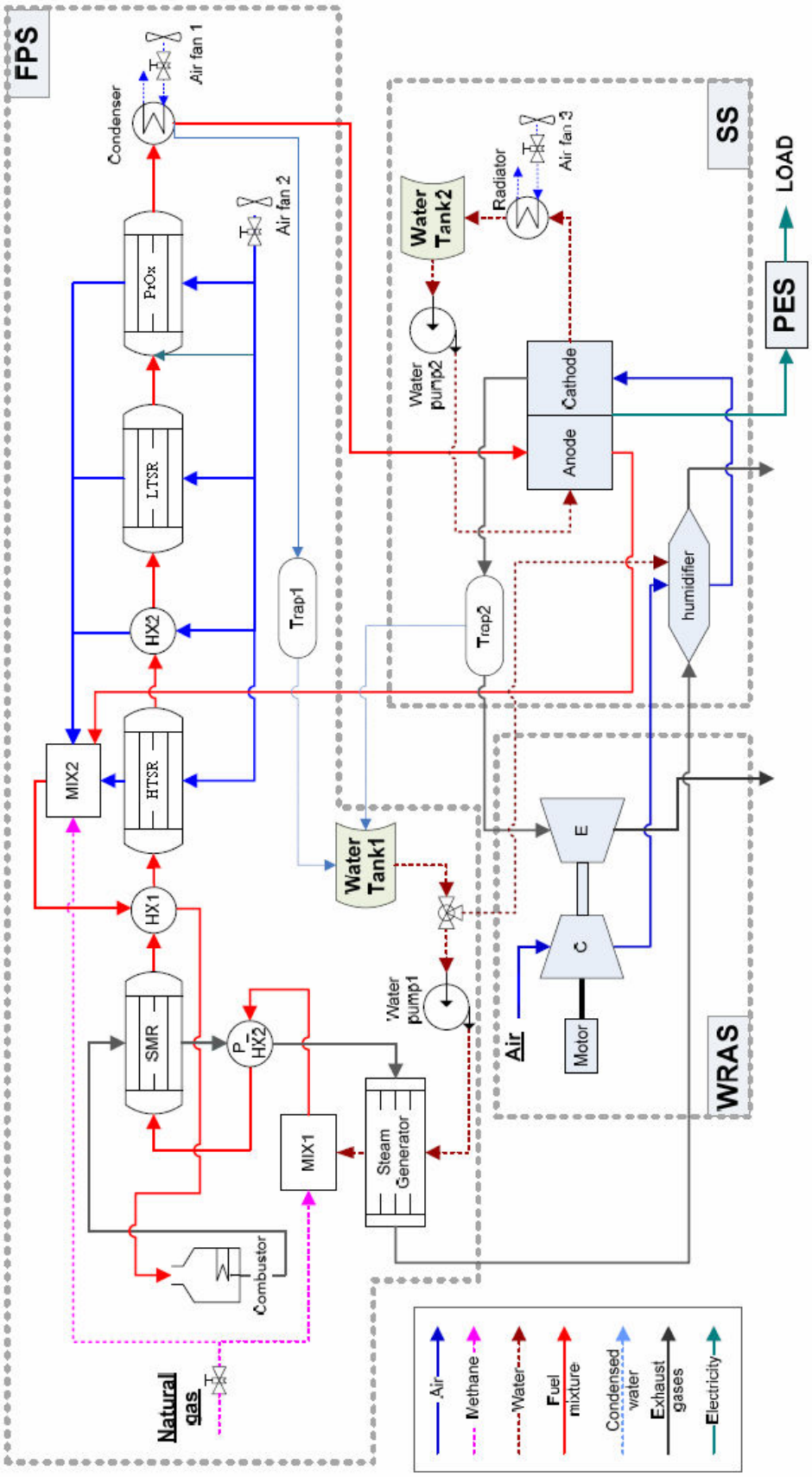

Figure 6.33 Optimum configuration of the PEMFC system.

Table 6.2b. FPS, WRAS, and SS optimum values for the control decision variables.

Controllers					
SS			**SS**		
Current Controller Gains	*K(1)*	3.35e11	Fuel Utilization Controller Gains	*K(7)*	2.89e10
	K(2)	-1.62e15		*K(8)*	-1.62e14
	K(3)	8.65e4		*K(9)*	5.47e3
	K(4)	405.3		*K(10)*	31.0
	K(5)	-300.8		*K(11)*	-25.9
	K(6)	392.4		*K(12)*	33.0
WRAS			**FPS**		
Cooling Air Flow Rate Controller Gains	*K_c(1)*	4.87e3	Reformate Temperature Controller Gains	*Kc(1)*	-0.013
	K_c(2)	-0.27		*Kc(2)*	1.2e-7
	K_c(3)	0.54		*Kc(3)*	7.68e-6
	K_c(4)	-30.8		*Kc(4)*	5.66e-7
PEMFC Operating Pressure Controller Gains	*K_c(5)*	0.0116	Methane Inlet Flow Rate Controller Gains	*Kc(5)*	0.02
	K_c(6)	1.02e-5		*Kc(6)*	4.8e-11
	K_c(7)	-2.2e-6		*Kc(7)*	1.56e-4
	K_c(8)	-0.01		*Kc(8)*	2.89e-11

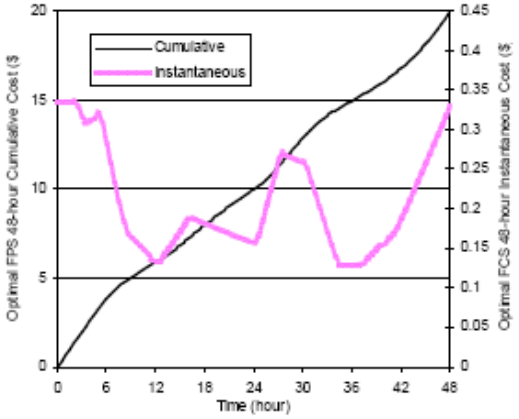

Figure 6.34a Optimal PEMFC system two operating costs as a function of time.

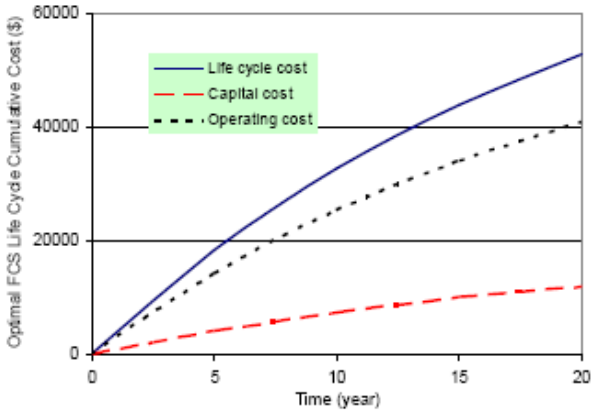

Figure 6.34b Optimal PEMFC system life cycle cost as a function of time.

As shown in Chapter 3, the representative load profile applied for system simulation and optimization is a 48 hours residential load profile, which has been repeated to generate the 10 years load profile (repeated 1650 times with 330 days per year and 10 years of operation). Figure 6.34a shows both the instantaneous and cumulative operating cost over the 48-hour period while Figure 6.34b shows the cumulative life cycle costs for

each year over the life time of the system. The initial value in Figure 6.34b represents the capital cost of the optimal PEMFC system. One thing need to be emphasized is that the cumulative cost in Figure 6.34b is not linear (it only looks like linear because the scale of horizontal axis is large).

6.6.2 System Trade offs

The PEMFC system life cycle cost shown in Figure 6.30 consists of four components: the capital costs of the three subsystems, the SS, FPS, and WRAS, and the life cycle fuel consumption cost. The changes of these four costs during the DILGO procedure are presented in Figure 6.35.

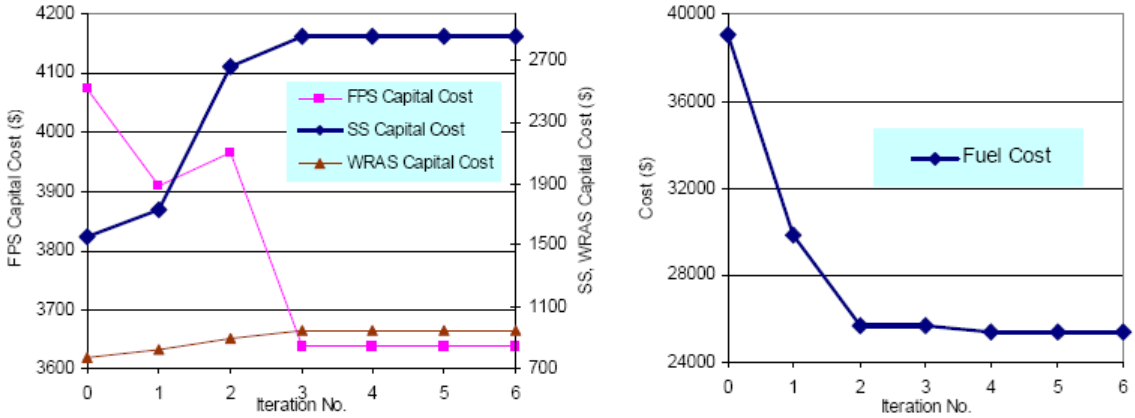

Figure 6.35 Changing the SS, FPS, and WRAS capital costs and fuel cost in each DILGO iteration.

As seen from this figure, the major part of the PEMFC system life cycle cost is the fuel consumption, which has a tremendous reduction during the optimization. Each subsystem optimization trades off capital cost versus subsystem efficiency. Generally speaking, larger components tend towards better performance and, therefore, higher efficiencies, but also higher capital costs. However, the operating condition is also a very important factor. A big compressor cannot deliver high efficiency with very low compressed flow rates. In the WRAS design, the proper sizes of compressor and expander balancing these competing factors need to be determined by the optimization. In case of the FPS, which has chemical reactors as its major components, the efficiency is not affected as much by size/length as long as the chemical reactions approach equilibrium. That is the reason that the FPS capital cost decreases for all DILGO iterations but one. The SS and WRAS system costs, on the other hand, have determined

by both the efficiencies and capital costs. For example, as seen in the figure, during the system optimization, the stack size increases and thus, its capital cost because the bigger sized stack increases the stack efficiency and, therefore, saves on fuel. Why this is is discussed next.

The relationship between fuel cell stack size, the fuel cell efficiency, and fuel cell stack capital cost are shown in Figure 6.36 for a given electrical power output. In the PEMFC stack model, the width and height of every single cell are the same (square, e.g., 20 cm×20 cm) another size factor is the thickness of each cell. In Figure 6.36, the axis of cell size represents the width/height of each cell. The efficiency of the fuel cell stack is the ratio between the net output electrical power and the lower heating value of the hydrogen consumption, i.e.

$$\eta_{SS} = \frac{\dot{E}_{SS\_total} - \dot{E}_{SS\_cooling}}{\dot{m}_{H_2 consumption} LHV_{H_2}} \tag{6.3}$$

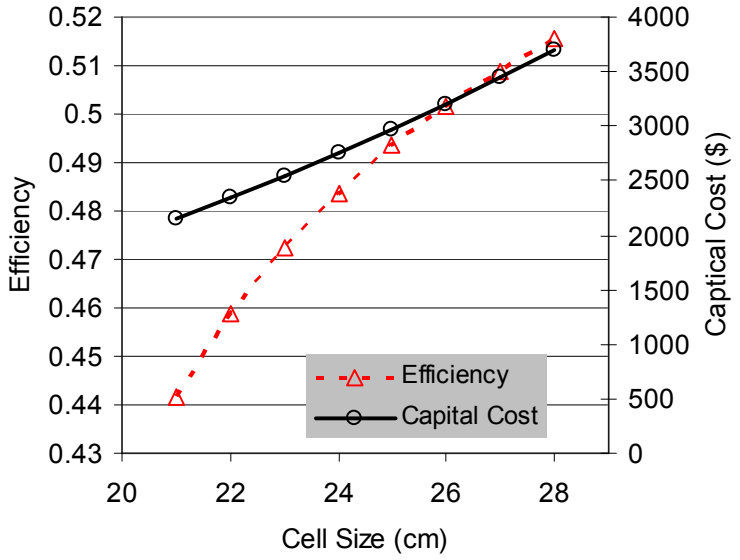

Figure 6.36 Relationship between fuel cell stack size, fuel cell efficiency, and fuel cell capital cost.

In Figure 6.36, the number of cells in the stack is constant (42 cells), and the capital cost is, therefore, only affected by the size of each cell. Other operating variables such as pressure and temperature are maintained at constant values (2.2 bars and 80^{o}C respectively). As shown in the figure, with increasing stack size, the fuel cell efficiency increases which reduces the operational cost, while the fuel cell capital cost also

increases. In fact, the fuel cell stack efficiency increases with increasing size due to the fact that it can operate at lower and lower current densities. However, large sizes also present a number of difficulties such as those related to fuel delivery (e.g., increased pumping costs and uniform flow distribution) and stack cooling (e.g., due to more complex temperature distributions). Therefore, there is some optimum compromise in terms of size with regards to both stack efficiency and capital cost.

Figure 6.37 makes evident why the fuel cell stack efficiency increases with increasing size. With increasing cell size, the fuel cell current density drops due to the increasing active area. This in turn produces an increase in cell voltage determined, of course, by the characteristic of the fuel cell. Thus, to produce the same amount of power, the total current requirement of the fuel cell is reduced. Therefore, less hydrogen is consumed to generate the same power. In fact, the higher the voltage is the higher the efficiency since voltage losses in the fuel cell stack due irreversibility decrease with decreasing current density.

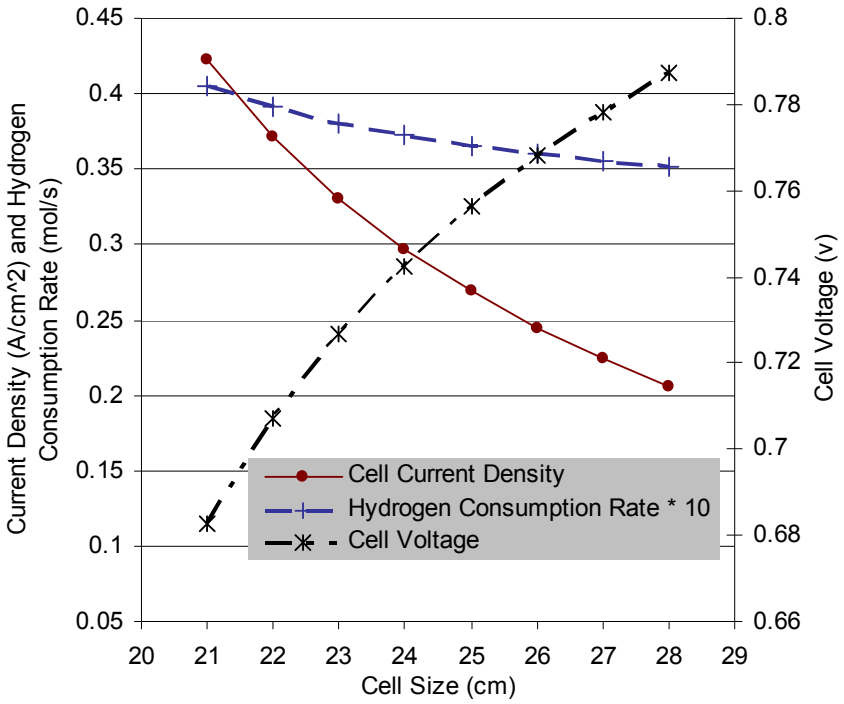

Figure 6.37 Relationship between fuel cell stack size and fuel cell voltage, current density, and hydrogen consumption rate.

As to the effects of reactor sizes on FPS efficiency and capital costs, Figure 6.38 presents the hydrogen ratio (the fraction of hydrogen in the reformate stream) change

inside the four reactors (SMR, HTSR, LTSR, and PrOx) based on the optimum lengths given in Table 6.2. The reaction rates at the beginning part of the reactors are much faster then those at the rear of the reactors, where the reactions are close to equilibrium. Because the fuel costs represent more than three fourth of the system life cycle cost, the optimum FPS attempts to allow the chemical reactions to reach equilibrium in order to save fuel. However, as the lengths increase, the gains in fuel economy per unit length decrease due to reductions in reaction rates. As shown in the figures, at the end of the optimum reactor length, the reactions approach but do not quite reach equilibrium. Thus, the trade-off in terms of size, efficiency and capital cost is such in the FPS that generally with the exception of a single DILGO iteration, the size of the FPS decreases in order to find the best compromise between efficiency and capital cost.

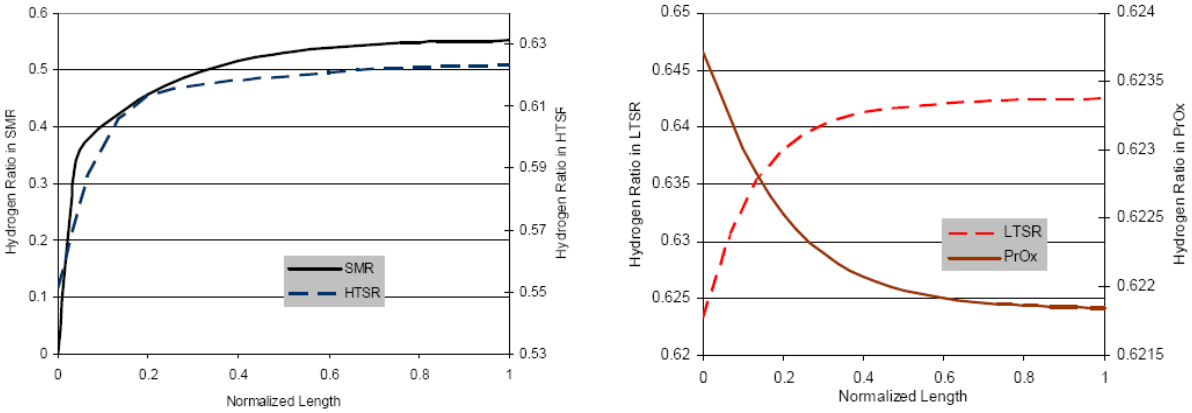

Figure 6.38 Hydrogen ratio change inside the optimum FPS reactors, SMR, HTSR, LTSR, and PrOx.

6.6.3 Dynamic Shadow Price Rates

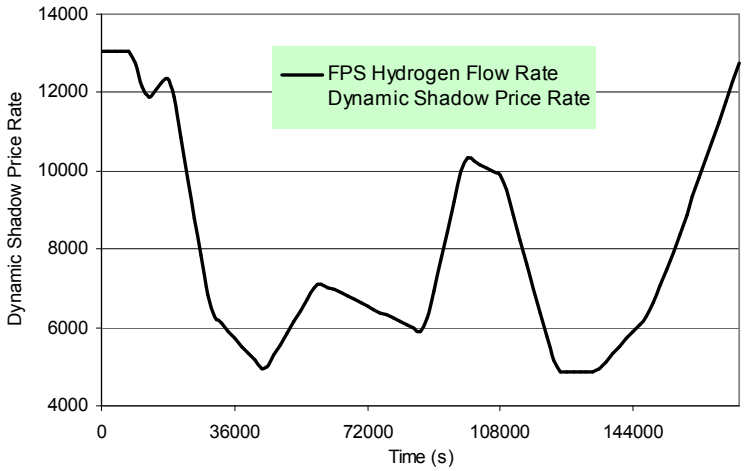

Figure 6.39 FPS hydrogen flow rate dynamic shadow price rate profile for the last DILGO iteration.

Figure 6.39 shows the FPS hydrogen flow rate dynamic shadow price rate through the operational profile. It can be seen that the effect of hydrogen flow rate on the FPS cost rate is a function of the operational point of the system, i.e. the higher the operating power, the higher the hydrogen flow rate effect on the FPS cost rate.

6.6.4 Comparison with Single-Level Optimization

For the purpose of comparison and validation of the multi-level optimization, a single-level approach is also used to optimize the entire PEMFC system, i.e. all of the subsystems simultaneously. This single-level optimization is a dynamic synthesis/design and operation/control optimization, using the system control architecture given in Chapter 4.

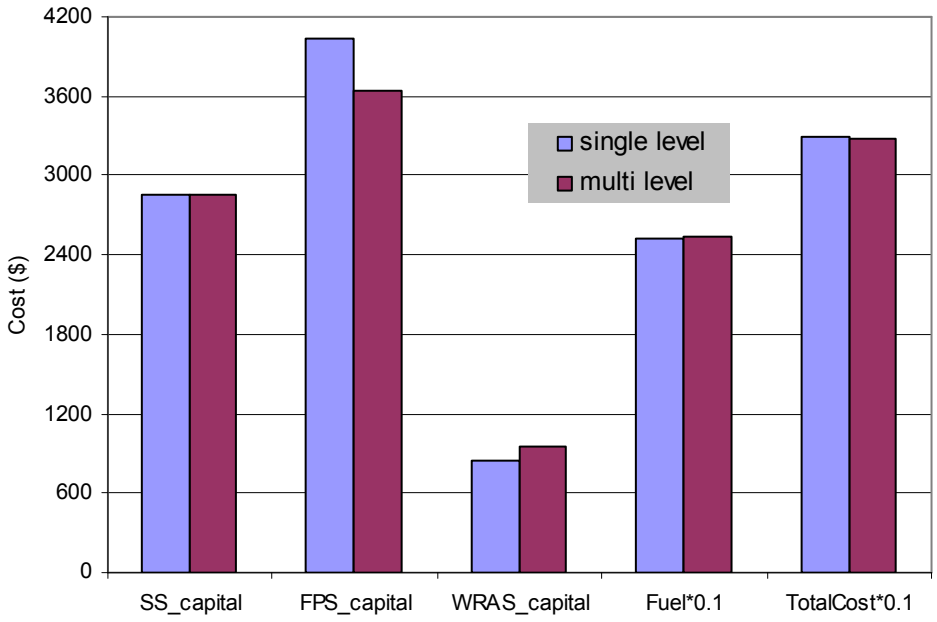

Figure 6.40 Comparison between the single-level and multi-level optimizations.

Figure 6.40 presents the comparison between the single-level and multi-level optimization results based on life cycle cost. In the multi-level optimization, each subsystem system level, unit based optimization considers only those decision variables local of itself (see Table 6.2) and the coupling functions between subsystems (see Table 5.1). In the single-level optimization, all these decision variables and coupling functions are considered together at once during the optimization. Figure 6.40 compares the capital costs of three subsystems, the fuel costs, and the system life cycle costs. Note that the

fuel cost and system life cycle costs are multiplied by 0.1 in order to show them on the same figure with the other costs. The results show very good agreement between the single-level optimization approach and the multi-level one using DILGO. This leads practical credence to the validity of using the DILGO decomposition strategy for multi-level optimization, something which has already been validated both theoretically and practically in Munoz (2001), Rancruel (2005), and Georgopoulos (2002) previously.

6.7 System Efficiency

Equations (6.4) to (6.7) are the definitions of the FPS, WRAS, SS and PEMFC system efficiencies/effectiveness with schematically explanations in Figures 6.41 to 6.44.

$$\eta_{FPS} = \frac{\dot{m}_{H_2} LHV_{H_2}}{\left(\dot{m}_{CH_4} LHV_{CH_4}\right)_{toSMR} + \left(\dot{m}_{CH_4} LHV_{CH_4}\right)_{toComb} + \left(\dot{m}_{H_2} LHV_{H_2}\right)_{toComb}} \tag{6.4}$$

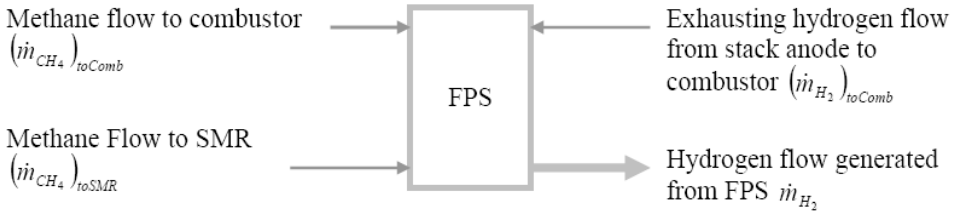

Figure 6.41 Schematically explanation of FPS efficiency definition.

$$\eta_{WRAS} = \eta_{comp} \frac{\dot{W}_{comp}}{\dot{E}_{motor}} \tag{6.5}$$

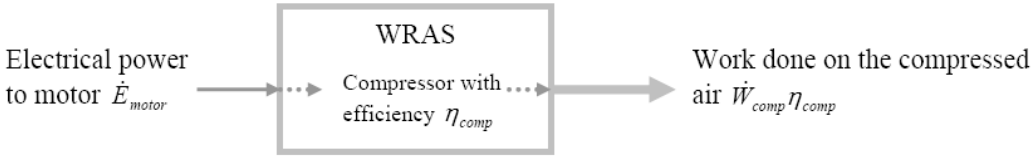

Figure 6.42 Schematically explanation of WRAS effectiveness definition.

$$\eta_{SS} = \frac{\dot{E}_{SS\_total} - \dot{E}_{SS\_cooling}}{\dot{m}_{H_2 cons} LHV_{H_2}} \tag{6.6}$$

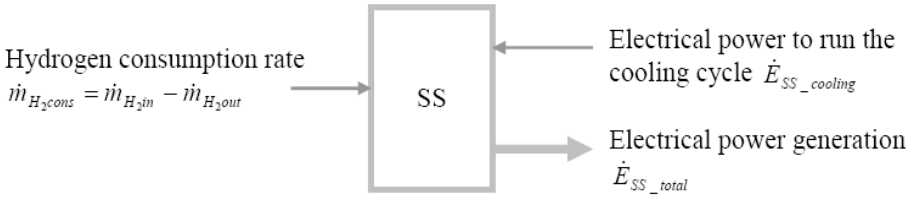

Figure 6.43 Schematically explanation of SS efficiency definition.

$$\eta_{PEMFC} = \frac{\dot{E}_{net}}{(\dot{m}_{CH_4} LHV_{CH_4})_{\text{to SMR}} + (\dot{m}_{CH_4} LHV_{CH_4})_{\text{to Comb}}} \tag{6.7}$$

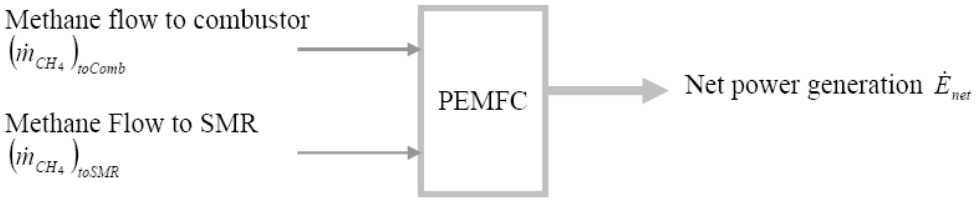

Figure 6.44 Schematically explanation of PEMFC efficiency definition.

where η_{FPS}, η_{WRAS}, η_{SS}, and η_{PEMFC} are the FPS, WRAS, SS, and the PEMFC system efficiencies/effectiveness, respectively. LHV_{H_2} and LHV_{CH_4} are the hydrogen and methane lower heating values, $\dot{m}_{H_2}$ and $\dot{m}_{CH_4}$ are the hydrogen and methane mass flow rates, $\dot{E}_{motor}$ is the parasitic power of the motor in the WRAS, $\dot{W}_{comp}$ and η_{comp} are the compressor power and isentropic efficiency in the WRAS, $\dot{E}_{SS\_total}$ is the total power generated from the stack, $\dot{E}_{SS\_cooling}$ is the power consumption for stack cooling, and $\dot{m}_{H_2cons}$ is the hydrogen consumption rate in the stack.

More explanations are necessary to better understand these definitions of the system/subsystem efficiencies/effectiveness. In the FPS, methane is utilized in both the SMR and the combustor to generate hydrogen and provide energy to the SMR respectively. In addition, exhausting hydrogen from the SS is another input to the combustor. These three inputs are all considered in calculating the FPS efficiency. In the WRAS, the two energy inputs are the electricity to the motor and the exhaust gases from the SS to the expander. However, only the electricity consumption is considered in the effectiveness calculation, which causes the WRAS effectiveness to be higher than 1 at some operational conditions. In the SS, some power generated from the stack is applied to the SS cooling subsystem so that the net power generation from the SS is the total power generation minus the cooling subsystem power. In the calculation of the system efficiency, the input is the consumed methane and the output is the net power output.

Figures 6.45a and 6.45b show the optimum SS, FPS, WRAS, and PEMFC system efficiencies/effectiveness over the entire load profile. The optimal average FPS efficiency is 80.2% over the 48 hours of operation, while the optimal instantaneous FPS efficiency

changes depending on the operating condition. The optimal average PEMFC system efficiency is about 39.5%, with an optimal average efficiency for the SS of 53%. The instantaneous WRAS effectiveness is higher than 1 at some operating points for the reason given in the previous paragraph.

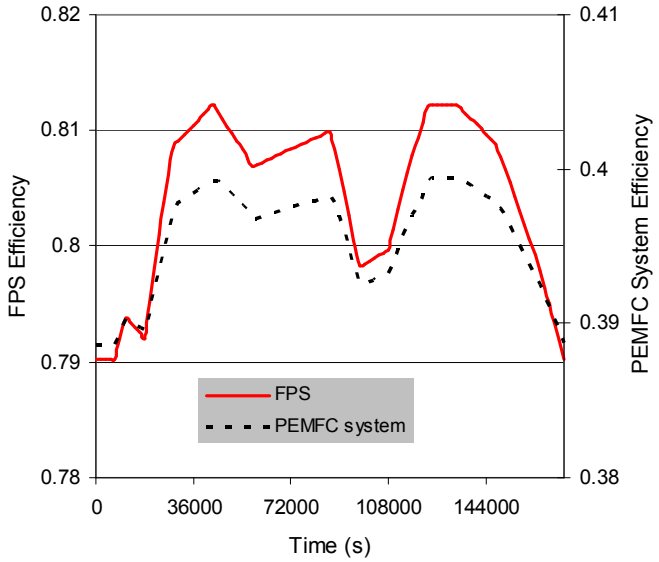

Figure 6.45a Efficiency of the optimum PEMFC system and FPS over the 48 hours of operation.

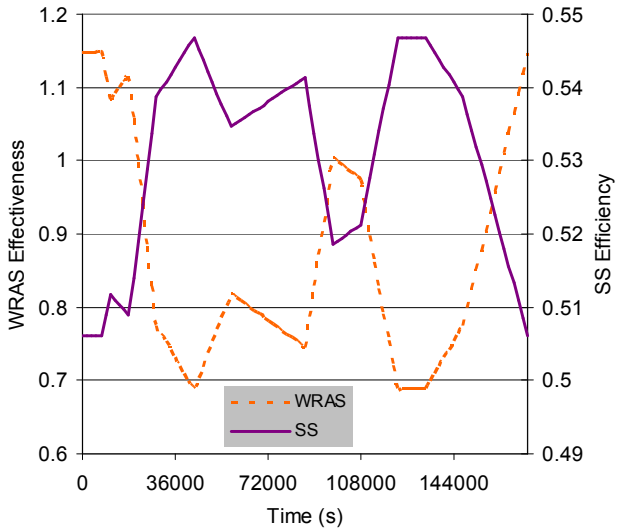

Figure 6.45b Effectiveness/efficiency of the optimum WRAS and SS over the 48 hours of operation.

Figure 6.46 presents the efficiencies of the compressor and expander in the WRAS over the 48 hour load profile. As can be seen by the figure, the optimal sizes of the compressor and the expander result in comparable efficiencies with the compressor is entropic efficiency slightly higher during certain periods of operation. With relatively low

air flow rates, which occur at lower loads, the compressor and the expander operate at efficiencies as much as 13% lower that at the full load operating which occur at the beginning and end of the load profile.

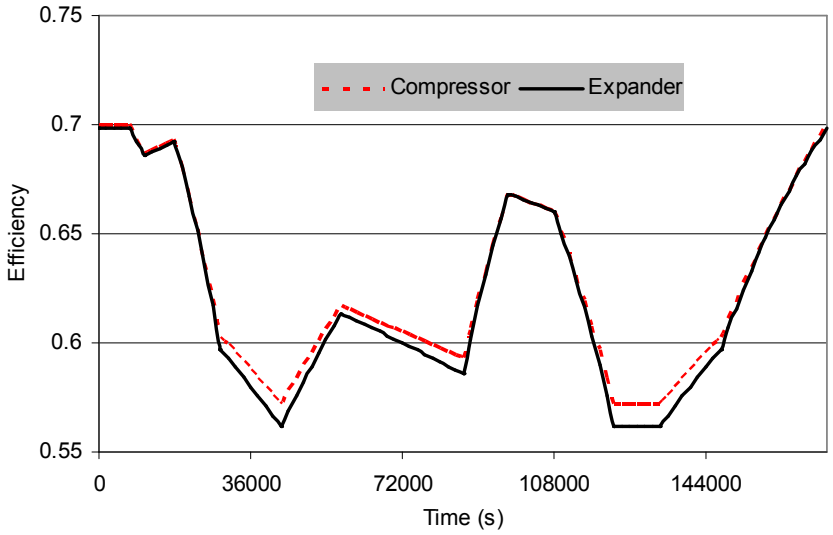

Figure 6.46 Optimal isentropic efficiencies of compressor and expander in the WRAS over the 48 hour load profile.

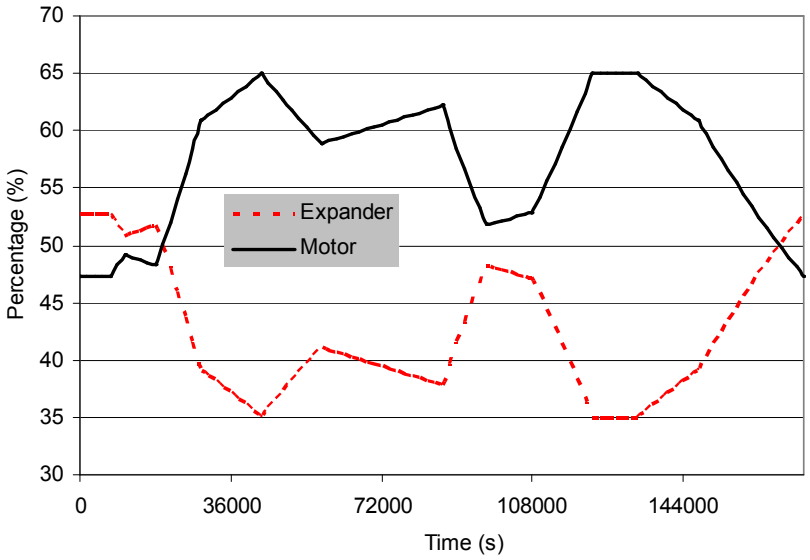

Figure 6.47 Optimal expander and motor output power percentages in the WRAS during the 48 hour load profile.

There are several thermal energy recovery and management cycles in the PEMFC system, which are able to enhance overall system efficiency. For example, the expander in the WRAS effectively recovers energy to significantly offset the parasitic load due to compressor operation. Power for the compressor is provide by the optimal motor and the

expander. The power percentages from these two components over the 48-hour load profile are shown in Figure 6.47. As can be seen, on average only around 55% of the optimal compressor power requirements need be obtained from the optimal motor while on average around 45% of the power requirements are supplied by the optimal expander using energy recovered from the exhausting stack gases on the cathode side. Another example is the fuel exhausting from the stack on the anode side which is recycled into the combustor that generates heat for the reforming process, which saves on methane consumption. The heat generation from the recycled hydrogen is on average around 18% to 19% of the total heat generation of the combustor for the optimum system configuration. A final example is the cooling air sent to the FPS for temperature control, which eventually ends up in the combustor with a temperature much higher than that of the environment, enhancing the efficiency of the combustor.

6.8 Comparison with Hybrid Heuristic/Gradient Based Optimization Results of Kim (2008)

One objective of this research is to compare the results of the gradient-based optimization results obtained here on energy system development with those obtained by Kim (2008) using the same models but based on a and hybrid heuristic/gradient based optimization. The latter is a surrogate algorithm using surrogate models obtained from some samples over design space of the actual model. With the surrogate models, optimizations using SQP (Sequential Quadratic Programming) are carried out (not the actual models) to reduce lots of computational time. Once the optimization processes find a set of possible solutions, these optimum points are evaluated using the actual model. After these, the surrogate models are modified again using these updated information. This procedure is kept until the optimization is converged. Due to the fact of screening all design spaces, this surrogate algorithm has high possibility to find global optimum point.

Figure 6.48 shows the comparison of the DILGO based optimization results for the PEMFC system with different optimization algorithms: the gradient-based optimization used here and the hybrid heuristic/gradient based optimization used in Kim (2008). With the hybrid heuristic/gradient based optimization strategy (i.e. the so-called surrogate method), the optimization gives better results than that of the gradient-based

optimization, and also solves the system-level, unit-based optimizations in fewer iterations (i.e. DILGO converges more quickly than with the gradient-based method). The reason is that for highly non-linear problems, a well designed and conditioned hybrid heuristic/gradient based optimization strategy such as surrogate method or a genetic algorithm does a better job of searching the solution space of optimal solutions for the global optimum avoiding the tendency some what better than of a gradient-based approach of falling into a local optimum. Detailed information about hybrid heuristic/gradient based optimization can be found in Kim (2008).

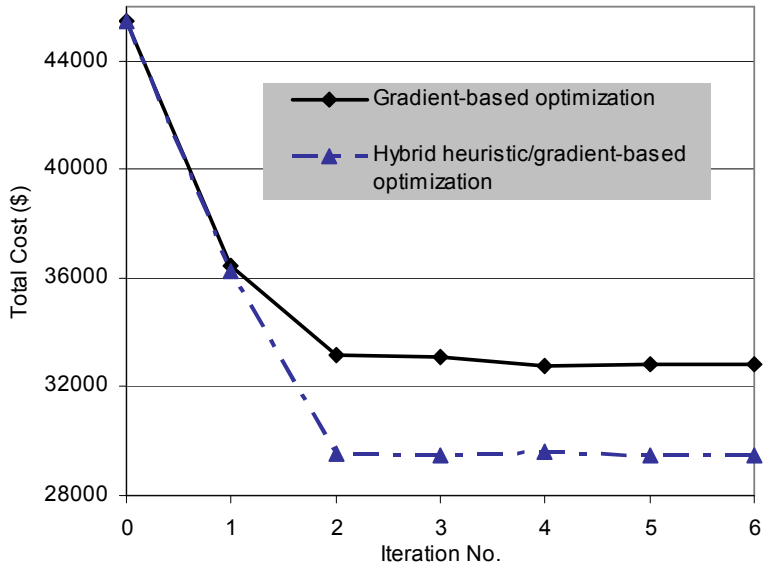

Figure 6.48 Comparison of DILGO results with gradient and hybrid heuristic/gradient based optimizations.

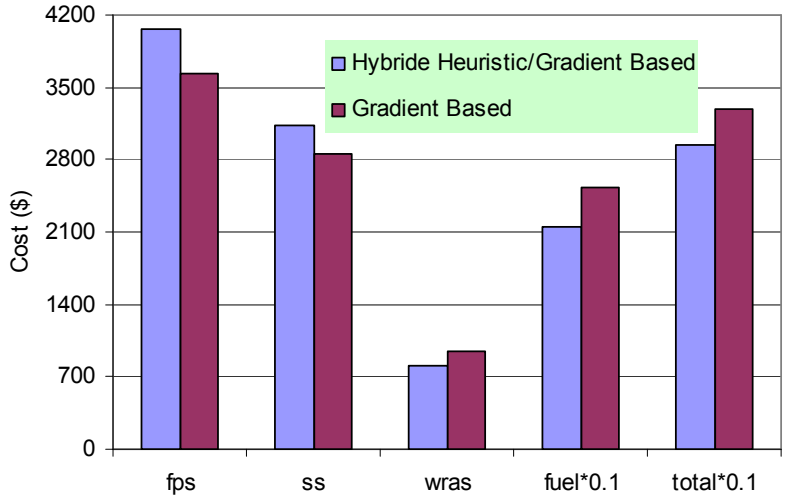

Figure 6.49 Optimum PEMFC system costs comparison with gradient and hybrid heuristic/gradient based optimizations.

Figure 6.49 presents the difference between the two optimum PEMFC system obtained by the different optimization schemes. In the figure, the optimum PEMFC system costs (capital costs of each subsystem, system operating costs and system life cycle costs) obtained by using the hybrid heuristic/gradient and gradient optimization strategies are presented. As shown in this figure, the optimum system from the surrogate method suggests a bigger system, which increases the capital cost but saves on the cost of fuel. Therefore, the hybrid heuristic/gradient method results in a better trade off between capital and the operating costs. As shown in Figure 6.50, the optimum system obtained from the hybrid heuristic/gradient based optimization consumes less fuel (methane) to support the fuel reforming and combustion processes.

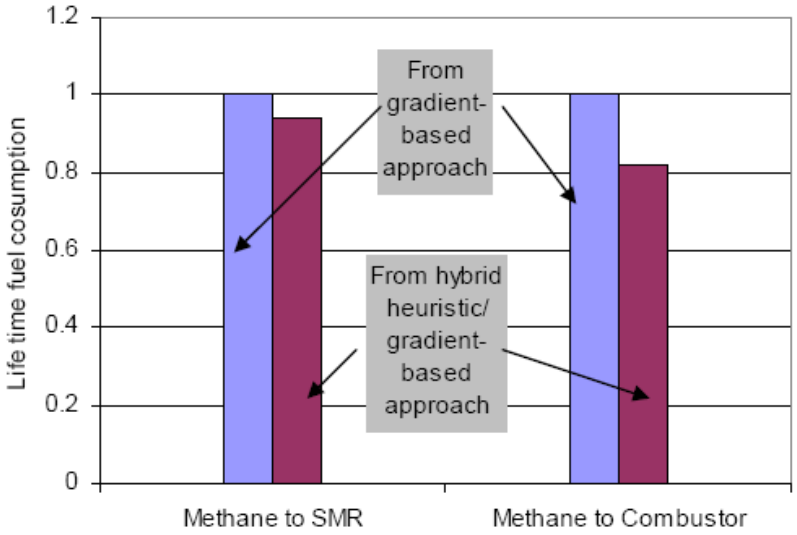

Figure 6.50 Comparison of the optimum system fuel consumption rate resulting from the gradient-based and hybrid heuristic/gradient based optimization strategies.

6.9 Run Times and Computer resources

Table 6.3 Computational time consumption at different cases.

	48 hour dynamic simulation(Min)	Steady state optimization (hour)	Dynamic optimization (hour)
FPS	5	20	40
SS	<1	<0.1	0.2
WRAS	<1	<0.1	0.2
PEMFC system	6	25	48

In this research, the PEMFC system dynamic simulations and optimizations (steady state and dynamic) are performed with an Intel Pentium dual-core processor computer

with 1GB of memory. The runtimes of the simulations and optimizations are shown in Table 6.3.

Chapter 7

Conclusions and Future Work

7.1 Conclusions

Conclusions of this doctoral work for solving the synthesis/design and operation/control optimization problem of a PEMFC system for residential applications are summarized as follow:

1. State space control design has shown the capabilities in complex energy system dynamic operation control as well as integrating with the decomposition strategy, DILGO, in solving the multi-level synthesis/design and operation/control optimization problems.
2. Due to the advantages of state space method in multi variables control design over the classical method, and the strong capability of the DILGO in solving complex optimization problem, the integration of the state space control design and the DILGO has the ability in solving highly nonlinear, complex energy system synthesis/design, operation/control optimization problems.
3. The results of the looped optimization prove that, in a dynamic synthesis/design and operation optimization based on the system total cost, the controllers in the system will be a limitation to the optimization even they have only minor affect to the total cost. Because the optimization can only find out the optimum system which can still be controlled by the controllers. Thus, the gains of controllers should be considered as part of decision variables in the dynamic optimization, which becomes a dynamic synthesis/design and operation/control optimization.
4. In the energy system synthesis/design, the name ‘synthesis’ refers to changes in system or component configuration, which can also be treated in the dynamic synthesis/design and operation/control optimization. Therefore, when considering the configuration of the originally proposed system, more components may be able

to put into the whole system model, if it is not very clear that whether they are necessary of not. Later, the existence of these components can be decided by the synthesis/design and operation/control optimization. As shown in this research, for the FPS optimization results, the optimum lengths of two heat exchangers are zero, which eliminates these two components from the FPS.

5. For an energy system synthesis/design and operation optimization, the typical way is to optimize the system at steady state, full load condition. But this may give overestimated solutions, i.e. bigger sizes of the system, which will increase the total system cost. On the other hand, dynamic synthesis/design and operation/control optimization can give better results over the steady state optimization by choosing more reasonable size of the energy system, based on representative load profiles.
6. By comparing with single level optimization results, the decomposition optimization strategy, DILGO, has shown its capability and accuracy to handle the large-scale DMINLP problems for energy system. DILGO effectively handles the information transfer problems between subsystems when subject to external forces (e.g., change in load) and internal regulation (e.g. system control system), in the way to ensure that the decomposed unit-based optimizations are able to result in an overall system-level optimum.
7. The integration of state space control design and the DILGO constitutes a powerful way of not only obtaining a global optimum solution for the complex dynamic synthesis/design and operation/control optimization problems, but also gaining a big amount of insight into the system dynamics and the relations among each unit/subsystem and its respective decision variables.
8. The integration of state space control design and the DILGO decomposition strategy successfully applied to the transients and control of highly complex, highly dynamic, non-linear systems. It considers dynamic, control, and operation requirements all together at the early stages of the conceptual and preliminary synthesis/design stage. This is achieved by the integration of state space control design and the DILGO in such a way that it is possible to pose a synthesis/design and operation/control system optimization problem.

9. By dividing the total energy system into subsystems, the technique of physical decomposition (DILGO in particular) has the advantage of breaking the overall optimization problem into a set of much smaller, unit-level problems, which simplifies a highly complex, highly dynamic, non-linear synthesis/design and operation/control optimization problem and allows one to take into account a larger number of decision variables (degrees of freedom) than would otherwise be impossible or with a lot of difficulties. Therefore, this physical decomposition strategy makes it possible to simultaneously optimize not only at a system level, i.e. with respect to the system's performance and configuration synthesis, but also at a detailed component/subsystem level, i.e. with respect to the detailed geometry, capacities, and performance of the components themselves.
10. As a decomposition strategy which takes iterative optimization procedure to find the solution, DILGO uses dynamic shadow price rates and coupling function changes to reduce the number of unit optimizations. The effect of the different units' decision variables and dynamics are assessed in terms of the unit's (local) cost and their effect on the rest of the system. Each of these sub-problems, using strictly unit (local) decision variables, apPrOximates the system-level optimum cost. The dynamic shadow price rates are in fact the dynamic marginal cost rates based on the optimum cost rates of the units. The dynamic shadow price rates are an approximation of the dynamic optimum response surface (ORS).
11. Physical decomposition (in particular DILGO) allows different subsystems to be modeled using the most appropriated software. As a matter of fact, different subsystems are often synthesized/designed by different groups and even different companies, which in turn are most probably in different geographical locations. Therefore, diverse modeling platforms are almost assuredly unavoidable.
12. The DMINLP problem for the PEMFC was solved and the global convergence of the DILGO method was verified. In the DILGO iteration, the calculation of the dynamic shadow price rates is crucial. A relatively constant behavior of the dynamic shadow price rates is a significant contributing factor to the rather fast convergence of the DILGO approach. This constant behavior of the dynamic shadow price rates allows one to infer that they are linear or at least monotonic

(e.g., convex) with respect to the coupling functions but not necessarily with respect to time. In case of un-constant dynamic shadow price, appropriate selection of the step length to calculate the dynamic shadow price is important and will affect the rate of convergence.

13. The thermal energy recovery and management cycles considering heat exchangers and the expander show the capability to enhance the total system efficiency. The thermal energy from chemical reactions is recovered by air to increase the inlet flow temperature of the combustor. The expander in the WRAS effectively recovers energy to significantly offset the parasitic load due to compressor operation. The exhausting fuel from stack anode is also being recycled into the combustor to generate heat. The end result of all of this is that, taking capital cost into account, an incredibly efficient and cost effective system can be developed with internal energy recovery and management.
14. The optimum configuration of the PEMFC system, which is one product of this research, is shown to enhance the total system efficiency significantly in such way that the average system efficiency through the entire load profile is 39~40%. The system is able to operate at full and low loads (the low loads are approximately 40 % of the system full power) without sacrificing system performance. In fact, at low load system performance increases because the increase in the SS and FPS efficiencies surpass of the reduction in efficiency due to the parasitic load for air compression.
15. The fact that the consumption of natural gas throughout the system's lifetime represents almost 80% of the total cost indicates that the proposed system is theoretically more attractive at locations where natural gas is cheaper. Additionally, the life cycle capital cost breakdown shows that the fuel cell stack and the chemical reactors in the FPS are the major capital costs of the PEMFC system.

7.2 Recommendations for Future Work

With the all the results and conclusions presented already, there are still some additional issues that may be considered as future steps of this doctoral work. They are listed below.

1. The increasing complexity of energy systems and the need to account for transient behavior create a severe computational burden for simulation, control, and optimization. Some recommendations can be made to simplify this type of problem based on the experiences of this doctoral work.
    1.1. Before modeling a system, some sensitivity analysis of the system can be done utilizing models/results from others. Then, in the model, different complexities can be applied to different units. Variables/components with high effect to the system need to be considered in detail, while others with low effect can be treated briefly. In case of components on which the system has low sensitivity, their models in the whole system may even be substituted by the linearized models to reduce the complexity of the system simulation.
    1.2. It is difficult to get the linearized model of the whole system. Therefore, it is better to have separated linearized model of each component/unit of the system, before the component/unit model being put into the system. Thus, the whole system linearized model can be the combination of the linearized models of all the components, which can be utilized for the purpose of control design.
    1.3. In the optimization, one difficulty is to find the reasonable boundaries for each decision variables. A simple model that contains more linearized models could potentially aid in the search of the optimum synthesis/design space. Once a few "promising areas" are found one could switch to a more complex model.
2. The PEMFC stack applied in this research is a 1-D model, which only considers the direction orthogonal to the stack anode/cathode. Thus, the phenomenon along the flow channels of bipolar plates is not being studied, such as concentration changing of hydrogen and oxygen. And this will affect the optimization results as well. Therefore, a more detailed fuel cell stack model will give better understanding of the whole system simulation and optimization.
3. For the whole PEMFC system control design, or any other complex energy system, state space method has very strong capability, but requires much more equations in modeling and consumes much longer time in calculation. One way to reduce the complexity is to have the sensitivity analysis between the inputs and the outputs of the system. If there is one/several output which is mainly determined by one/several

input, this input-output relation can be separated from the whole system multi-input, multi-output control design problem.

4. In the energy system optimization, one of the reasons that the dynamic optimization gives better results over steady state optimization is that the dynamic optimization considers the whole operation procedures instead of only full load. Thus, the selected load profile characteristic will affect the optimization results, such as a load profile with long part load schedule will favorite small size of system. Therefore, it is very important to choose the representative load profile intelligently to be as close as possible to the real operation conditions.

REFERENCES

Arthur D. Little, Inc., 2001, Conceptual Design of POX/SOFC 5kW Net System, The Final Report for the Department of Energy Technology Laboratory.

Baratto, F., Diwekar, U., and Manca, D., 2005a, Impacts Assessment and Trade-offs of Fuel Cell-Based Auxiliary Power Units Part I: System Performance and Cos modeling, Journal of Power Sources, Vol. 139, pp 205-213.

Baratto, F., Diwekar, U., and Manca, D., 2005b, Impacts Assessment and Trade-offs of Fuel Cell-Based Auxiliary Power Units Part II: Environments and Health Impacts, LCA, and Multi-objective Optimization, Journal of Power Sources, Vol. 139, pp 214-222.

Bejan, A., 1995, Entropy Generation Minimization, CRC Press, Boca Raton, Florida.

Bejan, A., Tsatsaronis, G., et al., 1996, Thermal Design and Optimization, John Wiley and Sons, New York.

Bird, J. P., Model of the Air System Transients in a Fuel Cell Vehicle, 2002, Master Thesis, Department of Mechanical Engineering, Virginia Polytechnic Institute and State University.

Boettner, Daisie D., and Moran, Michael J, Proton Exchange Membrane (PEM) Fuel Cell Powered Vehicle Performance Using Direct Hydrogen Fueling and on-board Methanol Reforming, Vol. 29, Issues 12-15, Oct.-Dec., 2004, Pages 2317-2330.

Braun, Robert J., 2002, Optimal Design and Operation of Solid Oxide Fuel Cell Systems for Small-scale Stationary Applications, PhD. Thesis, Mechanical Engineering Department, University of Wisconsin – Madison.

Carlos A. Coello Coello, Gary B, Lamont, Applications of Multi-Objective Evolutionary Algorithms, 2004.

Carlson, E. J., Kopf, P., Sinha, J., Sriramulu, S., and Yang, Y., 2005, Cost Analysis of PEM Fuel Cell Systems for Transportation, TIAX LLC, Cambridge, Massachusetts.

Ceraolo, M., Miulli, C., and Pozio, A., 2003, Modeling Static and Dynamic Behaviour of Proton Exchange Membrane Fuel Cells on the Basis of Electro-Chemical Description, Journal of Power Sources, 113, pp. 131-144.

Choi, Y., and Stenger, H. G., 2004, Kinetics, Simulation and Insights for CO Selective Oxidation in Fuel Cell Applications, Journal of Power Sources, 129, pp.246-254.

El-Sayed Y.M., 1996, A Second-Law-Based Optimization: Part I Methodology & Part 2, ASME Application, Journal of Energy Resources Technology, vol. 118, pp. 693-703.

El-Sayed, Y. M., and Evans, R. B., 1970, Thermoeconomics and the Design of Heat Systems, Journal of Engineering for Power, ASME Transactions, Vol. 92, 27, Jan.

Energy Information Administration, 2006, U.S. Natural Gas Prices, http://www.eia.doe.gov.

Ettouney, H. M., Shaban, H. I., and Nayfeh, L. J., 1995, Theoretical Analysis of High and Low Temperature Shift Concerters, Chem. Eng. Comm., 1995, Vol. 134, pp.1-16.

Evans, R. B., 1980, Thermoeconomic Isolation and Exergy Analysis, Energy: The Internal Journal, Vol. 5, No. 8-9, 805-821.

Evans, R. B., and von Spakovsky, M. R., 1993, Engineering Functional Analysis (Part II), Journal of Energy Resources Technology, ASME Transactions, vol. 115, No. 2, N.Y., June.

Frangopoulos, C. A., 1983, Thermoeconomic Functional Analysis: A Method for Optimal Design or Improvement of Complex Thermal Systems, School of Mechanical Engineering, Georgia Institute of Technology, PhD dissertation.

Frangopoulos, C. A., 1994, Application of Thermoeconomic Optimization Methods to the CGAM Problem, Energy: The International Journal, special edition, Vol. 19, No. 3, pp. 323-342, Pergamon Press, Great Britain.

Frangopoulos, C. A., and Evans, R. B., 1984, Thermoeconomic Isolation and Optimization of Thermal System Components", Second Law Aspects of Thermal Design, HTD Vol. 33, ASME, New York, August.

Frangopoulos, C., von Spakovsky M. R., and Sciubba E., 2002, A Brief Review of Methods for the Design and Synthesis Optimization of Energy Systems, International Centre for Applied Thermodynamics Journal. Vol. 5 No. 4, pp 151-160.

Franklin, G. F., J. David Powell, and Abbas Emami-Naeini, Feedback Control of Dynamic Systems, 2nd ed. Reading, MA: Addison-Wesley, 1991.

Fuel Cell Handbook, 2004, 7th edition, U.S. Department of Energy, Office of Fossil Energy, National Energy Technology Laboratory, Morgantown, West Virginia.

Fuel Cell Turbocompressor, Hydrogen and Fuel Cells Merit Review, May 22, 2003, Claremont Resort & SPA, Berkeley, CA, Honeywell.

Gee, M. K., Fuel Cell Turbocompressor, Hydrogen and Fuel Cells Merit Review, Berkeley, CA, May, 2003.

Georgopoulos, N. G., 2002, Application of a Decomposition Strategy to the Optimal Synthesis/Design and Operation of a Fuel Cell Based Total Energy System, M.S. Thesis, Department of Mechanical Engineering, Virginia Polytechnic Institute and State University, Blacksburg, Virginia.

Georgopoulos, N. G., von Spakovsky, M. R., and Muñoz, J. R., 2002, A Decomposition Strategy Based on Thermoeconomic Isolation Applied to the Optimal Syntheses/Design and Operation of a Fuel Cell Based Total Energy System, International Mechanical Engineering Congress and Exposition – IMECE 2002, ASME, No. 33320, N.Y., N.Y., November.

Hajela, P., Lee, E., Constrained Genetic Search Via Schema Adaptation: An Immune Network Solution, Journal of Structural Optimization, Vol. 12, No. 1, 11-15, 1996.

Handbook of Electric Motors, Second Edition, Toliyat, H. A., and Kliman, G. B, 2004.

Haslego, C., and Polley, G., September, 2002, Compact Heat Exchanger – Part I: Designing Plate- and Frame-Heat Exchangers, Chemical Engineering Progress.

Hjorteland, T., The Action Variational Principle in Cosmology, June 1999.

Hydrogen, Fuel Cells and Infrastructure Technologies Program, 2003 annual progress report, U.S. Department of Energy.

Ishida, M., Shiga, N., and Sadahiro, K., Improvement of Motor Performance by Use of High-Efficiency Electrical Steels, Kawasaki Steel Technical Report, No. 48, March, 2003.

James, B. D., Lomax, F. D., Thomas C. E., and Colella, W. G., 1997, "PEM Fuel Cell Power System Cost Estimates: Sulfur-Free Gasoline Partial Oxidation and

Compressed Direct Hydrogen", Final Report for the Ford Motor Company, Arlington, Virginia, October.

Kakac, S., and Liu, H., 2002, Heat Exchangers Selection, Rating, and Thermal Design, CRS press.

Kamarudin, S. K., Daud, W.R.W., Som, A. Md., Takriff, M. S., and Mohammard, A. W., 2006b, Synthesis and Optimization of a PEMFC System via Reactor-Separation Network (RSN), Journal of Power Sources, Vol. 159, pp 1194-1204.

Kern, D. Q., 1950, Process Heat Transfer, McGraw-Hill, New York.

Khandkar, A., Hartvigsen, J., and Elangovan, S., 1998, Selection of SOFC Stack Operating Point for Optimal Balance of Efficiency and Power, Proceedings of the Third European Solid-oxide Fuel Cell Forum.

Kim, K., 2005, An Experimental Study on the Performance of Plate Heat Exchanger, Society of Air-Conditioning Refrigerating Engineers, Vol. 17, No. 2, pp 117-124.

Kim, K., 2008, Dynamic Proton Exchange Membrane Fuel Cell System Synthesis/Design and Operation/Control Optimization under Uncertainty, PhD dissertation, Department of Mechanical Engineering, Virginia Polytechnic Institute and State University, Blacksburg, Virginia.

Larminie, J., and Dicks, A., 2003, Fuel Cell System Explains.

Linnhoff, B., Pinch Technology for the Synthesis of Optimal Heat and Power Systems, Journal of Energy Resources Technology, September 1989, Vol. 111, pp. 137-147.

Melli, R., and Sciubba, E., 1997, A Prototype Expert System for the Conceptual Synthesis of Thermal Processes, Energy convers. Mgmt Vol. 38, No. 15-17, pp. 1737-1749.

Metropolis, N., A. Rosenbluth, M. Rosenbluth, A. Teller, E. Teller, Equation of State Calculations by Fast Computing Machines, J. Chem. Phys., 21, 6, 1087-1092, 1953.

Moran, M. J., Availability Analysis: A Guide to Efficient Energy Use (New Jersey: Prentice-Hall Inc., 1982)

Muñoz, J. R., 2000, Optimization Strategies for the Synthesis/Design of Highly Coupled, Highly Dynamic Energy Systems, PhD. Thesis, Department of Mechanical Engineering, Virginia Polytechnic Institute and State University, Blacksburg, Virginia.

Muñoz, J. R., and von Spakovsky, M. R., 2000, The Use of Decomposition for the Large Scale Synthesis/Design Optimization of Highly Coupled, Highly Dynamic Energy Systems: Part I – Theory, 2000 ASME International Mechanical Engineering Congress and Exposition, Orlando, Florida, November 5-10.

Muñoz, J. R., and von Spakovsky, M. R., 2001a, A Decomposition Approach for the Large Scale Synthesis/Design Optimization of Highly Coupled, Highly Dynamic Energy Systems, International Journal of Applied thermodynamics, March, Vol. 4, no. 1.

Muñoz, J. R., and von Spakovsky, M. R., 2001b, The Application of Decomposition to the Large Scale Synthesis/Design Optimization of Aircraft Energy Systems, International Journal of Applied thermodynamics, June, Vol. 4, no. 2.

Oei, D., Adams, J. A., Kinnelly, A. A., Purnell, G. H., Sims, R. I., Sulek, M. S., and Wemette, D. A., 1997, Direct-Hydrogen-Fueled Proton-Exchange-Membrane Fuel Cell System for Transportation Applications, Final Report for the U.S. Department of Energy, Report No. DOE/CE/50389-503, Dearborn, Michigan, July.

Olsommer, B., von Spakovsky, M. R., Favrat, D., 1999a, An Approach for the Time-dependent Thermoeconomic Modeling and Optimization of Energy System Synthesis, Design and Operation (Part I : Methodology and Results), International Journal of Applied Thermodynamics, vol. 2, No. 3.

Olsommer, B., von Spakovsky, M. R., Favrat, D., 1999b, An Approach for the Time-dependent Thermoeconomic Modeling and Optimization of Energy System Synthesis, Design and Operation (Part II : Reliability and Availability), International Journal of Applied Thermodynamics, vol. 2, No. 4.

Peter, M., Timmerhaus, K., and West, R., 2003, Plant Design and Economics for Chemical Engineers, 5th Edition, McGraw-Hill, New York.

Pukrushpan, J. T., Stefanopoulou, A. G., Peng, H., Modeling and Control for PEM Fuel Cell Stack System, American Control Conference, Anchorage, AK, 2003.

Rancruel, D. F., 2005, Dynamic Synthesis/Design and Operation/Control Optimization Approach Applied to a Solid Oxide Fuel Cell Based Auxiliary Power Unit under Transident Conditions, PhD. Dissertation, Department of Mechanical Engineering, Virginia Polytechnic Institute and State University, Blacksburg, Virginia.

Rancruel D. F., and von Spakovsky, M. R., 2003, Decomposition with Thermoeconomic Isolation Applied to the Optimal Synthesis/Design of an Advanced Fighter Aircraft System, International Journal of Thermodynamics, Vol. 6, No. 3, pp. 93-105, September.

Rao, S. S., 1996, Engineering Optimization – Theory and Practice, John Wiley and Sons, N.Y.

Suh, K., Stefanopoulou, A., 2005, Coordination of Converter and Fuel Cell Controllers, International Journal of Energy Research 29(12): 1167-1189.

Technical Bulletin 103, MOOG INC., Controls Division, Thayer, W. J., 1965, Transfer Functions for MOOG Servovalves, East Aurora, NY.

Toliyat, H. A., and Kliman, G. B., 2004, Handbook of Electric Motors, Second Edition, Revised and Expanded.

Tsatsaronis, G., Pisa, J., et al., 1989, Thermodynamic Analysis and Improvement of Energy Systems, Proceedings of the International Symposium, Beijing, China, Pergamon Press, pp. 195-200.

Tsatsaronis, G., and Pisa, J., 1994, Exergoeconomic Evaluation and Optimization of Energy Systems – Application to the CGAM Problem, Energy – The International Journal, Vol. 19, No. 3, pp. 287-321.

Valero, A., Lozano, M., et al., 1994, Application of the Exergetic Cost Theory to the CGAM Problem, Energy – The International Journal, vol. 19, No. 3, pp. 365-381.

Varigonda, S., Pukrushpan, J., Stefanopoulou, A., 2003, Challenges in Fuel Cell Power Plant Control: The Role of System Level Models, AIChE Spring Meeting.

von Spakovsky, M. R., 1994, Application of the Functional Analysis to the Analysis and Optimization of the CGAM Problem, Energy – The International Journal, Vol. 19, No. 3, pp. 343-364.

von Spalovsky, M. R., and Evans, R. B., 1984, Detailed Second Law Design of Components in Complex Thermal Systems, Second Law Aspects of Thermal Design, HTD vol. 33, ASME, N.Y., N.Y., August.

von Spalovsky, M. R., and Evans, R. B., 1993, Engineering Functional Analysis (Part I), Journal of Energy Resources Technology, ASME Transactions, Vol. 115, No. 2, June.

Xiang-Sun Zhang, Neural Networks in Optimization, Kluwer Academic Publishers, Dordrecht, Boston, London, 2000.

Xu, J., and Froment, G. F., 1989, Methane Steam Reforming, Methanation and Water-Gas Shift: I. Intrinsic Kinetics, AIChE Journal, Vol. 35, No. 1, pp. 88-96, January.

Xu, J., and Froment, G. F., 1989, Methane Steam Reforming: II. Diffusional Limitations and Reactor Simulation, AIChE Journal, Vol. 35, No. 1, pp. 97-103, January.

Zhang Xiang-Sun, Neural Networks in Optimization, 2000.